UC Berkeley
UC Berkeley Electronic Theses and Dissertations

Title
Optical Magnetometry with Nitrogen-Vacancy Centers in Diamond

Permalink
https://escholarship.org/uc/item/1rj4p2ch

Author
Acosta, Victor Marcel

Publication Date
2011

Peer reviewed|Thesis/dissertation

eScholarship.org Powered by the California Digital Library
University of California

Optical Magnetometry with Nitrogen-Vacancy Centers in Diamond

by

Victor Marcel Acosta

A dissertation submitted in partial satisfaction of the
requirements for the degree of
Doctor of Philosophy
in
Physics
in the
Graduate Division
of the
University of California, Berkeley

Committee in charge:

Professor Dmitry Budker, Chair
Professor Irfan Siddiqi
Professor Robert Littlejohn
Professor David Attwood

Spring 2011

Optical Magnetometry with Nitrogen-Vacancy Centers in Diamond

Copyright 2011
by
Victor Marcel Acosta

Abstract

Optical Magnetometry with Nitrogen-Vacancy Centers in Diamond

by

Victor Marcel Acosta

Doctor of Philosophy in Physics

University of California, Berkeley

Professor Dmitry Budker, Chair

Precision measurement of magnetic fields is at the heart of many important analytic techniques in materials, geology, biology, medicine, security, space, and the physical sciences. These applications require operation under a wide range of specifications regarding sensitivity, spatial resolution, bandwidth, scalability, and temperature. In this work we have developed the enabling technology for magnetometers based on nitrogen-vacancy (NV) defects in diamond which promise to cover a wider portion of this parameter space than existing sensors. We have studied how to prepare diamond material optimized for magnetometry, and we observed the basic optical and spin properties of the NV centers. Using a novel scheme inspired by new information about NV centers gathered from these studies, we constructed a sensor which improved on the state-of-the-art in a number of areas. Finally, we outline a plan for improving these sensors to study micro- and nano-scale magnetic phenomena currently inaccessible using existing technology.

To my parents, Marjorie Churgin and Thomas Acosta,
and my partner Andrea Lee,
for their generous love and support.

Contents

List of Figures **iv**

List of Tables **xiii**

1 Physics of nitrogen-vacancy centers in diamond and overview of the field **1**

1.1 Introduction 1

1.1.1 Comparison with existing technologies 2

1.2 Historical background 3

1.2.1 ODMR in diamond 5

1.2.2 Single-spin ODMR 6

1.3 NV center physics 7

1.3.1 Group theory and electron orbitals 7

1.3.2 Optical selection rules 9

1.3.3 Absorption and fluorescence spectra 11

1.3.4 Intersystem crossing and optical pumping 13

1.3.5 Ground-state level structure and ODMR based magnetometry 14

1.3.6 Effect of zero-field splitting on sensitive magnetometry 17

1.3.7 Interaction with environment 18

1.4 Experimental realizations 21

1.4.1 Near-field scanning probes and single-NV magnetometry 22

1.4.2 Far-field sub-wavelength probes 27

1.4.3 Wide-field array magnetometers 29

1.4.4 Bulk micro-magnetometers 30

1.5 Outline of remaining chapters 30

2 Diamonds with a high density of nitrogen-vacancy centers for magnetometry applications **31**

2.1 Abstract 31

2.2 Introduction 31

2.3 Experimental Procedure 32

2.3.1 Sample parameters and irradiation 32

    2.3.2 Optical characterization and annealing 33
  2.4 Results 34
    2.4.1 Proton-irradiated samples 34
    2.4.2 Electron-irradiated samples 40
    2.4.3 Light-power dependence of NV^0 and NV^- concentrations . . . 50
    2.4.4 Optically detected magnetic resonance (ODMR) 52
    2.4.5 Prospects for ultra-sensitive magnetometry 57
  2.5 Conclusion 58
  2.6 Acknowledgements 58

3 Temperature dependence of the nitrogen-vacancy magnetic resonance 60
  3.1 Abstract 60
  3.2 Introduction 60
  3.3 Experiment procedure 61
  3.4 Zero-field Hamiltonian and fitting procedure 61
  3.5 Results 62
  3.6 Calculation of D and its relative temperature dependence 66
  3.7 Significance for magnetometry applications 66
  3.8 Conclusion 67
  3.9 Addendum 67

4 Optical properties of the nitrogen-vacancy singlet levels in diamond 70
  4.1 Abstract 70
  4.2 Introduction 70
  4.3 Experimental apparatus 73
  4.4 Optical properties, spin-dynamics and temperature-dependent lifetimes 73
  4.5 Conclusion 76

5 Broadband magnetometry by infrared-absorption detection of diamond NV centers 79
  5.1 Abstract 79
  5.2 Introduction 79
  5.3 Fundamental limits on sensitivity 80
  5.4 Infrared absorption technique 81
  5.5 Operation as a magnetic gradiometer 83
  5.6 Eliminating photon shot-noise 85
  5.7 Conclusion 85

6 Conclusion 86

Bibliography 87

List of Figures

1.1 Comparison of some of the most sensitive magnetometry technologies. The points for diamond are the projected sensitivities based on Eq. (1.1), and the other points are experimental results for magnetometers based on vapor-cells [1, 2], Bose-Einstein Condensates (BEC) [3], low-frequency micro-SQUIDs [4], nano-SQUIDs [5], and narrowband MRFM [6]. The lines represent the theoretical range and scaling of the spatial resolution for potential sensors based on these technologies (MRFM and BECs have limited range and complicated scaling and are not shown here). Note that the sensitivity scaling with size for all sensors is $\delta B \propto r_{min}^{-3/2}$ (see, for example, [7]) except in the case of nano-SQUIDs (without a pickup coil) where the scaling is $\delta B \propto r_{min}^{-5/4}$ [8]. The numbers are the temperature ranges (in Kelvin) for each sensor as reported in the references. 4
1.2 Optical microscope image of a $\sim$ 100 μm sized single-crystal HPHT microdiamond (a) after initial growth, (b) after irradiation with 8-MeV electrons at a dose of $\sim 10^{19}$ cm^{-2}, and (c) after annealing at 800° C for 2 hours. Figure courtesy of G. Balasubramanian. 5
1.3 (a) Schematic of the NV center with nitrogen, vacancy, and three nearest-neighbor carbon atoms. The geometry and atomic labels are those used to derive the molecular orbitals (MOs). (b) MOs of the three highest-energy single-electron orbitals, a_1, e_x, and e_y. The red (blue) colors denote positive (negative) contributions to the MO. Adapted from [9] with author permission. (c) Schematic of the six-electron configuration for (left) the ground, e^2, and (right) first-excited, a_1e, configurations. The specific wavefunctions depicted here correspond to (left) $\mid e_xe_y\rangle = \mid {}^3A_2, m_s = +1\rangle$ and (right) $\mid a_1e_x\rangle = \mid {}^3E_x, m_s = +1\rangle$. Note that the lowest-energy level, a_1', is predicted to lie below the valence band [10] and experiments have established that the conduction band is well above the e_x, y levels. 8

1.4 (a) Schematic illustrating the Franck-Condon principle for excitation and fluorescence of the main optical transition, $^3A_2 \leftrightarrow {}^3E$. Nonradiative decay is shown with dashed lines. (b) Room-temperature optical absorption and fluorescence (excited at 532 nm) spectra for an HPHT diamond with [NV$^-$] $\approx$ 15 ppm. Besides the spectral features attributed to the NV$^-$ center discussed in the text, the weak line at 575 nm is present from the NV^0 ZPL. PSB–Phonon sideband, ZPL–zero-phonon line. 12

1.5 Level diagram for the NV center showing spin-triplet ground and excited states, as well as the singlet system involved in intersystem crossing. Radiative transitions are indicated by solid arrows and non-radiative transitions by dashed arrows. Only those transitions confirmed by experiments are shown. The tentative label of the upper (lower) singlet as ^1E ($^1A_1$) is based on the observed spin-selective decay paths (see text). Lifetimes of the excited levels are also shown as measured in [11], with the lower singlet lifetime being temperature dependent ($\sim$ 220 ns at room temperature and $\sim$ 450 ns at 5 K). . . 13

1.6 (a) Ground state level structure of the NV center under a small axial magnetic field. Allowed magnetic dipole transitions are shown with double-headed arrows. The values for the ^{14}N hyperfine splitting can be found in Tab. 1.4. The nuclear Zeeman effect is not included and E is taken to be zero here. (b) ODMR spectrum (excited at 532 nm) for a low-defect-density CVD diamond [12]. The 24 separate resonances correspond to two different $|\Delta m_s| = 1$ transitions, four different NV orientations, and three different ^{14}N m_I levels. The spectrum for each orientation are shifted due to an applied field of $\sim$ 50 G. Arrows connect resonances of a given orientation. 16

1.7 Optical and microwave spin-echo pulse sequence used for sensing an AC magnetic field, $b(t)$. NV centers are first polarized into the $m_s = 0$ sublevel. A coherent superposition between the states $m_s = 0$ and $m_s = 1$ (or alternatively $m_s = -1$) is created by applying a microwave $\pi/2$ pulse tuned to this transition. The system freely evolves for a period of time $\tau/2$, followed by a π refocusing pulse. After a second $\tau/2$ evolution period, the electronic spin state is projected onto the $m_s = 0, 1$ (or $m_s = 0, -1$) basis by a final $\pi/2$ pulse, at which point the ground state polarization is detected optically via spin-dependent fluorescence. The optimal sensitivity is achieved for $\tau \approx T_2$, making this magnetometry scheme ideal for kHz-scale AC fields. The DC magnetic field is adjusted to eliminate the contribution of the randomly phased field produced by ^{13}C nuclear spins (Larmor period, $1/\Omega_n$) by choosing $\tau = 2n/\Omega_n$, for integer n. 20

1.8 Illustration of high-spatial-resolution magnetometry with a diamond nanocrystal. (a) The dipolar fields from spins in the sample decay rapidly with distance; only those within a distance $\sim r_o$ contribute to the observable signal for the point-like NV center. The inset shows how B_{max} (the magnetic field produced by fully polarized nuclei) and B_{rms} are related; when few spins are involved, the statistical fluctuations become large. (b) In the presence of a magnetic-field gradient (field lines in grey), only the spins from a small region of the detection volume are precessing at the frequency band center of the detector, enabling even higher spatial resolution. Adapted from [13]. 22

1.9 (a) Diagram of the magnetic field imaging experiment in [14]. A nanoscale magnetic particle (red) is imaged with a single nitrogen-vacancy defect (green, within the blue nanocrystal) fixed at the scanning probe tip (black). A microscope objective is used to focus light from a 532 nm laser on the NV center, exciting the $^3A_2 \rightarrow {}^3E$ transition on the phonon sideband. The same objective collects fluorescence (i.e. confocal microscopy), which is then spectrally filtered and directed to photodetectors. (b) Fluorescence map in the vicinity of the nickel magnet, recorded using a single NV center on the AFM tip as light source and magnetometer. The triangular shaped magnet is black because laser light is reflected off the magnet and consequently no fluorescence is collected in this region. Inset (c), the fluorescence signal from the scanned nitrogen-vacancy center attached to the apex of the AFM tip when resonant microwaves at 2.75 GHz are applied. The arrowed point corresponds to 5 mT resonance line with the magnetic field tilted by 45° relative to the nitrogen-vacancy axis. Adapted from [14]. 24

1.10 (a) Spin-echo measurement for a single NV center more than 1 μm below the diamond surface. The normalized echo signal corresponds to a fractional change in the NV center's fluorescence. Maximal signal corresponds to an average of 0.03 detected photons during the 324-ns photon counting window of a single experimental run. Collapses and revivals are due to interactions with the ^{13}C nuclear spin bath. The revivals occur at half the rate of the Larmor frequency of ^{13}C (here set by B_{DC} = 22 G). The spin-echo signal envelope was fitted with an exponential decay function modulated by a strongly interacting pair of nearby ^{13}C (Methods in [15]. Magnetometer sensitivity experiments are performed at spin-echo revival peaks to maximize signal. (b) Examples of measured spin-echo signal as a function of B_{AC} for two operating frequencies, 3.15 kHz (red) and 4.21 kHz (blue), corresponding to revivals 1 and 2 indicated in a. Each displayed point is a result of 7×10^5 averages of spin-echo sequences. The magnetometer is most sensitive to variations in the AC magnetic field amplitude (δB) at the point of maximum slope, with the sensitivity being limited by the uncertainty in the spin-echo signal measurement (δS). The cosine behavior of the signal with respect to AC magnetic field amplitude can be changed to a sine by adjusting the phase of the third microwave pulse by 90°. This change moves the point of maximum magnetometer sensitivity to near zero AC field amplitude. (c) Measured sensitivity of a single NV magnetometer in a bulk diamond sample over a range of frequencies for the external AC magnetic field after averaging for one second. Error bars, standard deviation (s.d.) for a sample size of 30. Also shown is the theoretically predicted sensitivity (solid blue line), with the shaded region representing uncertainty due to variations in photon collection efficiency. Measurements were carried out at two different DC fields, $B_{DC} = 13$ G (red) and 22 G (green). Adapted from [15]. 25

1.11 (a) Level diagram and optical transitions for the STED scheme. A green pump laser excites NV center's into the ^3E excited state and a depletion beam at 700 nm stimulates emission, quenching fluorescence. (b) Timing diagram of STED for pulsed operation. Continuous-wave operation is also possible as shown in (c). The spatial profile of the pump and STED beams during cw excitation. The level diagrams show that in the intense portion of the STED beam, all NV centers are in the ground state, whereas at the optical vortex, a significant population of NV centers exists in the excited state. 27

1.12 Wide-field fluorescence microscope used for magnetic imaging as described in text. The sample under study would be placed in close contact with the thin layer of NV centers. Adapted from [13]. 29

2.1 (a) Monte-carlo simulation of radiation damage as a function of penetration depth for 2.4-MeV proton radiation, using the SRIM software. (b) Depth profile of NV$^-$ centers, taken by normalizing the integrated ZPL intensity by that of a single NV center, after the first annealing (see text). The concentrations for Sample 10 have been divided by a factor of 10 for visualization. Errors on the concentration estimates are discussed in Sec. 2.4.2.2. (c) NV$^-$:NV^0 ZPL intensity ratio as a function of depth after the first annealing. The lightpower was 100 μW. For Sample 10, beyond a depth of $\sim$ 36 μm, the NV^0 ZPL became indistinguishable from the background. 35

2.2 (a) Depth profiles of the phonon-sideband PL intensity for Sample 10 at a typical location (left) and at a sector boundary (right). (b) Deconvolved intensity as a function of depth for Samples $1, 9,$ and 10 (S1, S2, etc.) after the first annealing at 700, 500, and 800 °C, respectively. The PL intensity is normalized by the incident laser power $(5, 153,$ and 1.9 nW for Samples $1, 9,$ and 10, respectively). The signal for Sample 9 is multiplied by a factor of 100 for visualization. (c) PL deconvolution for Sample 9 after the first and third annealing. The PL intensity after the first annealing has been multiplied by a factor of 30. The damped oscillations are artifacts of the signal processing caused by rapid changes in concentration. 37

2.3 Fluorescence spectrum at each stage of annealing for Sample 2 (see Tab. 2.1), as well as the spectrum of a single NV center in the ultra-pure CVD diamond used for calibrations. The measurement volume is approximately 5.2 μm^3 located $\sim$ 12 μm from the surface. The important spectral features are labeled (as described in the text). (b) Lateral (xy) scans of the ultra-pure CVD diamond showing fluorescence in the $647 - 804$ nm spectral region from two of the single NV centers used to determine the fluorescence collection volume. The range for all of the scans is 30 μm $\times$ 30 μm 41

2.4 (a) NV$^-$ concentrations of electron-irradiated samples as a function of annealing temperature. (b) NV$^-$:NV^0 ZPL intensity ratio of the same samples as a function of annealing temperature. The data were taken during two different runs on separate days. On each day the collection location for each sample was the same, but in between days the location changed. The laser power for the data on each day is indicated in the legend. Filled plot symbols are used for all samples with high nitrogen content and empty symbols represent the two samples with $\lesssim$ 1 ppm nitrogen. Error bars are not shown here but are discussed in the text. 43

2.5 NV$^-$ concentrations near the surface as a function of dose for electron-irradiated samples after the final annealing at 1050°C. The data are the same as used in Fig. 2.4(a). 44

2.6 Room temperature transmission curves for four electron-irradiated samples after the final annealing at 1050°C. The beam path (i.e. the sample thickness) was 1 mm for Samples 1 and 2 (S1 and S2) and .5 mm for S3 and S4. The ZPL at $\sim$ 638 nm is visible for S1 and S2 and is blown up in the inset. The dotted lines represent the baselines used for Sample 1 in the effective vibrational-splitting and Huang-Rhys factor calculations (the baseline for Sample 2 was similar). 46

2.7 Infrared spectra for Samples 1, 2, and "Y1" after the final annealing. Each spectrum represents averaging of 64 scans and the resolution of the spectrometer was set to 0.25 cm^{-1}. The rapid oscillations are due to etaloning at normal incidence, and they have been smoothed by a moving average (black lines) in order to quantify the peak at $\sim$ 1130 cm^{-1} (see text). Features mentioned in the text are labeled by their wavenumbers. 49

2.8 Relative NV$^-$ and NV^0 concentrations for (a) Sample 10 and (b) Sample 4 after the first annealing (700°C and 800°C, respectively) as a function of incident laser power. The concentrations were obtained from fluorescence spectra (insets) taken at a depth of approximately 36 μm, for Sample 10, and 12 μm, for Sample 4. Determination of NV^0 concentration was made by weighting the relative ZPL intensity according to the difference in room-temperature Huang-Rhys factors; $S \sim 3.3$ for NV^0 [16] and $S \sim 4.0$ for the NV$^-$ center (Sec. 2.4.2.4). The laser beam was focused to a diameter of approximately 0.5 μm for all measurements. 51

2.9 (a) Crystallographic cell for the NV center in diamond. The center has C$_{3v}$ symmetry and the line that contains both N and V defines the symmetry axis, of which there are four possible orientations. C–Carbon, N–Nitrogen, V–Vacancy. (b) Level diagram for NV$^-$ center showing spin-triplet ground and excited states, as well as the singlet system responsible for intersystem crossing (see text). The transition wavelengths are for the ZPL, with radiative transitions indicated by solid arrows and non-radiative transitions by wavy arrows. 53

2.10 (a) ODMR spectrum for Sample 3. The 24 separate resonances correspond to two different $|\Delta m_s| = 1$ transitions, four different NV orientations, and three different ^{14}N hyperfine transitions. The orientations were split by a $\sim$ 50 G field. (b) Level diagram for the ground-state magnetic dipole transitions induced by the microwave field in the ODMR measurements. The selection rules for these transitions are $|\Delta m_s| = 1$ and $\Delta m_I = 0$. The values for the ^{14}N hyperfine splitting are taken from Ref. [17]. (c) Microwave-power dependence (log-scale) of the relaxation rate for Sample 4 for a laser power of 213 μW. Microwaves from a signal generator were amplified and applied with a $\sim$ 1-mm-diameter current loop with unmatched impedance. The microwave power was measured at the output of the signal generator prior to the $\sim$ 30 dB amplifier. The FWHM linewidth of each $|\Delta m_s| = 1, \Delta m_I = 0$ transition for one of the orientations was plotted as a function of microwave power. A linear fit for the lowest-power points (dashed line) was used to extrapolate the linewidth to zero microwave power. The standard error in the fit parameter serves as the uncertainty in the measurement. 54

3.1 Zero-field FDMR spectrum at 293 K for S3 and the corresponding fit based on Eq. 3.1 (solid green line). The six blue lines represent the fitted amplitudes at each transition frequency, and the fitted linewidth was 3.3 MHz (full width at half maximum). The microwave power was reduced to ~ -10 dBm to resolve the hyperfine structure, resulting in the relatively small contrast of $\sim$ 0.6%. The best-fit parameters for this scan are $E = 1.4(5)$ MHz and $D = 2869.3(2)$ MHz. 63

3.2 (a) Zero-field FDMR spectra at 283 K and 326 K for S8 with fits (solid red lines). (b) Value of E for S8 as a function of temperature with linear fit (solid black line). (c) D for S8 vs. temperature with linear fit. (d) dD/dT and dE/dT as a function of laser intensity for S5. The dotted lines are the laser-intensity-independent values used in Tab. 3.1. 64

3.3 (a) Fitted value for D as a function of temperature. The microwave field amplitude was $\sim$ 3 mG and excitation was with $\sim$ 1 mW of 532 nm light for all data in (a)-(c). Error bars from the fits in (a)-(b) are smaller than the plotted points. (b) Fitted value of E as a function of temperature. (c) Fitted values of $dD/(DdT)$ as a function of temperature and theoretical temperature dependence based on macroscopic thermal expansion [18], as described in the text. 68

4.1 Level diagram for NV center showing spin-triplet ground and excited states, as well as the singlet system involved in intersystem crossing. Radiative transitions are indicated by solid arrows and non-radiative transitions by dashed arrows. The tentative label of the upper(lower) singlet as ${}^1E({}^1A_1)$ is based on the observed spin-selective decay paths (see text). 71

4.2 (a) Apparatus used for magnetic resonance and optical studies. MC–monochromator. (b) Fluorescence spectrum of the IR transition (excitation at 532 nm) at room temperature for two diamonds with different NV$^-$ concentrations [12] showing a ZPL at 1042.5(3) nm. The sloped background is due to the tail of the phonon sideband of the much-stronger ${}^3E \rightarrow {}^3A_2$ transition [19]. (c) Magnetic-resonance spectra of sample S2 for visible (650-800 nm bandpass filter) and IR (1000 nm longpass filter) emission at room temperature under an applied field of $\sim$ 4 mT. Excitation was with $\sim$ 1 W of 532 nm light, polarized in the plane of the sample surface. The variation in peak heights can be explained by the pump-light and microwave polarization selection rules [20]. 72

4.3 (a) The phase shift technique. (b) Phase shift of visible (650-800 nm) and IR (1035-1045 nm) fluorescence as a function of modulation frequency and fits (see text). (c) Lifetime of the MS as a function of temperature as well as fits to Eq. (4.1). The values of ϵ and $\epsilon_{1,2}$ are the fitted phonon energies for $N = 1$ and $N = 2$ decays, respectively. Error bars represent the standard deviation of multiple measurements. 75

4.4 (a) Example magnetic-resonance spectrum for visible fluorescence and transmission of IR probe at 70 K. As the sample was [111]-oriented, one of the NV axes was normal to the sample surface. (b) Polar plot of the contrast of visible fluorescence (left) and IR absorption (right) as a function of light-polarization angle for both geometries (see text). Solid lines are fits to a constant and dashed lines are fits to $\sin^2(\theta - \phi_{NV}) + c$, where θ is the polarizer angle, ϕ_{NV} is the angle of $\mathbf{z}$ relative to the polarizer axis, and c is an offset which takes into account imperfections in light polarization, beam alignment, and selection rules. For the $\mathbf{z} \perp \hat{\mathbf{k}}$ geometry, the sample and polarizer were positioned such that we expected $\phi_{NV} = 90(3)^\circ$, and both of the fitted values of ϕ_{NV} agree with this value to within the uncertainty. (c) Light-polarization axes for allowed transitions between the singlet levels [21]. The selection rules are identical for both absorption and emission. 77

5.1 (a) Level structure of the NV center and allowed optical transitions. Radiative (non-radiative) transitions are represented by solid (dashed) lines. (b) IR absorption gradiometer apparatus. The green pump and IR probe beams were focused to a diameter of $\sim 30\ \mu$m near the surface of the diamond, and two halves of the transmitted IR beam were detected with separate photodiodes. MW–microwave. 81

5.2 Optically-detected magnetic resonance at 75 K using the fluorescence method and both halves of the transmitted IR probe. The pump power was 0.8 W and the microwave Rabi frequency was ~ 1.5 MHz. 82

5.3 (a) Lock-in signal for both IR magnetometer channels. (b) Time series magnetometer signal, after subtraction of the static bias field, for a 1 $\mu\mathrm{T}_{\mathrm{rms}}$ applied field at 109 Hz. The microwave frequency was tuned to the center of the resonance (zero-crossing in (a)). (c) Frequency-domain response of the magnetometer output in (b) revealing an IR absorption gradiometer noise floor of 7 $\mathrm{nT}_{\mathrm{rms}}$ in 1 s of acquisition. . . 84

List of Tables

1.1 Electronic levels of the NV center in the ground (e^2) and first-excited (a_1e) configurations. The wavefunctions refer to the MOs of the two unpaired electrons, with bars (lack of bars) denoting an electron in the $m_s = -1/2$ ($m_s = +1/2$) state. The spin quantization axis is the symmetry axis of the NV center, labeled $\boldsymbol{z}$ in Fig. 1.3(a). 10
1.2 Light-polarization axes for allowed optical transitions. Note: $A_1 \leftrightarrow A_1$ is forbidden to first order because it would require altering the electronic configuration twice ($e^2 \leftrightarrow a_1a_1$) and $A_2 \leftrightarrow A_2$ is forbidden because there is only one A_2 level in the bandgap. 11
1.3 Products of C_{3v} symmetry states. 11
1.4 Coupling coefficients for the ground-state Hamiltonian in Eq. (1.4) at room temperature. We use units where Planck's constant, $h = 1$. ZFS–zero-field splitting. 15

2.1 Sample characteristics. Initial nitrogen concentration, [N], is given as specified by manufacturer. Each annealing was carried out for $2 - 2.5$ hours. 32
2.2 Sample Characteristics. Final NV$^-$ concentrations for the electron-irradiated samples are tabulated along with initial nitrogen content (reported by the commercial providers) and projected vacancy concentrations. These values are used to set a lower bound on the nitrogen-to-NV$^-$ conversion efficiency, as seen in the last column. The error in NV$^-$ concentration estimates, and consequently the error in conversion efficiency, is a approximately a factor of two, as discussed in the text. 45

2.3 Effective transverse spin relaxation times, T_2^*, extrapolated to zero microwave power, for several electron-irradiated samples at the given laser powers (focused to $\sim$ 0.5-μm diameter). For Sample 5, three locations, corresponding to spots in different growth-sectors, were investigated. The uncertainty estimates for all samples except Sample 3 come from the standard error of the linear fits, as shown in Fig. 2.10(c). For Sample 3, only one low microwave power, -30 dBm before the amplifier, was investigated (shown in Fig. 2.10(a)). The lower bound on T_2^* for this sample corresponds to one standard deviation below the statistical average of the resonance widths. 56

3.1 ZFS parameters and uncertainties for four different samples. The values of E represent the expected value of $E(293\text{ K})$ extrapolated from the linear fits, and the error bars represent the standard error from the fit but not systematic effects due to imperfect assumptions in the model (see text). The laser intensity was $\sim$ 25-50 kW/cm^2 throughout the collection volume. Note that for the S2 spectra a magnetic field of $B_\perp \approx 13$ G was applied. This field enabled the isolation of a single NV orientation, and the simplified spectrum was used to verify the robustness of the model. 65

Acknowledgments

I want to thank my advisor, Dmitry Budker, for sharing his contagious love of physics. He is my favorite person to talk to about physics and research, so I am lucky that he chose to give me countless hours of his time discussing science, designing experiments, providing solutions to technical problems, and supervising manuscript preparation. Thanks also to my committee members Irfan Siddiqi and Robert Littlejohn for guiding me through this process.

I would like to express my gratitude to postdoc Micah Ledbetter who taught me all of the nuts-and-bolts of the research process, and who has helped me on virtually every project I have undertaken as a graduate student. Former and current postdocs/students Derek Jackson-Kimball, Eric Corsini, James Higbie, Kostya Tsigutkin, Damon English, Todor Karaulanov, and Brian Patton have also contributed greatly to this work helping with technical problems and discussing basic physics. Along the way, they became good friends and I hope these relationships continue for many years.

The students and postdocs who contributed the most to this work were Erik Bauch, Andrey Jarmola, and Lucas Zipp. I learned a lot working with them and could not have obtained the results presented here without their tireless contributions. Just as important, it was a lot of fun and I hope to never forget these experiences.

Finally, I want to acknowledge the expert help of collaborators Charles Santori, Kai-Mei Fu, Paul Barclay, Ray Beausoleil, Louis Bouchard, Amir Waxman, Ron Folman, Marcis Auzinsh, Heloise Linget, Wojtek Gawlik, Sergey Chemerisov, Phil Hemmer, Ron Walsworth, Mike Romalis, Irfan Siddiqi, Jean-Francois Treussart, Jean-Francois Roch, Vincent Jacques, Adam Gali, Alex Sushkov, Marcus Doherty, Jeronimo Maze, Fedor Jelezko, Jeorg Wrachtrup, Lillian Childress, Gopi Balasubramanian, Neil Manson, and members of the group of Alex Pines. We entered a somewhat unfamiliar territory when we started in this solid-state magnetometry work, and none of the results presented here would have been possible without their patient advice and essential contributions.

Chapter 1

Physics of nitrogen-vacancy centers in diamond and overview of the field

1.1 Introduction

At the core of modern-day quantum metrology is the ability to obtain long-lived coherences, in the ensemble of spins under study. Since the 1950s, researchers have applied long-lived coherences in alkali vapor cells to measure magnetic fields with record sensitivity [7]. These vapor cell magnetometers now have achieved a better sensitivity [2] than the previously most sensitive superconducting quantum interference devices (SQUIDs) [8] under comparable conditions. These "atomic magnetometers" have been used to detect the nuclear spin magnetization of xenon [22], applicable to the field of magnetic resonance imaging (MRI) of human tissue, and to locate ultra-low-concentration magnetic micro- and nano-particles [23], important in materials science, petrology, and security applications. Ultra sensitive magnetometers have also been used to map the magnetic fields from the human heart and even the brain [24]. Further, remotely-detected nuclear magnetic resonance (NMR) has been demonstrated using microfluidic chips [25], and recently atomic magnetometers were used for the study of isotropic nuclear-spin "J-coupling" interactions in the zero-field environment [26]. Other applications of precision magnetometry include ordnance and explosives detection for defense, space magnetometry, and fundamental physics research, such as searches for permanent electric dipole moments of electrons [27], tests of local Lorentz invariance [28, 29], and the search for new elementary particles such as the axion [30].

Atomic magnetometry was the focus of my first three years of graduate research [31, 32, 33, 34, 35, 36], and provided the foundation for the present work. However, there are areas where the existing technologies and approaches find their limits. While atomic magnetometers can measure magnetic fields with exceptional sensitivity and without cryogenics, spin-altering collisions limit the sensitivity of sub-millimeter-scale sensors [7]. In order to probe magnetic fields with nanometer resolution, magnetic measurements using SQUIDS [8, 37, 38] as well as magnetic resonance force microscopes (MRFMs) [39, 40, 6, 41], have been performed. However, the spatial resolution of the best SQUID sensors is still not significantly better than a few hundred nanometers [5], and both sensors require cryogenic cooling to achieve high sensitivity, which limits the range of possible applications.

Recently, a new technique for measuring magnetic fields at the nanometer scale has emerged based on optical detection of electron spin resonances of nitrogen-vacancy (NV) centers in diamond [14, 15, 42]. This system offers the possibility to detect magnetic fields with an unprecedented combination of spatial resolution and magnetic sensitivity [43, 41, 13, 42, 44], in a wide range of temperatures (from 0 K to well above 300 K), opening up new frontiers in biological [14, 45, 46] and condensed-matter [14, 47, 48] research. Over the last few years, researchers have developed techniques for scanning magnetometry using nanoscale imaging techniques in bulk diamond [15, 42, 49], as well as in nanodiamonds [50, 51, 52] combined with scanning probe techniques [14, 53]. Sensors employing ensembles of NV centers promise even higher sensitivity and the possibility to map out all vector components of the magnetic field [13, 12], and pilot NV-ensemble magnetometers have recently been demonstrated by several groups [48, 47, 54, 44].

The development of these techniques with an eye toward applying them to image novel micro- and nano-scale magnetic phenomena is the focus of this chapter. As a note of caution, we point out that this field is currently exploding. The number of citations to papers related to diamond NV centers has probably increased tenfold or more over the period 2005-2010. With such a rapidly expanding field, we can only review a portion of the relevant literature here, and new techniques will inevitably emerge in the near future. Thus, we focus here on the history of optical magnetometry in diamond, the underlying physics which makes nitrogen-vacancy centers such remarkable sensors, and the basic techniques for utilizing their potential.

1.1.1 Comparison with existing technologies

Sensitivity estimates for NV-based magnetometers compare favorably with the currently most sensitive devices, including SQUIDs and atomic magnetometers. While the ultimate verdict will come from experiments, the prospect of a robust, scalable, solid-state system with a superior operating temperature range (from 0 K to well above room-temperature) has many researchers chomping at the bit.

Spin-based magnetometers are fundamentally limited by the quantum noise associated with spin projection. The minimum detectable magnetic field for a sample of spins with density n in a volume V is given by [7, 13]:

$$\delta B_q \simeq \frac{1}{\gamma}\frac{1}{\sqrt{nVt_mT_2^*}}, \tag{1.1}$$

where $\gamma = 1.761 \times 10^{11}$ $\mathrm{s}^{-1}\mathrm{T}^{-1}$ is the NV gyromagnetic ratio [55], T_2^* is the electron spin dephasing time, and $t_m \gtrsim T_2^*$ is the measurement time.

Figure 1.1 compares the sensitivity and operating temperatures of the currently most sensitive technologies with two types of diamond sensors being developed, a ~ 50 μm-scale sensor [44] for low-field NMR detection [25, 26] and general field use and a 2D surface probe with a spatial resolution of $\sim$ 10 nm [43, 41, 13, 15, 14, 42, 54, 47, 53] for condensed matter [48] and biological [45, 46, 56] applications. At centimeter and longer length scales, vapor-based atomic magnetometers are currently the most sensitive devices, but nanoscale spatial resolution is not possible due to thermal motion of the atoms. By employing a high density of a noble gas, vapor-based magnetometry with a spatial resolution of $\sim$ 10 μm is possible [57], but despite impressive results for mm-scale sensors [58, 25] the projected sensitivity for this length scale is exceeded by the diamond-based sensors presently proposed. Further, for optimal operation, vapor-based cells must be heated to well above room-temperature, which increases the power consumption and limits the range of applications.

In the case of SQUIDs, significantly better spatial resolution is possible, but the operating temperature range is cryogenic, limiting the range of applications. Recently, an Al nano-SQUID was placed on a scanning tip, and the probe of diameter $\sim$ 180 nm demonstrated a sensitivity of $\sim$ 100 $\mathrm{nT}/\sqrt{\mathrm{Hz}}$ [5]. The diamond-based sensors discussed here promise better spatial resolution and comparable magnetic sensitivity without cryogenic operation. MRFM and BEC magnetometers also offer impressive spatial resolution and magnetic sensitivity, however the large magnetic field gradients used in MRFM (approaching 10^6 T/m [39, 59]) and the extreme cryogenic operating temperatures for both BECs and MRFMs are impractical for many applications.

1.2 Historical background

The use of optically detected magnetic resonance (ODMR, defined here as the detection of spin transitions by optical means) for precision magnetometry is not restricted to gas phase atoms, though it did indeed begin there. The first published results related to optically detected magnetic resonance were probably experiments with mercury vapor by Fermi and Rasetti in 1925 [60]. The topic was subsequently refined in a proposal by Bitter in 1949 [61] and experimental demonstrations, first with mercury vapor and later with various alkali vapors, by Brossel, Bitter, and others in the early 1950s [62]. The techniques were first applied to solids, using Cr^{3+} in $\mathrm{Al_2O_3}$ (ruby), by two groups in 1959 [63, 64]. Since then, the advent of high-quality light sources, including modern-day diodes and diode-pumped solid state lasers, has allowed these techniques to be applied in a wide variety of media with numerous applications ranging from quantum information to space science.

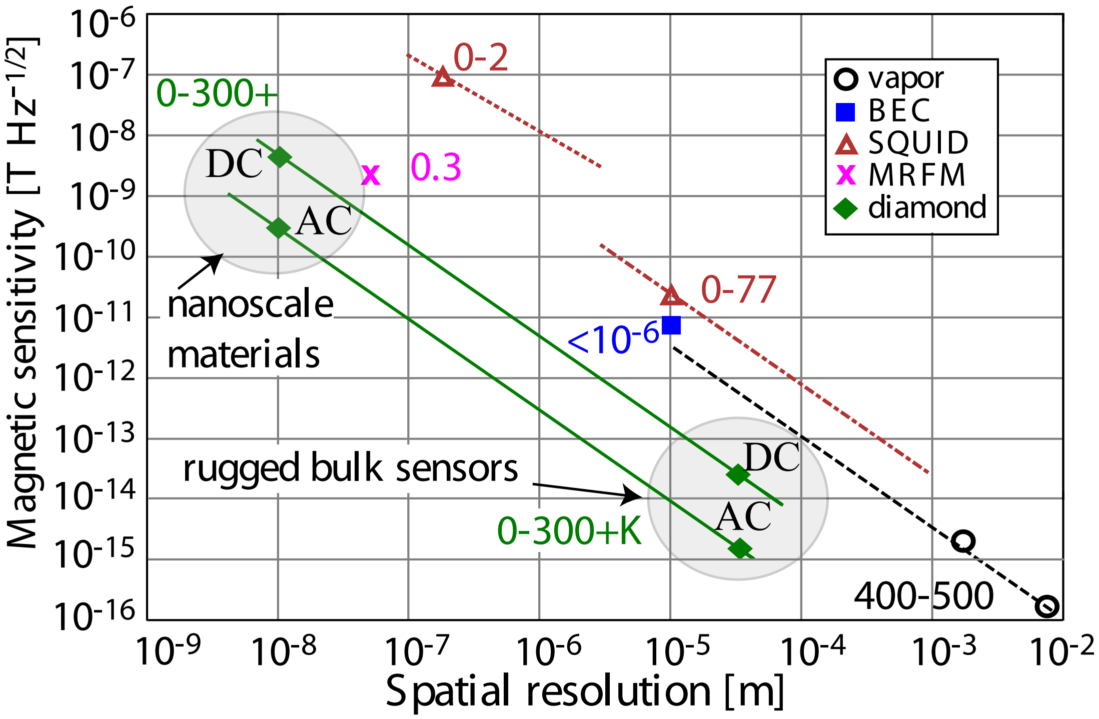

Figure 1.1: Comparison of some of the most sensitive magnetometry technologies. The points for diamond are the projected sensitivities based on Eq. (1.1), and the other points are experimental results for magnetometers based on vapor-cells [1, 2], Bose-Einstein Condensates (BEC) [3], low-frequency micro-SQUIDs [4], nano-SQUIDs [5], and narrowband MRFM [6]. The lines represent the theoretical range and scaling of the spatial resolution for potential sensors based on these technologies (MRFM and BECs have limited range and complicated scaling and are not shown here). Note that the sensitivity scaling with size for all sensors is $\delta B \propto r_{min}^{-3/2}$ (see, for example, [7]) except in the case of nano-SQUIDs (without a pickup coil) where the scaling is $\delta B \propto r_{min}^{-5/4}$ [8]. The numbers are the temperature ranges (in Kelvin) for each sensor as reported in the references.

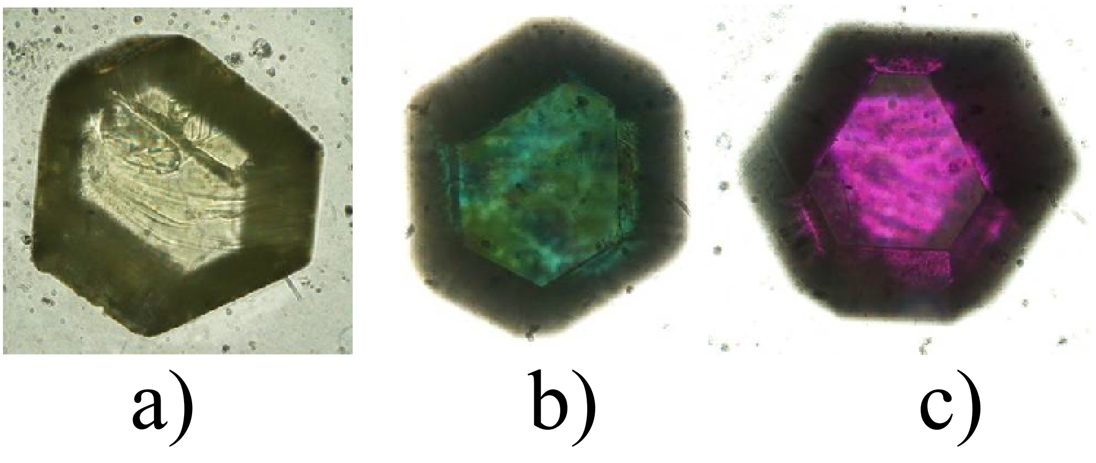

Figure 1.2: Optical microscope image of a $\sim$ 100 μm sized single-crystal HPHT microdiamond (a) after initial growth, (b) after irradiation with 8-MeV electrons at a dose of $\sim 10^{19}$ cm^{-2}, and (c) after annealing at 800° C for 2 hours. Figure courtesy of G. Balasubramanian.

1.2.1 ODMR in diamond

Before ODMR, electron spin resonances (ESR) in solids were traditionally detected by the absorption or reflection of microwaves, with the first such studies reported by Zavoisky in 1945 [65]. In the 1950s this technique was applied to identify the presence of paramagnetic centers in neutron-irradiated diamond [66, 67]. The first specific defect in diamond to be identified via ESR was the single substitutional nitrogen center, known as the P1 center, which was first observed in 1959 [68].

All-microwave ESR continues today to be a powerful analytic tool for bulk samples, but is saddled with two major drawbacks for practical magnetometry. The first is that it usually relies on the thermal Boltzmann distribution to create spin polarization, which means the sensing medium must be cooled and/or subjected to high magnetic fields. For example, even in a 10 T magnetic field, in order to get 75% of free electrons to be “spin down” requires cooling to about 12 K. In contrast $>$ 99% of atomic spins can be polarized into a single spin state at room temperature and zero magnetic field, using optical pumping techniques [69]. The second drawback is associated with the detection of microwave photons. Owing to the $\sim f^2$ frequency-dependence of blackbody and other low-energy radiation background, microwaves are notoriously difficult to detect sensitively, compared to optical frequencies. There currently does not exist a high-quantum-efficiency microwave detector, as an ordinary Si photodiode provides for the optical regime. For these reasons the development of optical techniques has been essential for sensitive spin-based magnetometers.

At the heart of the ODMR technique is the ability to simultaneously drive strong optical transitions (preferably those that can alter the population distribution of magnetically-sensitive states) and narrow radio-frequency transitions between magnetically sensitive states.

Optical transitions in diamond have been known to exist for centuries. Naturally occurring diamonds exist in many different colors, due to isolated defects called color centers (see Fig. 1.2). The study of these color centers has been aided by techniques to grow diamonds in the lab, either by high-pressure-high-temperature synthesis (HPHT, which attempts to mimic the conditions under which diamond is formed in nature) or more recently by chemical vapor deposition (CVD, which enables greater control over the composition and surface properties). Additionally a variety of irradiation techniques, including bombardment by beams of electrons, ions, neutrons, and high-energy electromagnetic rays, have facilitated the production of these color centers in a relatively controlled manner. Indeed more than 600 optical lines have been characterized in Ref. [16]. Figure 1.2 depicts microscope images of a single-crystal HPHT diamond (a) after initial growth (b) after irradiation with high-energy electrons, and (c) after annealing.

Signal enhancement beyond the thermal polarization limit of various ESR-active color centers in diamond under continuous optical excitation was reviewed by Loubser and van Wyck in 1978 [70]. In that work a particularly luminous color center, associated with a substitutional nitrogen atom lying nearest-neighbor to a carbon vacancy (the NV center), was identified and a model for the center involving six valence electrons was proposed and continues to be adopted today. In the late 1980s, optically detected magnetic resonance was observed in high-nitrogen-density, electron-irradiated diamonds [71, 72]. From this and earlier work, it was confirmed that the center was the negatively-charged NV^- center, with ESR transitions occurring in the spin-triplet ground state and optical transitions with an excited state with zero-phonon line at 637 nm [73].

1.2.2 Single-spin ODMR

Given the ubiquity and importance of optical detection of single quantum systems today, it may come as a surprise that it was only first realized in 1980, when Dehmelt and coworkers observed fluorescence from a single trapped Ba ion [74]. ODMR on a single emitter did not come until 1993 when it was realized by two separate collaborations using cryogenic pentacene molecules embedded in a solid [75, 76]. After this groundbreaking work, the search was on to find a suitable room temperature system using technologically relevant materials. In 1997 Jorg Wrachtrup and coworkers found such a system when they performed ODMR at 300 K on single NV centers in diamond [77]. In addition to having a paramagnetic ground state and efficient optical pumping mechanism, it was noted that, unlike most color centers, organic molecules and semiconductor quantum dots, most NV centers in bulk diamond gave a stable fluorescence signal that did not bleach or blink. This feature, combined with the low cytotoxicity of the diamond host [78, 79, 80] makes NV centers in nanodiamonds ideal candidates for fluorescent markers in biological systems [81, 82, 50, 83, 84].

The decade following the initial discovery was marked by major accomplishments in optical and microwave control of the electronic and nuclear degrees of freedom of the NV center and neighboring spins [85, 86, 87, 88, 89, 90, 91, 92, 93, 94]. This progress, combined with the realization of extremely long electron-spin coherence times, for condensed matter standards ($T_2 > 1$ ms for isotopically pure diamond [42]), has quickly made the NV center a leading candidate for qubits in a solid-state quantum computer [95].

During this time, it was also realized that these properties make NV centers an ideal candidate for optical magnetometry [43, 41, 13]. The first realization of a single-spin magnetometer was simultaneously achieved by two groups, one based at Harvard [15] and the other based in Stuttgart [14]. In the last few years several more groups have developed NV-based magnetometers using single spins in bulk diamond [15, 42], in nanodiamonds on scanning tips [14, 53], as well as large ensembles in micron-scale devices [47, 54, 44]. We will review these developments and the underlying physics in the remaining sections.

1.3 NV center physics

1.3.1 Group theory and electron orbitals

The NV center arises when a vacant lattice site lies nearest-neighbor to a substitutional nitrogen atom in the diamond lattice [Fig. 1.3(a)]. Two types of such centers have been identified, the neutral NV^0 center and the singly-charged NV^- center (commonly referred to as the NV center). The latter is of interest to magnetometry because it has a spin-one ground state [70] with a long spin-coherence time [1]. The NV^- center is widely believed to be comprised of six electrons. Three electrons are considered to come from the dangling bonds connecting the vacant site with the three nearest-neighbor (basal) C atoms, two come from the nitrogen-atom's dangling bond, and the other electron is captured from elsewhere in the crystal.

While a complete group theoretical treatment is beyond the scope of this chapter, we provide here a qualitative picture which can be used to understand the basic symmetry and physics of the electronic levels. Using the linear combination of atomic orbitals technique [atomic orbitals labeled c_1, c_2, c_3, and n as in Fig. 1.3(a)], it is possible to construct a set of four molecular orbitals (MOs) which transform as

---

[1] ODMR in the ground state of NV^0 has so far been undetectable, perhaps due to Jahn-Teller distortion [96].

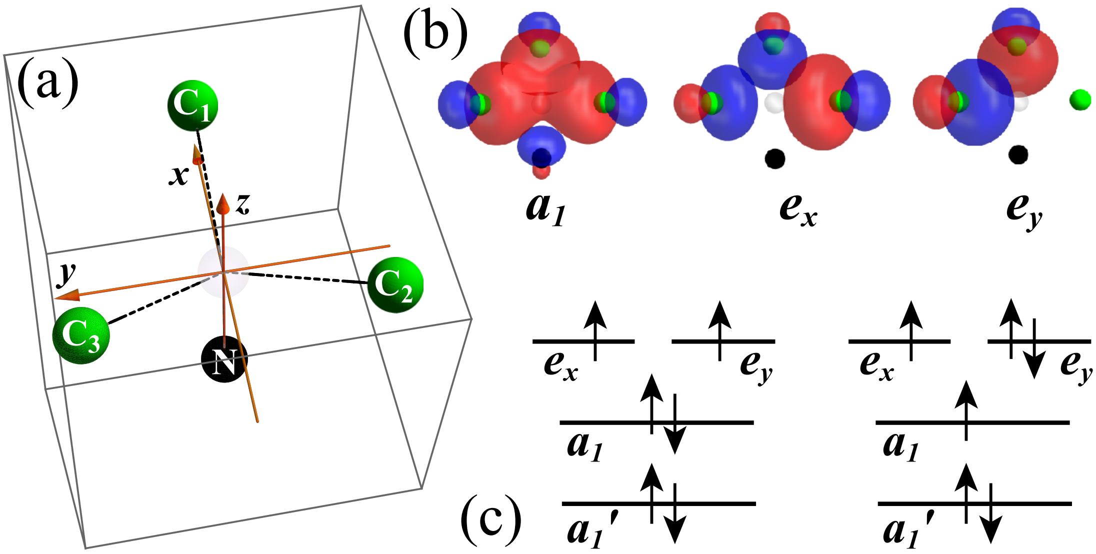

Figure 1.3: (a) Schematic of the NV center with nitrogen, vacancy, and three nearest-neighbor carbon atoms. The geometry and atomic labels are those used to derive the molecular orbitals (MOs). (b) MOs of the three highest-energy single-electron orbitals, a_1, e_x, and e_y. The red (blue) colors denote positive (negative) contributions to the MO. Adapted from [9] with author permission. (c) Schematic of the six-electron configuration for (left) the ground, e^2, and (right) first-excited, a_1e, configurations. The specific wavefunctions depicted here correspond to (left) $\mid e_xe_y\rangle = \mid {}^3A_2, m_s = +1\rangle$ and (right) $\mid a_1e_x\rangle = \mid {}^3E_x, m_s = +1\rangle$. Note that the lowest-energy level, a_1', is predicted to lie below the valence band [10] and experiments have established that the conduction band is well above the e_x, y levels.

irreducible representations of the C_{3v} symmetry group [97, 98, 9]:

$$\begin{cases} a_n = n \\ a_c = c_1 + c_2 + c_3 \\ e_x = 2c_1 - c_2 - c_3 \\ e_y = c_2 - c_3, \end{cases} \tag{1.2}$$

where we have omitted normalization constants. The group-theory-astute reader will notice that a_n and a_c are invariant under all of the C_{3v} symmetry operations and therefore transform as the irreducible representation A_1. The e_x and e_y MOs transform as the rank-two irreducible representation, E [21]. The Coulomb interaction between the electrons mixes a_n and a_c, leading to a new basis of MOs: $\{a_1', a_1, e_x, e_y\}$, where the ordering is dictated by symmetry and the Coulomb interaction [10, 9, 98] and has been confirmed by *ab initio* studies [99, 100, 10, 101, 102]. Figure 1.3(b) approximates the a_1, e_x, and e_y wavefunctions using sp^3 atomic orbitals taken from [9].

The six electrons fill the MOs from lowest to highest energy following Hund's rules. Figure 1.3(c) depicts the electronic configuration in the ground state, labeled e^2 to denote the unpaired electronic density, as well as the first excited configuration, a_1e. Higher-order excited states are theoretically possible but have so far not been observed in experiments [19, 11].

The total electronic wavefunctions of the coupled-electron system, including spin, are obtained by taking appropriate combinations of MOs using a Slater determinant [97, 9, 98]. The resulting states are compiled in Tab. 1.1, where we have omitted spin-orbit coupling, which is often negligible for NV centers in the presence of typical strain fields [103, 104, 105, 106, 92].

1.3.2 Optical selection rules

The selection rules for optical excitation can be determined by considering which matrix elements satisfy:

$$\langle \psi_f | \vec{d} \cdot \vec{E} | \psi_i \rangle \neq 0, \tag{1.3}$$

where ψ_i and ψ_f are, respectively, the initial and final electronic wavefunctions, $\vec{d}$ is the electric dipole moment, and $\vec{E}$ is the optical electric field. The first selection rule which is readily observed from Eq. (1.3) is that ψ_i and ψ_f must belong to different electronic configurations (i.e. $e^2 \leftrightarrow a_1e$). This is because $\vec{d} \cdot \vec{E}$ must change one of the single-electron orbitals in order for the dipole moment to exist. This selection rule can be violated in the presence of electron-vibration or spin-orbit interactions [9, 98], a topic beyond the scope of this chapter.

Another important selection rule is that the electronic spin, S, and its axial projection, m_s must be conserved, in the absence of spin-orbit coupling. This selection

Configuration	$\boldsymbol{C_{3v}}$ **term**	**Spin,** S	**Orbit**	m_s	**Wavefunction**
e^2	${}^3A_2$	1	Singlet	0	$\mid e_x\bar{e}_y\rangle + \mid \bar{e}_x e_y\rangle$
				-1	$\mid \bar{e}_x\bar{e}_y\rangle$
				$+1$	$\mid e_x e_y\rangle$
	${}^1E$	0	X	0	$\mid e_x\bar{e}_x\rangle - \mid e_y\bar{e}_y\rangle$
			Y		$\mid \bar{e}_x e_y\rangle - \mid e_x\bar{e}_y\rangle$
	${}^1A_1$	0	Singlet	0	$\mid e_x\bar{e}_x\rangle + \mid e_y\bar{e}_y\rangle$
a_1e	${}^3E$	1	X	0	$\mid a_1\bar{e}_x + \bar{a}_1 e_x\rangle$
				-1	$\mid \bar{a}_1\bar{e}_x\rangle$
				$+1$	$\mid a_1 e_x\rangle$
			Y	0	$\mid a_1\bar{e}_y\rangle + \mid \bar{a}_1 e_y\rangle$
				-1	$\mid \bar{a}_1\bar{e}_y\rangle$
				$+1$	$\mid a_1 e_y\rangle$
	${}^1E$	0	X	0	$\mid a_1\bar{e}_x\rangle - \mid \bar{a}_1 e_x\rangle$
			Y		$\mid a_1\bar{e}_y\rangle - \mid \bar{a}_1 e_y\rangle$

Table 1.1: Electronic levels of the NV center in the ground (e^2) and first-excited (a_1e) configurations. The wavefunctions refer to the MOs of the two unpaired electrons, with bars (lack of bars) denoting an electron in the $m_s = -1/2$ ($m_s = +1/2$) state. The spin quantization axis is the symmetry axis of the NV center, labeled $\boldsymbol{z}$ in Fig. 1.3(a).

rule may be counterintuitive to readers working with alkali atoms, in which the spin-orbit interaction can be many THz and therefore total spin projection can be altered optically. In the NV center, spin-orbit coupling does split the ${}^3E$ orbitals by ~ 5 GHz [106], so at low temperature and in the absence of strain $\Delta m_s = \pm 1$ optical transitions are allowed and have served as the basis of a recent spin-photon entanglement experiment [92]. However under most operating conditions, either phonon-induced orbital averaging in the ${}^3E$ excited state [107, 106, 108] or strain shifts due to local environment overwhelm the spin-orbit coupling, and consequently the probability for $\Delta m_s = \pm 1$ transitions is typically less than 1% of that of the allowed transitons [91, 92]. Another way to realize spin-non-conserving optical transitions is to tune magnetic sublevels to a near degeneracy either in the ground state, as first seen in [109], or in the excited state [105, 110].

Group theory gives us a convenient way to evaluate which of the rest of the matrix elements satisfy expression (1.3). Suppose $\vec{d}\cdot\vec{E}$, ψ_i, and ψ_f transform as C_{3v}irreducible representations F, G, and H, respectively. Then expression (1.3) will only be satisfied if the tensor product $F\otimes G\otimes H$ includes the symmetric representation, A_1. Intuitively this can be seen because if the inner product is an odd function then integration over all space will give zero net contribution. For C_{3v} symmetry, the position operator $\hat{z}$ transforms as A_1, and $\{\hat{x}, \hat{y}\}$ transform as $E_{x,y}$. Table 1.2 displays the optical selection

	$\boldsymbol{A_1}$	$\boldsymbol{A_2}$	$\boldsymbol{E_x}$	$\boldsymbol{E_y}$
$\boldsymbol{A_1}$			$\hat{x}$	$\hat{y}$
$\boldsymbol{A_2}$			$\hat{x}$	$\hat{y}$
$\boldsymbol{E_x}$	$\hat{x}$	$\hat{x}$	$\hat{x}, \hat{z}$	$\hat{x}+\hat{y}$
$\boldsymbol{E_y}$	$\hat{y}$	$\hat{y}$	$\hat{x}+\hat{y}$	$\hat{y}, \hat{z}$

Table 1.2: Light-polarization axes for allowed optical transitions. Note: $A_1 \leftrightarrow A_1$ is forbidden to first order because it would require altering the electronic configuration twice ($e^2 \leftrightarrow a_1a_1$) and $A_2 \leftrightarrow A_2$ is forbidden because there is only one A_2 level in the bandgap.

	$\boldsymbol{A_1}$	$\boldsymbol{A_2}$	$\boldsymbol{E}$
$\boldsymbol{A_1}$	A_1	A_2	E
$\boldsymbol{A_2}$	A_2	A_1	E
$\boldsymbol{E}$	E	E	$A_1 + A_2 + E$

Table 1.3: Products of C_{3v} symmetry states.

rules for different light polarizations for each of the possible C_{3v} terms, $\{A_1, A_2, E_{x,y}\}$. Table 1.3 shows the multiplication table used to make these calculations.

1.3.3 Absorption and fluorescence spectra

Until now we have considered only radiative optical transitions. However phonons also play an important role in both the optical transitions and spin dynamics of the NV center. The most obvious example is in the absorption and laser-induced-fluorescence spectra shown in Fig. 1.4. It is well established that the ground state of the NV center is $^3A_2(e^2)$ [71]. Owing to the optical selection rules discussed in Sec. 1.3.1, the only fully-allowed optical transition out of the ground state is to $^3E(a_1e)$. This transition can be excited resonantly at 637 nm [73], but it turns out that at room temperature a more efficient way to excite this transition is to use green, or even white, light.

To understand why this is the case, we model the $^3A_2$ and ^3E levels as harmonic wells with discrete vibrational levels, as illustrated in Fig. 1.4(a). In thermal equilibrium at room temperature, about 90% of NV centers will be in the lowest vibrational level, corresponding to an effective vibrational spacing of $\sim$ 50 meV [2]. According to the Franck-Condon principle, the most probable vertical transitions are to the turning point in the ^3E harmonic well, which corresponds to about 4 vibrational quanta ($\sim$ 0.2 eV). Such a large shift occurs because the e^2 and a_1e configurations

---

[2] We say here "effective" energy splitting because in reality these vibrational levels are so strongly coupled to the continuum of delocalized phonons that there are no clearly discrete levels.

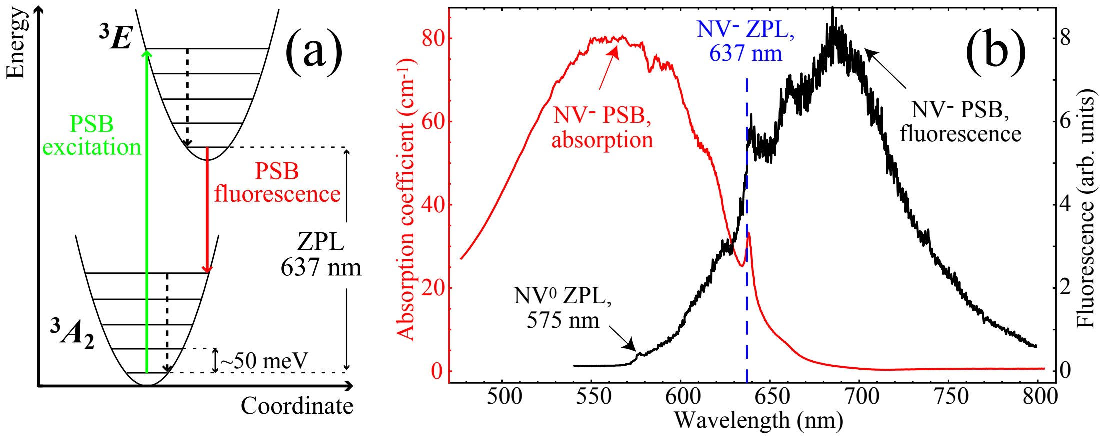

Figure 1.4: (a) Schematic illustrating the Franck-Condon principle for excitation and fluorescence of the main optical transition, $^3A_2 \leftrightarrow {}^3E$. Non-radiative decay is shown with dashed lines. (b) Room-temperature optical absorption and fluorescence (excited at 532 nm) spectra for an HPHT diamond with [NV$^-$] $\approx$ 15 ppm. Besides the spectral features attributed to the NV$^-$ center discussed in the text, the weak line at 575 nm is present from the NV^0 ZPL. PSB–Phonon sideband, ZPL–zero-phonon line.

have significantly different nuclear coordinates, which has been confirmed in *ab initio* studies [111]. This accounts for the broad peak in the absorption spectrum in Fig. 1.4(b) at around 560 nm. This broad peak is known as the phonon sideband (PSB), since the NV center nearly immediately decays back to the ground vibrational level in ^3E non-radiatively. The same principle holds for emission, producing the maximum fluorescence on the PSB at $\sim$ 700 nm. The resonant transition occurs at 637 nm between the ground vibrational levels in both $^3A_2$ and ^3E, and is consequently called the zero-phonon line (ZPL).

Based on the absorption spectrum, it is possible to estimate the electron-phonon coupling parameter, also known as the Huang-Rhys factor [112], $S = -\ln(I_{ZPL}/I_{tot})$, where I_{ZPL} and I_{tot} refer to the integrated absorption intensities after normalization by the light frequency [3]. Analysis of the data in Fig. 1.4(b) gives $S = 3.9(3)$ [12], which is comparable to values seen elsewhere in the literature [114, 73]. The Huang-Rhys parameter physically corresponds to the mean number of vibrational quanta involved in the optical transition.

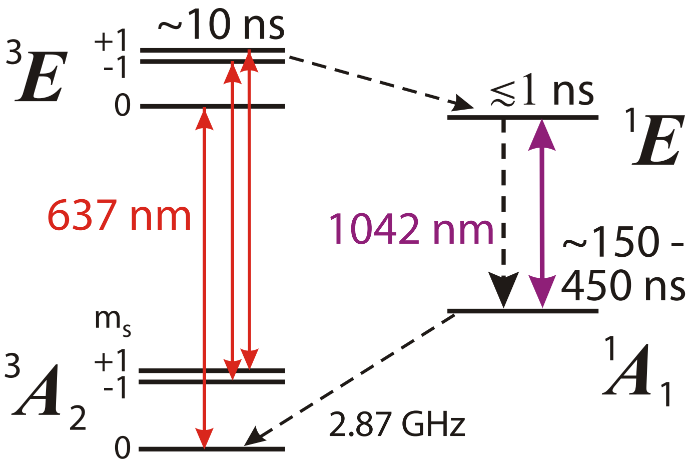

Figure 1.5: Level diagram for the NV center showing spin-triplet ground and excited states, as well as the singlet system involved in intersystem crossing. Radiative transitions are indicated by solid arrows and non-radiative transitions by dashed arrows. Only those transitions confirmed by experiments are shown. The tentative label of the upper (lower) singlet as ^1E ($^1A_1$) is based on the observed spin-selective decay paths (see text). Lifetimes of the excited levels are also shown as measured in [11], with the lower singlet lifetime being temperature dependent ($\sim$ 220 ns at room temperature and $\sim$ 450 ns at 5 K).

1.3.4 Intersystem crossing and optical pumping

One of the crucial features of nitrogen-vacancy centers for practical magnetometry is that they can be optically pumped and interrogated using visible light over a broad range of wavelengths ($\sim$ 480-640 nm). Figure 1.5 shows the level diagram with energy levels and allowed transitions labeled according to a recently proposed model [19, 102, 11]. As discussed in Sec. 1.3.3, the center's ground state is a $^3A_2$ spin triplet and optical transitions are with a spin-triplet excited state, ^3E, with ZPL at 637 nm. In thermal equilibrium at temperatures above $\sim$ 1 K, the ground state sublevels are nearly equally populated. After interaction with sufficiently intense light exciting the $^3A_2 \rightarrow {}^3E$ transition, the $m_s = \pm 1$ sublevels become depopulated, and eventually 80% or more of the total population accumulates in the $m_s = 0$ ground state [115, 55, 89, 116, 117].

This occurs because at least one singlet level lies close in energy to ^3E, and spin-orbit coupling induces triplet-singlet intersystem crossing (ISC). Experiments have shown that NV centers in the $m_s = \pm 1$ magnetic sublevels have significantly higher

---

[3] While this relationship is only strictly correct at zero-temperature where quadratic electron-phonon coupling is suppressed, it was shown in Ref. [112] that, for NV$^-$ centers, the temperature-dependence of S is weak. The ZPL does narrow considerably, eventually reaching the limit set by the spontaneous emission rate, $\sim$ 13 MHz [113], but the integrated area remains roughly the same.

probability to undergo ISC [19, 11, 44, 117]. NV centers which undergo ISC then decay to another, longer-lived singlet level (ZPL at 1042 nm) [19, 11, 44], after which they cross over predominately to the $m_s = 0$ sublevel of the $^3A_2$ ground state.

By determining the optical polarization selection rules (Tab. 1.2), experiments [11] have shown that the levels involved in the ISC include ^1E and $^1A_1$ [4]. However the ordering of these levels is still under debate. If the ISC involves only symmetric vibrations (i.e. phonons that transform as A_1), the observed spin polarization in $m_s = 0$ leads to the prediction that the lower, longer-lived singlet is $^1A_1$. This is because $m_s = 0$ transforms as A_2, while singlets transform as A_1, and, in the group-theoretic language of Sec. 1.3.1, $\langle ^3A_2, m_s = 0 \mid A_1 \mid {}^1A_1 \rangle \neq 0$ because $(A_2 \otimes A_2) \otimes A_1 \otimes (A_1 \otimes A_1) = A_1$. Similarly, $m_s = \pm 1$ transform as E, so $\langle ^3A_2, m_s = \pm 1 \mid A_1 \mid {}^1A_1 \rangle = 0$ because $(A_2 \otimes E) \otimes A_1 \otimes (A_1 \otimes A_1) = E$. The reader can verify that if the lower singlet were ^1E then spin polarization would be in $m_s = \pm 1$ under the same symmetric phonon assumption. This ordering of levels is supported by some recent *ab initio* calculations [102]. However, the ordering is still debated because it is known that transverse phonons (which transform as E) do play a role in the NV center's spin dynamics [108], and some theoretical calculations predict the $^1A_1$ singlet to lie closest in energy to ^3E [101, 9].

Regardless, it is clear that optical excitation results in spin polarization into $m_s = 0$. Furthermore, as the ISC mechanism is mostly non-radiative [19, 11], NV centers in $m_s = 0$ have a higher probability (per excitation cycle) for fluorescence than those in $m_s = \pm 1$. For dilute samples this fluorescence contrast can be as high as 30%, limited by the difference in branching ratios between $m_s = 0$ and $m_s = \pm 1$ into and out of the singlet system [104, 14]. This spin-selective fluorescence serves as the basis for optical readout in most magnetometry schemes to date [14, 15, 42, 54, 47, 53, 48].

1.3.5 Ground-state level structure and ODMR based magnetometry

The level structure in the $^3A_2$ ground state is governed by the Hamiltonian $\mathscr{H}_{tot} = \mathscr{H}_S + \mathscr{H}_{SI} + \mathscr{H}_I$, where $\mathscr{H}_S$ refers to the part which affects only the electronic spin ($S = 1$), $\mathscr{H}_{SI}$ is the hyperfine coupling to the nitrogen nucleus ($I = 1$ for ^{14}N) [5], and

---

[4] We note that there exists some evidence that a third level may be involved in the ISC, though the nature of this level is still unknown [11, 117].

[5] In natural abundance, nitrogen is composed of 99.6% of ^{14}N, with spin $I = 1$, and 0.4% of ^{15}N, with spin $I = 1/2$. We choose to treat only the more naturally abundant ^{14}N nuclei, though there has been some work related to selective implantation and growth of ^{15}NV centers [17].

$\mathscr{H}_I$ is the nuclear portion. These terms can be written as [6]:

$$\begin{cases} \mathscr{H}_S = DS_z^2 + E(S_x^2 - S_y^2) + g_s\mu_B\vec{B}\cdot\vec{S} \\ \mathscr{H}_{SI} = A_\parallel S_z I_z + A_\perp(S_x I_x + S_y I_y) \\ \mathscr{H}_I = PI_z^2 - g_I\mu_N\vec{B}\cdot\vec{S}, \end{cases} \tag{1.4}$$

where μ_B is the Bohr magneton, μ_N is the nuclear magneton, and the other coefficients are defined in Tab. 1.4, along with experimental values.

Coefficient	**Description**	**Value**	**Ref.**
D	axial ZFS parameter	2.87 GHz	[118]
E	transverse ZFS parameter	kHz – MHz	[77, 118]
g_s	electron-spin g-factor	2.003	[55]
$A_\parallel$	axial hyperfine constant	−2.16 MHz	[119]
$A_\perp$	transverse hyperfine constant	−2.7 MHz	[55]
P	quadrupole splitting parameter	−4.95 MHz	[119, 120]
g_I	nuclear-spin g-factor	0.403	[55]

Table 1.4: Coupling coefficients for the ground-state Hamiltonian in Eq. (1.4) at room temperature. We use units where Planck's constant, $h = 1$. ZFS–zero-field splitting.

Figure 1.6(a) displays the fine and hyperfine structure of the ${}^3\mathrm{A}_2$ ground state. The ground state is split by $D \approx 2.87$ GHz due to spin-spin interaction between the unpaired electrons [70, 118]. Here we take $E = 0$, conserving perfect C_{3v} symmetry, and discuss the effect of non-zero E in Sec. 1.3.6. In the presence of a small axial magnetic field, $B_z << D/(g_s\mu_B)$, the $|m_s = \pm1\rangle$ levels split, each one shifting by $m_s g_S \mu_B B_z$. Additional structure due to coupling to ^{14}N nucleus is shown with $m_I = 0$ level separated from $m_I = \pm1$ by $P \pm A_\perp$.

The selection rules for magnetic dipole transitions are $\Delta m_s = \pm1$ and $\Delta m_I = 0$. These transitions can be driven by an oscillating magnetic field oriented perpendicular to the NV axis. For a single NV center, there are six allowed transitions, as indicated in Fig. 1.6(a). For ensembles, there are four different NV orientations and, since only the projection of a small magnetic field on the N-V axis affects the transition frequency, this leads to four shifted copies of the single spectrum. For special magnetic field orientations (i.e. along the [100] crystal orientation), B_z is the same for all four NV orientations, producing only six resonances. However for most field orientations, B_z is different for each N-V orientation, and consequently there are 24

---

[6] While, in natural abundance, 98.9% of C atoms are ^{12}C ($I = 0$), some NV centers also have a nearby ^{13}C atom, and consequently further level structure can exist and has been studied extensively [70, 10, 55]. We will not consider these special centers here, instead focusing on decoherence and line broadening due to coupling to the bath of randomly located ^{13}C spins in Sec. 1.3.7.

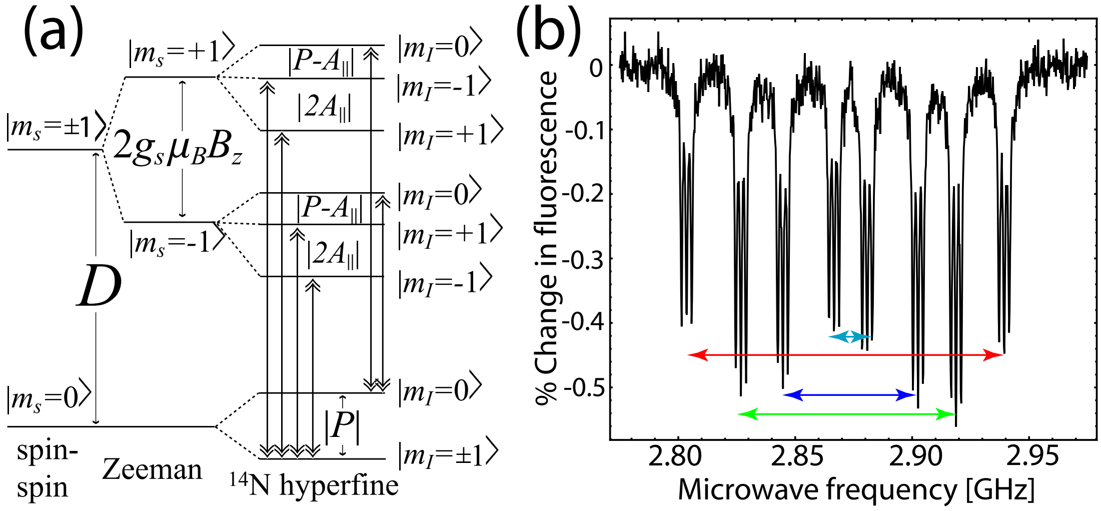

Figure 1.6: (a) Ground state level structure of the NV center under a small axial magnetic field. Allowed magnetic dipole transitions are shown with double-headed arrows. The values for the ^{14}N hyperfine splitting can be found in Tab. 1.4. The nuclear Zeeman effect is not included and E is taken to be zero here. (b) ODMR spectrum (excited at 532 nm) for a low-defect-density CVD diamond [12]. The 24 separate resonances correspond to two different $|\Delta m_s| = 1$ transitions, four different NV orientations, and three different ^{14}N m_I levels. The spectrum for each orientation are shifted due to an applied field of $\sim$ 50 G. Arrows connect resonances of a given orientation.

different resonances. This feature makes diamond magnetometers fundamentally vector magnetic sensors, enabling measurement of not only the magnitude but also the direction of an external magnetic field [20, 13, 121, 47, 54].

A fluorescence detected magnetic resonance spectrum of such a scenario is shown in Fig. 1.6(b). When the microwave frequency is off resonance, optical transitions are predominately from $|\, {}^3A_2, m_s = 0\rangle \leftrightarrow |\, {}^3E, m_s = 0\rangle$ and the fluorescence is at maximum intensity. When the microwaves are tuned to resonance, population is transferred to $m_s = \pm 1$, resulting in non-radiative ISC and consequently diminished fluorescence intensity. This is the basic principle of operation of most diamond-based magnetometers to date [14, 15, 42, 54, 47, 44, 48, 53].

1.3.6 Effect of zero-field splitting on sensitive magnetometry

As seen in Tab. 1.4, the largest term in $\mathscr{H}$is given by the axial zero-field splitting parameter, D. The origin of D is expected to be predominately due to dipolar spin-spin coupling between the two unpaired electrons forming the center [70, 97, 122, 118],

$$D \propto \langle (r_{12}^2 - 3z_{12}^2)/r_{12}^5 \rangle, \tag{1.5}$$

where r_{12} is the displacement between the two spins, and z_{12} is the component of r_{12} along the N-V symmetry axis.

Recently [118], it was discovered that D is highly dependent on temperature near room temperature with a slope $dD/dT \approx -75$ kHz/K. In that work, it was proposed that a likely mechanism for the temperature variation is local lattice expansion, which effectively changes the displacement of the electronic spins, r_{12}. The sharp temperature dependence of D presents a technical challenge for room-temperature magnetometry. Even if the ambient temperature can be controlled at the 1-mK level, this would lead to fluctuations in the resonance frequency of 80 Hz corresponding to a magnetic-field variation of 3 nT. Monitoring both of the $\Delta m_s = \pm 1$ resonances could provide a mechanism for controlling this effect, since the energy difference between these resonances depends only on the magnetic field projection and not depend on D. Alternatively, using two phase synchronized microwave tones [92] to produce coherence and observe precession directly amongst the $m_s = \pm 1$ levels could be employed [7].

The presence of non-zero transverse splitting parameter, E, produces another challenge for sensitive magnetometry. The E parameter arises from interaction with stray electric fields in the lattice. A slight mixing in the ground state with E_x and E_y excited-state orbitals produces a transverse dipole moment of order 10 Hz/(V/cm)

---

[7] While these schemes would mitigate deleterious effects of non-zero dD/dT, any temperature variation in g_s would still produce magnetometer noise, particularly in applications which look for small deviations on top of a large DC field. While dg_s/dT has not yet been studied, recent NV-ensemble magnetometry results [44] demonstrating $\sim 10\ \mathrm{nT}/\sqrt{\mathrm{Hz}}$ sensitivity under a 4 mT bias field are promising.

[123]. Neglecting interaction with the nitrogen nucleus, and diagonalizing $\mathscr{H}_S$ under a small axial magnetic field, B_z, the allowed microwave transition frequencies, $\nu_\pm$, are obtained:

$$\nu_\pm = D \pm \sqrt{E^2 + (g_s \mu_B B_z)^2}. \tag{1.6}$$

From this equation, we can see that transition frequencies are only quadratic in the magnetic field for $|B_z| \lesssim E/(g_s\mu_B)$. In order to measure small variations in magnetic field, it is therefore necessary to apply an axial bias field, $|B_z| >> E/(g_s\mu_B)$.

In high-purity samples that have not undergone irradiation or implantation, the local electric fields can be relatively small, corresponding to kHz-scale E values [106, 124]. In such samples, which are best suited for single-NV magnetometers, only a moderate 100 μT-scale bias field is necessary to reinforce magnetometer linearity. Using a current source with a stability of ppm/$\sqrt{\text{Hz}}$ would be sufficient to achieve the sub-nT/$\sqrt{\text{Hz}}$ required for many applications [8].

In high-defect-density samples necessary for ultra-sensitive ensemble magnetometers [12], typical E values are MHz-scale and highly variable from center-to-center, leading to inhomogenous broadening of the magnetic-resonance lines and quadratic field sensitivity for small fields. In this case the bias field typically needs to be of order 1 mT. Such bias fields are difficult to control at the sub-nT/$\sqrt{\text{Hz}}$ level, and ultra-low-noise current sources [125] may be required. Alternatively, gradiometry techniques [44] which cancel common-mode magnetic noise can be employed to overcome this problem.

1.3.7 Interaction with environment

The NV center's spin is largely decoupled from the lattice, and the main sources of decoherence (characterized by T_2 and T_2^* timescales) are from the paramagnetic-impurity spin bath (which dominates for high nitrogen concentration) and interactions with spin-1/2 ^{13}C nuclei [13, 126, 127, 128, 42, 12]. Population decay (characteristic timescale T_1) is primarily dominated by interaction with lattice phonons [129, 127]. Under most doping conditions, $T_1 >> T_2 >> T_2^*$, in stark contrast to dense alkali vapor where these timescales are often nearly equal. Below, we give a brief overview of contributions to dephasing and techniques to reach the T_2 and even T_1 limit.

1.3.7.1 Contributions to T_2^*

A well-known cause of spin dephasing is due to dipolar hyperfine coupling with nearby ^{13}C nuclear spins (natural 1.1% abundance s). These nuclear spins are largely unpolarized [130] and produce different effective magnetic fields at the site of each NV center, leading to inhomogenous broadening of ensemble resonances. Even single NV centers are affected by the ^{13}C spin bath since the unpolarized nuclei precess in the presence of applied or nearby-defect-induced fields, producing a superposition of time-varying magnetic fields with random phase [126]. Based on experiments with single NV centers, this contribution to the spin relaxation rate is $\gamma_C \approx 10^6$ s^{-1} [87, 128, 42], and similar results have been reported for ensembles [12, 55]. At very low magnetic fields, $|B_z| << E/(g_s\mu_B)$, the NV center is relatively immune to Zeeman shifts (Sec. 1.3.6), and extremely long values of $T_2^* \approx 40$ μs have been observed for $m_I = 0$ nuclear spin sublevels in single NV centers [124]. Unfortunately this regime is not suitable for magnetometry for the same reason T_2^* is long (i.e. insensitivity to magnetic fields). A more promising route is to fabricate isotopically pure diamond, where even longer T_2^* times are possible [128, 42].

---

[8] In fact, if ODMR linewidths are sufficiently narrow, such that hyperfine structure can be resolved, one can do away with the bias field almost entirely. This is because the $m_I = \pm 1$ sublevels are insensitive to strain and do split linearly with magnetic field even near zero field [124]. In this case, a zero-field magnetometer could be realized by using circularly polarized microwaves to selectively excite the relevant $\Delta m_s = \pm 1$ coherences [20].

For dilute samples, the contribution of NV$^-$–NV$^-$ dipolar interactions to the magnetic-resonance broadening can be approximated by assuming that each NV$^-$ center couples to only the nearest-neighboring NV$^-$ center. For an ensemble, this dipolar coupling leads to a spin-relaxation contribution on the order of $\gamma_{NV} \approx (g_s\mu_B)^2 n_{NV}$, where n_{NV} is the NV$^-$ concentration [13, 12]. For [NV$^-$] = 15 ppm, this corresponds to $\gamma_{NV} \approx 10^6$ s^{-1} $\approx \gamma_C$. For ensemble magnetometry using natural-carbon-abundance material, it is worth noting that increasing $[NV^-]$ beyond this level would not improve magnetometer sensitivity, since now $1/T_2^* \propto n_{NV}$ [recall Eq. (1.1)].

A figure of merit for fabricating optimized diamond samples for ensemble work is the nitrogen-to-NV$^-$ conversion efficiency. It is generally assumed that two nitrogen atoms are required to form an NV$^-$ center, one to contribute the actual atom and the other to serve as the donor [131, 12]. The remaining N^+ is not paramagnetic, but the NV centers and any unconverted nitrogen atoms are. For sufficiently high nitrogen concentration and nitrogen-to-NV$^-$ conversion efficiency of less than 33%, unconverted nitrogen is the main source of NV$^-$ dephasing and dominates over γ_C. Similarly to the estimate for NV$^-$–NV$^-$ interactions, the characteristic timescale for this dephasing is $\gamma_N \approx (g_s\mu_B)^2 n_N$, where we ignore the small difference in g-factors between NV$^-$ and nitrogen [70]. Conversion efficiencies of $\sim$ 20% [12, 132] are now routine for large ensembles, and even higher conversion efficiencies are possible under some conditions [133].

1.3.7.2 Refocusing the dephasing

Coherent-control techniques can improve the sensitivity for kHz-scale AC fields. As nuclear spins are well-protected from the environment, the characteristic correlation times for nuclear spin flips are long compared to T_2 of the NV center. A spin-echo pulse sequence [134] can be employed to remove the effect of these slowly-varying environmental perturbations. Figure 1.7 shows a timing diagram for such a pulse sequence. NV center are first prepared in the $m_s = 0$ state and then precess due

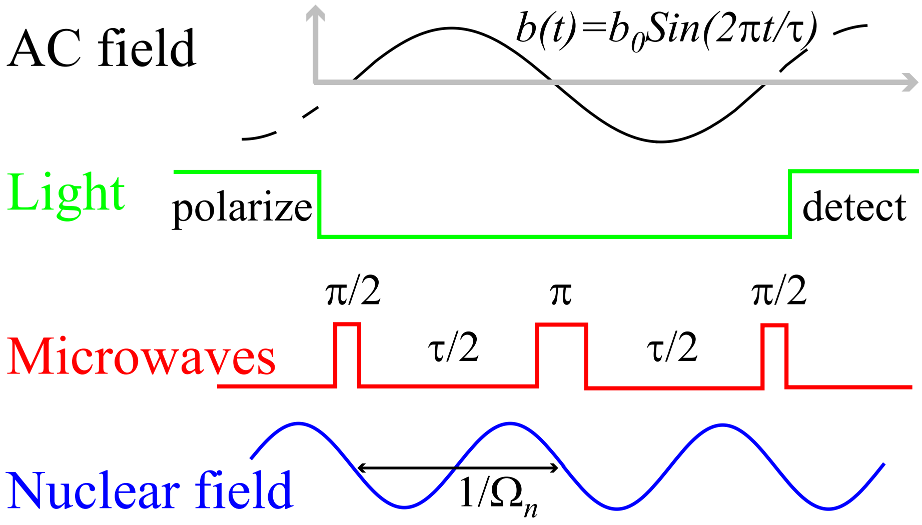

Figure 1.7: Optical and microwave spin-echo pulse sequence used for sensing an AC magnetic field, $b(t)$. NV centers are first polarized into the $m_s = 0$ sublevel. A coherent superposition between the states $m_s = 0$ and $m_s = 1$ (or alternatively $m_s = -1$) is created by applying a microwave $\pi/2$ pulse tuned to this transition. The system freely evolves for a period of time $\tau/2$, followed by a π refocusing pulse. After a second $\tau/2$ evolution period, the electronic spin state is projected onto the $m_s = 0, 1$ (or $m_s = 0, -1$) basis by a final $\pi/2$ pulse, at which point the ground state polarization is detected optically via spin-dependent fluorescence. The optimal sensitivity is achieved for $\tau \approx T_2$, making this magnetometry scheme ideal for kHz-scale AC fields. The DC magnetic field is adjusted to eliminate the contribution of the randomly phased field produced by ^{13}C nuclear spins (Larmor period, $1/\Omega_n$) by choosing $\tau = 2n/\Omega_n$, for integer n.

to a resonant $\pi/2$ microwave pulse[9]. During this precession window, the nuclear spins also precess, in the presence of a bias magnetic field, with random phase at angular frequency Ω_n. If this precession is not synchronized with the echo sequence then it leads to a time-varying magnetic field which dephases the NV center. However, if the echo sequence is timed such that the interval between pulses, $\tau/2$ is commensurate with an integral number of nuclear spin Larmor periods, the overall phase accumulation due to the nuclear field is refocused leading to a revival in the NV coherence [135]. We note that to realize maximum refocusing, it is necessary to position the bias field along the NV axis to within a few degrees to ensure that nuclear spins precess uniformly [86, 126, 56].

In essence, the spin echo technique enables extension of the interrogation time from the limit set by T_2^* up to a value T_2 that is close to the intrinsic spin coherence time, at the cost of reduced bandwidth and insensitivity to magnetic field frequencies $\lesssim 1/T_2$. These techniques have been used to improve the sensitivity of diamond magnetometers by more than an order of magnitude to kHz-scale AC fields of known phase [14, 15, 42, 56] as well as more modest improvements in sensitivity to randomly fluctuating fields [136, 137].

Other pulse sequences can be used to further decouple the NV center from its environment. Examples include Mansfield, Rhim, Ellis and Vaughan (MREV) sequences to refocus NV–NV coupling [13, 138] and Carr-Purcell-Meiboom-Gill (CPMG) or Uhrig dynamic decoupling (UDD) pulse sequences to further reduce coupling to all environmental spins [13, 136, 139, 140]. Using these techniques, room-temperature T_2 times of a few ms have been realized using ultrapure diamond [139, 140] and a few hundred μs for nitrogen-rich HPHT diamond [101]. The ultimate limit, of course, is T_1 relaxation due to interaction with the lattice. In most samples, at room temperature, $T_1 \approx 10$ ms, but it is highly temperature dependent [129, 115, 127], and low-temperature devices with coherence times of seconds, or even minutes, may be possible.

1.4 Experimental realizations

Most demonstrations of diamond magnetometry to date can be grouped into the following categories: near-field scanning probes, far-field sub-wavelength probes, wide-field array magnetometers, and bulk micron-scale sensors. For the remainder of this chapter, we review the state of the art and discuss magnetometer design principles.

---

[9] For completeness, we must mention that if one considers all three levels in the ground state, this pulse is really not a $\pi/2$ pulse. It is only a $\pi/2$ pulse in a reduced space which includes only the $m_s = 0$ and one of the $m_s = \pm 1$ levels. Confusion over this language prompted Maurice Goldman, one of the pioneers of magnetic resonance, to call such a pulse a “so-called $\pi/2$ pulse”.

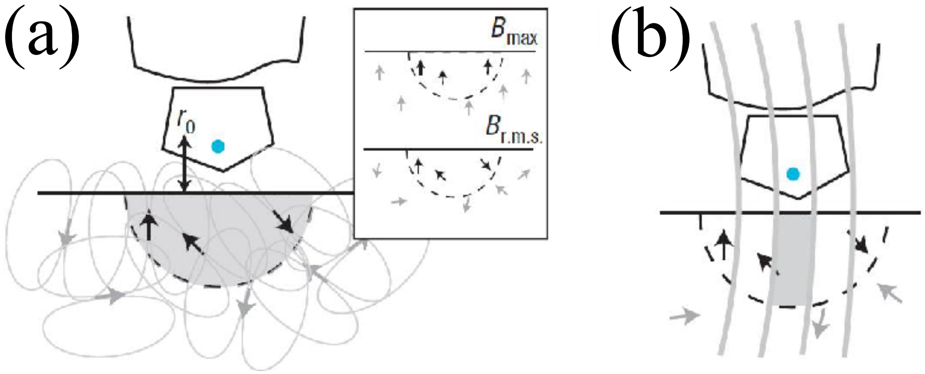

Figure 1.8: Illustration of high-spatial-resolution magnetometry with a diamond nanocrystal. (a) The dipolar fields from spins in the sample decay rapidly with distance; only those within a distance $\sim r_o$ contribute to the observable signal for the point-like NV center. The inset shows how B_{max} (the magnetic field produced by fully polarized nuclei) and B_{rms} are related; when few spins are involved, the statistical fluctuations become large. (b) In the presence of a magnetic-field gradient (field lines in grey), only the spins from a small region of the detection volume are precessing at the frequency band center of the detector, enabling even higher spatial resolution. Adapted from [13].

1.4.1 Near-field scanning probes and single-NV magnetometry

Perhaps the most conceptually simple implementation of a nanoscale magnetometer is using a near-field scanning-probe technique. A nanodiamond with a single NV center is placed at, for example, the end of an atomic-force microscope (AFM) and the resonance frequency (or for AC measurements, the spin echo amplitude) is monitored using the ODMR techniques described in Sec. 1.3. The probe is scanned laterally just above the sample of interest in order to produce a multi-dimensional map of the magnetic field produced by spins in the sample. In some situations it may also be possible to attach the sample on the probe and scan over the surface of the diamond. Such a system is called “near-field” because its spatial resolution is limited only by the distance between the NV center and the object of study, not by the diffraction limit set by the wavelength of the fluorescence light.

One of the primary goals of these near-field scanning probes is to detect the signal from a small ensemble of nuclear or electronic spins in the sample of interest. The ultimate limit would be to detect the signal from a single electronic spin [39], or perhaps eventually a single nuclear spin [41, 13]. To see how this may be possible, consider a material with a varying nuclear spin density $n_s(\vec{r})$ that is brought in close proximity (distance $\sim r_0$) to the NV center [Fig. 1.8(a)]. Even at cryogenic temperatures, the thermal nuclear spin polarization of the material is small. However, because only a few spins are involved, the distribution of spin configurations leads to an appreciable variance in the spin polarization [141], proportional to $\sqrt{N}$, where $N \approx {r_0}^3 n_s$ is the number of nuclear spins which the sensor is able to detect.

More precisely, this statistical polarization produces a substantial, albeit randomly oriented, magnetic field with projection along the NV axis of [41]:

$$B_{rms} \approx \frac{\gamma_n}{2} \left\{ \int d^3\vec{r} \frac{n_s(\vec{r})(1 - 3\cos\theta(\vec{r}))}{|\vec{r}|^6} \right\}^{1/2}, \tag{1.7}$$

where γ_n is the nuclear gyromagnetic ratio, $\theta(\vec{r})$ is the angle between $\hat{r}$ and the NV axis at location $\hat{r}$, and we have assumed the nuclei are protons (spin $I = 1/2$). In a typical organic molecule the protons are separated by about one angstrom, so $n_s \approx 10^{23}$ cm^{-3}. If the NV center could be positioned $r_0 = 20$ nm from the molecule, the magnetic signal calculated from Eq. (1.7) would be $B_{rms} \approx 100$ nT, which is equivalent to the field from ~ 300 proton magnetic moments located 20 nm from the NV center. Such a fluctuating field amplitude is theoretically detectable by a single-NV magnetometer with less than one millisecond of signal averaging (see Fig. 1.1) using an appropriate detection scheme [13, 45, 136, 137].

Further spatial resolution, potentially down to the single-spin level is possible by employing a large magnetic-field gradient, to encode spatial information spectrally, as is commonly employed in conventional MRI. Using similar techniques to those used in magnetic resonance force microscopy [59], a magnet near the surface of a substrate can produce gradient fields of order $\frac{dB}{dr} \approx 10^6$ T/m [Fig. 1.8(b)]. The narrow kHz-scale bandwidth of an AC diamond magnetometer ($\sim 1/T_2$) [15], enables it to spectrally distinguish two protons separated by a magnetic-field difference of $\Delta B \approx 0.1$ mT, corresponding to physical separation of $\frac{dB}{dr\Delta B} \approx 0.1$ nm. This implies that individual proton detection may be possible even in organic and biological molecules.

In one of the first demonstrations of the near-field approach performed at Stuttgart [14], a nanodiamond was attached to the tip of an AFM tip [shown schematically in Fig. 1.9(a)], and fluorescence was collected by confocal microscopy using light from a 532 nm laser (coming from below the substrate). A nickel micro-magnet [optical image in Fig. 1.9(b)] was placed on a clear substrate and the near-field diamond nanoscope was scanned in the two lateral dimensions. A microwave field with frequency 2.75 GHz was applied, and the NV$^-$ fluorescence was recorded. The nickel magnet produced a large field gradient such that the microwaves were only on resonance with the NV center's $m_s = 0 \leftrightarrow m_s = -1$ transition in a narrow (~ 20 nm wide) region near the magnet, producing a thin dark region in fluorescence as NV centers in this region were driven to the darker $m_s = -1$ sublevel [Fig. 1.9(c). In the same work, gradient imaging was performed where the magnet was scanned rather than the diamond, producing resonance rings ~ 4 nm wide.

At the same time, work was performed at Harvard in AC magnetometry with single NV centers both in bulk as well as in nanodiamonds. There, the principle of

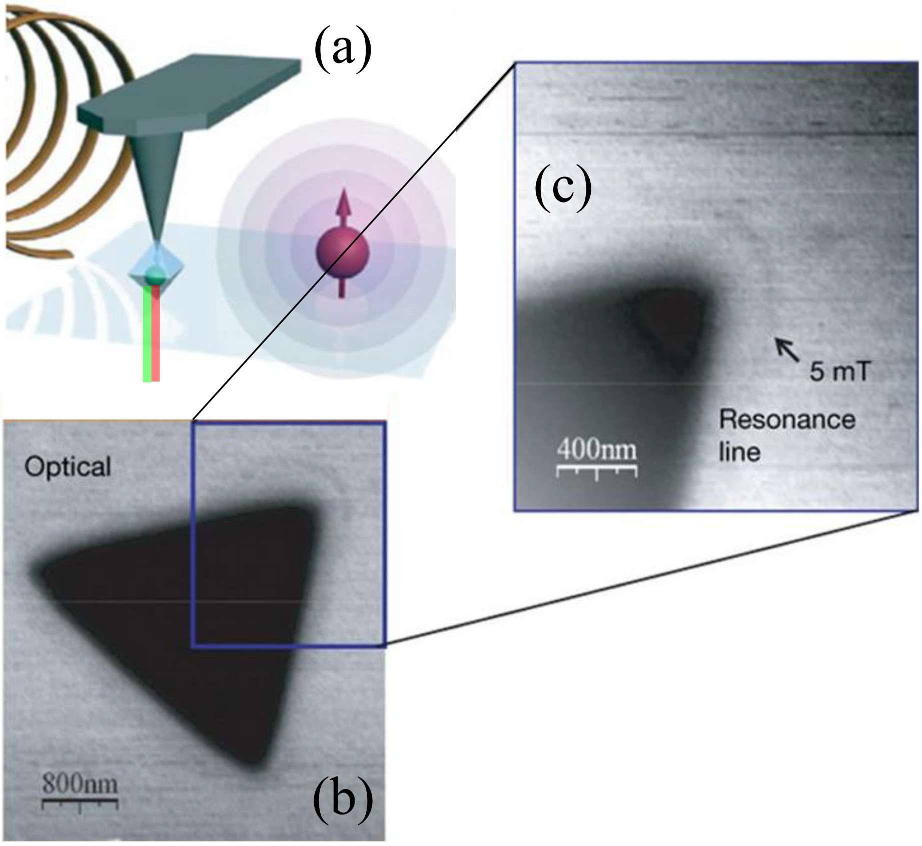

Figure 1.9: (a) Diagram of the magnetic field imaging experiment in [14]. A nanoscale magnetic particle (red) is imaged with a single nitrogen-vacancy defect (green, within the blue nanocrystal) fixed at the scanning probe tip (black). A microscope objective is used to focus light from a 532 nm laser on the NV center, exciting the $^3A_2 \rightarrow {}^3E$ transition on the phonon sideband. The same objective collects fluorescence (i.e. confocal microscopy), which is then spectrally filtered and directed to photodetectors. (b) Fluorescence map in the vicinity of the nickel magnet, recorded using a single NV center on the AFM tip as light source and magnetometer. The triangular shaped magnet is black because laser light is reflected off the magnet and consequently no fluorescence is collected in this region. Inset (c), the fluorescence signal from the scanned nitrogen-vacancy center attached to the apex of the AFM tip when resonant microwaves at 2.75 GHz are applied. The arrowed point corresponds to 5 mT resonance line with the magnetic field tilted by 45° relative to the nitrogen-vacancy axis. Adapted from [14].

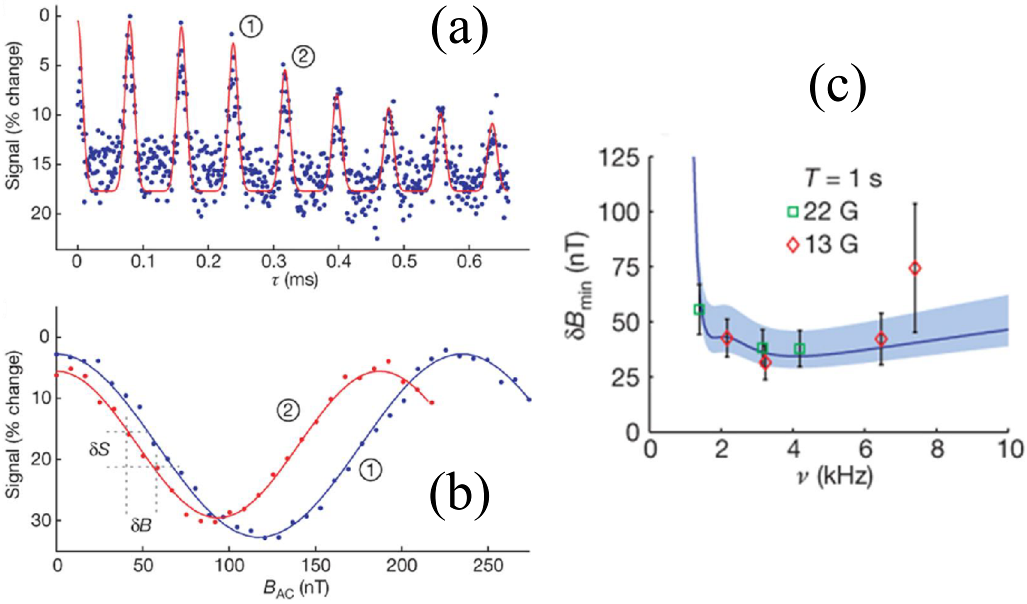

Figure 1.10: (a) Spin-echo measurement for a single NV center more than 1 μm below the diamond surface. The normalized echo signal corresponds to a fractional change in the NV center's fluorescence. Maximal signal corresponds to an average of 0.03 detected photons during the 324-ns photon counting window of a single experimental run. Collapses and revivals are due to interactions with the ^{13}C nuclear spin bath. The revivals occur at half the rate of the Larmor frequency of ^{13}C (here set by $B_{DC} = 22$ G). The spin-echo signal envelope was fitted with an exponential decay function modulated by a strongly interacting pair of nearby ^{13}C (Methods in [15]. Magnetometer sensitivity experiments are performed at spin-echo revival peaks to maximize signal. (b) Examples of measured spin-echo signal as a function of B_{AC} for two operating frequencies, 3.15 kHz (red) and 4.21 kHz (blue), corresponding to revivals 1 and 2 indicated in a. Each displayed point is a result of 7×10^5 averages of spin-echo sequences. The magnetometer is most sensitive to variations in the AC magnetic field amplitude (δB) at the point of maximum slope, with the sensitivity being limited by the uncertainty in the spin-echo signal measurement (δS). The cosine behavior of the signal with respect to AC magnetic field amplitude can be changed to a sine by adjusting the phase of the third microwave pulse by 90°. This change moves the point of maximum magnetometer sensitivity to near zero AC field amplitude. (c) Measured sensitivity of a single NV magnetometer in a bulk diamond sample over a range of frequencies for the external AC magnetic field after averaging for one second. Error bars, standard deviation (s.d.) for a sample size of 30. Also shown is the theoretically predicted sensitivity (solid blue line), with the shaded region representing uncertainty due to variations in photon collection efficiency. Measurements were carried out at two different DC fields, $B_{DC} = 13$ G (red) and 22 G (green). Adapted from [15].

AC magnetometry was demonstrated, based on spin-echo sequences (Sec. 1.3.7.2). The echo signal as a function of delay time between pump and probe pulses, τ, for a single NV center deep into a bulk crystal is shown in Fig. 1.10(a). An AC magnetic field was then applied, and the time between pumping and probing, τ, was tuned to coincide with one of the revivals in signal due to the nuclear spin bath. Figure 1.10(b) shows the echo signal as a function of AC field amplitude for two magnetic field frequencies, 3.15 and 4.21 kHz. Optimal magnetic sensitivity occurs where the echo signal has maximum slope, and this point can be chosen to coincide with zero AC field by altering the relative microwave pulse phases. Figure 1.10(c) displays the maximum magnetic sensitivity, which peaks at ~ 30 nT/$\sqrt{\text{Hz}}$, for this NV center as a function of field frequency. [10]

In subsequent work at Stuttgart [42] using isotopically pure diamond, a sensitivity of ~ 4 nT/$\sqrt{\text{Hz}}$ to AC fields and ~ 0.5 μT/$\sqrt{\text{Hz}}$ to DC fields was demonstrated for a single NV center deep in the lattice. Recently, a broadband magnetometer using a single NV center in a nanodiamond on an AFM tip was demonstrated using frequency modulation techniques combined with real-time feedback [53]. The sensitivity was only a few $\mu T/\sqrt{Hz}$, but a bandwidth from DC to ~ 0.3 MHz was shown to be possible, which is an important feature for many applications.

1.4.1.1 Sensitivity and limitations

The primary limitation in all fluorescence based magnetometers is fluorescence collection efficiency and limited signal contrast. For sufficiently low measurement contrast, R (relative difference in detected signal depending on spin-projection), the sensitivity using the fluorescence technique can be estimated [13, 12, 44] by modifying Eq. (1.1) as $\delta B_{fl} \approx \delta B_q/(R\sqrt{\eta})$, where η is the detection efficiency and δB_q is the spin-projection-noise-limited minimum magnetic field. Recent single-NV experiments [14, 15, 42] yielded typical values of $R \sim 0.2$ and $\eta \sim 0.001$, making the best possible sensitivity, in the absence of excess technical noise or other broadening mechanisms, 2-3 orders of magnitude worse than the spin-projection-noise limit. For ensembles the contrast is even worse ($R \sim 0.04$) owing to background fluorescence from centers belonging to other orientations or charge states which are out of resonance [47, 54, 44]. The contrast is limited by non-ideal branching ratios into and out of the dark singlet states [104, 19, 11, 117], while η is limited by the field of view of the detection optics and sub-unity quantum efficiency of the detected transition [142, 52].

There has been significant effort in the last few years to increase the collection efficiency by engineering nanoscale waveguides [143, 52, 144], using solid-immersion lenses made of diamond [145, 146, 147], or even coupling to metal plasmons [148, 149, 150]. While some of these techniques appear promising for future applications,

---

[10] In work with nanodiamonds, it was seen that T_2 times were only a few μs, and consequently revivals due to the nuclear bath were not observed. Nonetheless a field sensitivity of ~ 0.5 μT/$\sqrt{\text{Hz}}$ to 380 kHz AC fields was demonstrated for a ~ 30 nm nanodiamond.

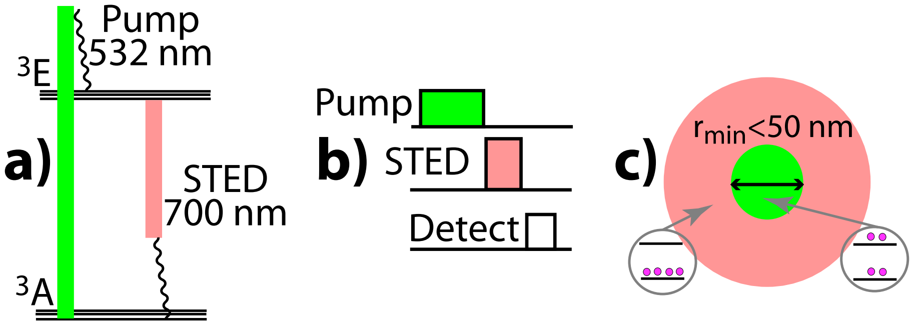

Figure 1.11: (a) Level diagram and optical transitions for the STED scheme. A green pump laser excites NV center's into the ^3E excited state and a depletion beam at 700 nm stimulates emission, quenching fluorescence. (b) Timing diagram of STED for pulsed operation. Continuous-wave operation is also possible as shown in (c). The spatial profile of the pump and STED beams during cw excitation. The level diagrams show that in the intense portion of the STED beam, all NV centers are in the ground state, whereas at the optical vortex, a significant population of NV centers exists in the excited state.

there are still several orders of magnitude room for improvement before reaching fundamental sensitivity limits.

Another challenge is to obtain long coherence times for NV centers near to the diamond surface. Currently T_2 in nanodiamonds or implanted NV centers within ~ 10 nm from the surface is just a few μs, limiting the fundamental sensitivity. As such NV centers are necessary to realize the impressive spatial resolution promised in Fig. 1.1, a major effort to understand the effect of surface charges and related defects on the NV spin is necessary.

1.4.2 Far-field sub-wavelength probes

1.4.2.1 RESOLFT and STED techniques

In order to achieve nanoscale resolution without the technical challenge of controlling a near-field probe, techniques are needed to bypass the diffraction limit of the excitation light (~ 300 nm). The most straightforward and mature technology for such sub-wavelength imaging is the STimulated Emission Depletion (STED) technique, where recent nanoscopy measurements in bulk diamond have achieved a spatial resolution of better than 6 nm [151]. The STED technique, which belongs to a family of sub-wavelength techniques based on Reversible Saturable Optical Fluorescence Transitions (RESOLFT), uses an intense, shaped laser beam to deplete the excited state via stimulated emission. Provided that this "STED" beam has greater intensity than the saturation threshold, no fluorescence is observed.

Figure 1.11(a) illustrates the necessary optical transitions schematically for an ensemble of NV centers. Figure 1.11(b) displays the timing diagram for pulsed operation. A short ($\lesssim$ 10 ns) pulse of 532 nm pump light excites NV centers into the ^3E excited state. The spatial mode of a second pulse of light tuned somewhere within the phonon-sideband (here at 700 nm) is shaped by a helical phase plate such that there is a dark region in the center of the beam due to the induced optical vortex. Due to the donut-shaped intensity profile of this laser beam, NV centers falling outside of the optical vortex immediately return to the ground state without emitting fluorescence due to depletion via stimulated emission–hence the name STED beam. NV centers in the center of the vortex, however, are relatively unaffected by the STED beam and still fluoresce. As the dark region at the middle of the optical vortex is significantly smaller than the wavelength of the light (limited by the intensity of the STED beam), sub-wavelength spatial resolution in the lateral dimensions is realized [11]. The same effect can be achieved using cw light, and is illustrated in Fig. 1.11(c).

In the case of diamond nanoscopy with an ensemble of NV centers, the lateral resolution of STED, r_{min}, can be related to the power of the STED laser light, I_{STED}, and the saturation power of the ensemble, I_{sat}, by [151]:

$$r_{min} \approx \frac{\lambda}{2NA}\frac{1}{\sqrt{1+I_{STED}/I_{sat}}}, \tag{1.8}$$

where $\lambda = 532$nm is the excitation wavelength, and $NA \approx 1$ is the numerical aperture of the microscope objective. A STED beam intensity of $I_{STED} \approx 100\text{MW/cm}^2$ at the focal point, which is well below the damage threshold of the crystal [151], is routinely realized using a high-NA objective to focus a 100-mW laser beam down to a sub-micron spot. The saturation intensity near the peak of the phonon sideband is $I_{sat} \approx \frac{hc}{\lambda\sigma\tau_{ES}} \approx 300\ \text{kW/cm}^2$, where h is Planck's constant, c is the speed of light, $\sigma \approx 10^{-16}\ \text{cm}^2$ is the excitation cross section [151], and $\tau_{ES} \approx 12$ ns is the excited-state lifetime [153]. Inserting these values into Eq. 1.8, the fundamental limit on lateral resolution is $r_{min} \approx 5$ nm.

For biological applications it is often necessary to use much lower light intensities to avoid damaging the sample under study. In some cases, this can be accomplished by transferring centers into a metastable dark state instead of the ground state [142, 49]. This dark state eventually decays to a bright state, but at a much slower rate than typical radiative decay. In this case the equations for resolution enhancement are identical, except τ_{ES} is replaced by the time the NV centers remain in the dark state. In a recent demonstration of a technique called "spin-RESOLFT", the effective dark-state lifetime was limited only by $T_1 \sim 10$ ms [49]. There a spatial resolution of 38 nm nm was achieved using microsecond pulses of light [peak power 2 mW (3 MW/cm^2)], and sub-wavelength magnetometry was demonstrated. Another promising technique

---

[11] Depth resolution of $\lesssim$ 20 nm is also possible by using a thin layer of NV centers or by longitudinal shaping of the STED beam [152].

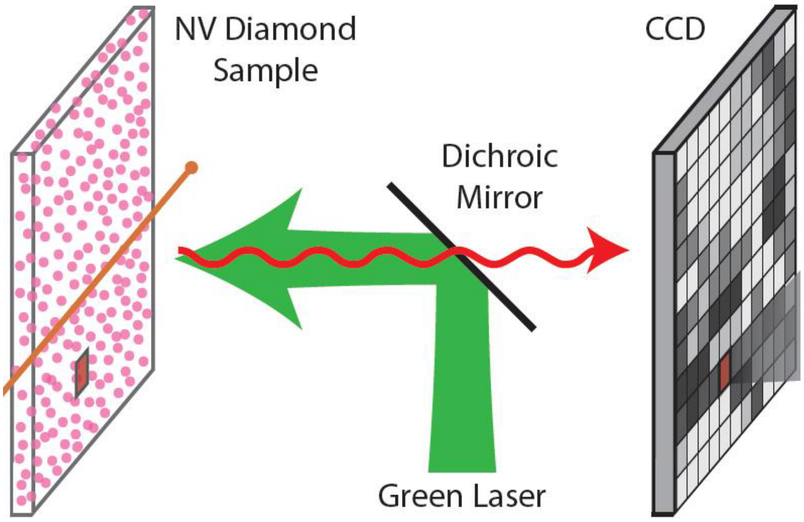

Figure 1.12: Wide-field fluorescence microscope used for magnetic imaging as described in text. The sample under study would be placed in close contact with the thin layer of NV centers. Adapted from [13].

is to drive NV centers into a different trapped state (lifetime >> 1 s for ultrapure CVD diamond) using red excitation. Using this scheme researchers have achieved 12 nm spatial resolution with 16 mW (12 MW/cm^2) of light. The exact nature of this trapped state requires further investigation, but it results in [154] are consistent with it being the NV^0 charge states.

1.4.3 Wide-field array magnetometers

One of the features, which makes magnetic sensing with diamond NV centers most promising is the possibility for variable spatial resolution combined with broad measurement bandwidth. So far we have considered single NV magnetometers which offer the best spatial resolution, but ensembles of NV centers can be used to make magnetic field images of much wider fields of view with even greater sensitivity.

Figure 1.12 depicts a technique using a wide-field fluorescence microscope to acquire such an image. A green pump laser beam is focused onto a diamond sample with a thin layer of NV centers. The thickness of the layer is chosen to be roughly the desired spatial resolution (typically a few hundred nanometers to a micron). The focal point is either a few Rayleigh ranges before (to produce a negative image) or after (positive image) the layer of NV centers and the illuminated region of the NV layer defines the field of view (typically order ~ 100 μm). The fluorescence is collected from the same objective, spectrally filtered and directed to a charge-coupled device (CCD) for post processing. This proof of principle of this scheme was recently demonstrated [54]. There a field of view of $\sim 60\ \mu$m was realized with a spatial resolution of $\sim 500\ \mu$m, using a high-numerical aperture oil-immersion objective.

1.4.4 Bulk micro-magnetometers

As discussed in Sec. 1.4.1.1, the sensitivity of fluorescence-based diamond magnetometers is limited due to poor light collection efficiency and diminished measurement contrast. For larger, micro-scale devices, one avenue around this problem may be to use optical rotation [91] or absorption of a probe beam for spin-state detection, is that transmitted light can be easily collected. Unfortunately, the weak spin-orbit coupling in the excited state and the presence of strain in the crystal, make the spin-nonconserving transitions necessary for optical rotation negligible, at least for large ensembles at room temperature. However, recently, a technique was demonstrated using infrared (IR) absorption on the $^1A_1 \leftrightarrow {}^1E$ transition [44] which circumvents some of the photon shot-noise problems associated with other techniques. This work is covered extensively in Chapter 5.

1.5 Outline of remaining chapters

The remainder of this dissertation is separated into four chapters. In the Chapter 2, the basic design principles for fabricating diamond optimized for high-spin-density magnetometry are discussed. In the Chapters 3 and 4, the underlying physical properties of the NV center are discussed and novel techniques for maximizing magnetometer performance based on this basic physics are presented. Finally, in Chapter 5 we discuss implementation of these techniques in an ensemble magnetometer which is the current state-of-the-art in terms of sensitivity and bandwidth.

Chapter 2

Diamonds with a high density of nitrogen-vacancy centers for magnetometry applications

This chapter was previously published in Ref. [12] and is republished here, with minor changes, with permission.

2.1 Abstract

Nitrogen-vacancy (NV) centers in millimeter-scale diamond samples were produced by irradiation and subsequent annealing under varied conditions. The optical and spin relaxation properties of these samples were characterized using confocal microscopy, visible and infrared absorption, and optically detected magnetic resonance. The sample with the highest NV$^-$ concentration, approximately 16 ppm (2.8×10^{18} cm^{-3}), was prepared with no observable traces of neutrally-charged vacancy defects. The effective transverse spin-relaxation time for this sample was $T_2^* = 118(48)$ ns, predominately limited by residual paramagnetic nitrogen which was determined to have a concentration of 49(7) ppm. Under ideal conditions, the shot-noise limited sensitivity is projected to be $\sim$ 150 fT/$\sqrt{\text{Hz}}$ for a 100 μm-scale magnetometer based on this sample. Other samples with NV$^-$ concentrations from .007 to 12 ppm and effective relaxation times ranging from 27 to over 291 ns were prepared and characterized.

2.2 Introduction

Optical magnetometers based on alkali vapor cells can measure magnetic fields with exceptional sensitivity and without cryogenics; however spin-altering collisions limit the sensitivity of small sensors [7]. Paramagnetic impurities in diamond, on the other hand, are a promising system for millimeter- and micrometer-scale magnetometers, because they exhibit long spin coherence times (several ms [42]) over temperatures ranging from liquid helium to well above room temperature. Nitrogen-vacancy (NV) centers are particularly promising because they have a spin-triplet ground state and convenient optical transitions, allowing for efficient optical pumping and magnetic sensitivity. Recently, single NV-centers were used for nanometer-scale magnetometry [15, 14] and magnetometry based on high-density ensembles of NV^- centers was proposed [13]. Here we discuss preparation of diamond samples with parameters optimized for room-temperature, optical NV-ensemble magnetometers.

The parameters for sample preparation most relevant to magnetometry are the concentration and homogeneity of the NV^- centers, as well as the abundance of other impurities such as neutral nitrogen-vacancy centers (NV^0) and substitutional nitrogen in the lattice. There is a wealth of techniques for growth, irradiation, and annealing of diamonds that can be considered (see, for example, Refs. [155, 156, 157, 158] and references therein). In this work, we prepared ten samples under different conditions and observed the optical properties at each stage of development using confocal microscopy, visible and infrared absorption, and optically detected magnetic resonance (ODMR). The results form an initial matrix that will help identify the most important variables and pinpoint optimal ranges in the sample preparation process.

2.3 Experimental Procedure

2.3.1 Sample parameters and irradiation

#	Company	Synthesis	[N] (ppm)	Ion	Dose (cm^{-2})	Anneal Temp.(°C)
1	Sumitomo	HPHT	$\lesssim 100$	e^-	4.0×10^{18}	[700,875,1050]
2	Sumitomo	HPHT	$\lesssim 100$	e^-	9.8×10^{18}	"
3	Element-6	CVD	$\lesssim 1$	e^-	4.0×10^{17}	"
4	Element-6	CVD	$\lesssim 1$	e^-	8.0×10^{16}	"
5	Element-6	HPHT	$\lesssim 200$	e^-	8.2×10^{18}	"
6	Element-6	HPHT	$\lesssim 200$	e^-	9.8×10^{18}	"
7	Sumitomo	HPHT	$\lesssim 100$	e^-	9.8×10^{18}	"
8	Element-6	HPHT	$\lesssim 100$	e^-	4.0×10^{17}	"
9	Element-6	HPHT	$\lesssim 100$	H^+	1.0×10^{16}	[500,875,1050]
10	Element-6	HPHT	$\lesssim 100$	H^+	1.0×10^{16}	[800,875,1050]

Table 2.1: Sample characteristics. Initial nitrogen concentration, [N], is given as specified by manufacturer. Each annealing was carried out for $2 - 2.5$ hours.

Ten diamonds were fabricated commercially by Sumitomo and Element-6 using either chemical-vapor deposition (CVD) or high-pressure, high-temperature (HPHT) synthesis. The samples are millimeter-sized diamond crystals with an initial concentration of nitrogen impurities ranging from less than 1 ppm to 200 ppm (1 ppm corrsponds to 1.76×10^{17} cm^{-3} in diamond). In the case of the HPHT samples, growth sectors with high and low nitrogen concentrations were identified and three of these sectors in Sample 5 were studied separately (see Sec. 2.4.4). The crystals were subjected to either proton or electron irradiation at varying doses. Electron irradiation was done at Argonne National Laboratory using 3.0-MeV electrons (e^-) from a Van de Graaff generator. Thermal contact with a water-cooled copper target was used to keep the temperature of the samples below 150°C during the irradiation process in order to reduce vacancy-carbon recombinations [159]. The irradiation doses were chosen so that the resulting vacancy concentrations would be within two orders of magnitude of the initial nitrogen concentration, as discussed in Sec. 2.4.2.3. The proton irradiation was performed at the Conditions Extrêmes et Matériaux: Haute Température et Irradiation (CEMHTI) laboratory using 2.4-MeV protons (H^+), and the samples were maintained below 80°C during irradiation. Table 2.1 shows the specific conditions under which each sample was prepared.

2.3.2 Optical characterization and annealing

After the irradiation, optical characterization of each electron-irradiated sample was performed using confocal-microscopy at room temperature [105]. Light from a commercial solid-state 532-nm laser was spatially filtered using a single-mode fiber, collimated, spectrally filtered, and combined into the collection path by a dichroic beamsplitter, exciting an optical transition associated with the NV^- center's ^3E excited-state manifold [104]. The excitation beam was focused to a sub-micron spot using a 0.6-numerical-aperture microscope objective with 40x magnification. The resulting photoluminescence (PL) was collected through the same objective, spectrally filtered to remove reflected laser light, imaged onto a pinhole, and analyzed. For spatial imaging, the microscope objective was mounted on a closed-loop triple-axis piezoelectric translation stage, and the collected photoluminescence was detected using a silicon avalanche photodiode, with filters used to select the NV^- phonon sidebands (PSB) in the spectral range $\sim$ 647-804 nm. For spectroscopy, the collected photoluminescence was sent to a spectrometer incorporating a cooled CCD detector, where the spectrum was recorded for various locations throughout each sample. The NV^0 and NV^- zero-phonon lines (ZPL) were fit to Gaussian lineshapes after subtracting the local linear background. Imaging tests on single NV centers in an Electronic Grade ultra-pure CVD diamond purchased from Element-Six indicated an effective measurement volume of 5.2 $\mu\mathrm{m}^3$, and the single-center fluorescence spectrum provided the absolute scale for determining the NV^- concentrations in the higher NV^- density samples.

Following irradiation and after the initial round of PL measurements, the eight electron-irradiated samples were subjected to thermal annealing at 700°C in the presence of a forming gas (0.96 atm Ar, 0.04 atm H_2), in order to prevent surface oxidation, for $2-2.5$ hours. The two proton-irradiated samples were annealed for two hours in vacuum, one sample at a temperature of 800°C (Sample 10) and the other at 500°C (Sample 9). Afterwards, each sample was analyzed with confocal spectroscopy at room temperature. This process was repeated for nine of the samples at an annealing temperature of 875°C and then 1050°C in the presence of the same forming gas. After the final annealing, a Varian Cary 50 UV-VIS spectrometer and Nicolet Magna IR-750 Fourier-transform infrared (FTIR) spectrometer were used to measure visible and infrared absorption spectra for some of the electron-irradiated samples. Additionally, confocal microscopy was used for ODMR measurements and the effective transverse spin-relaxation times were determined.

2.4 Results

2.4.1 Proton-irradiated samples

Development of micro-magnetometers in certain geometries may benefit from the use of proton irradiation, where damage is confined to a smaller volume than with electron irradiation. In this section we present results of the optical characterization of two identical proton-irradiated samples (Samples 9 and 10).

2.4.1.1 Stopping Range of Ions in Matter (SRIM) and spectroscopic measurements

When charged particles traversing a medium come near to rest, the stopping power dramatically increases, causing a thin layer of radiation damage to develop. This effect is pronounced for non-relativistic ions in diamond. The ionization losses limit penetration to a thin layer near the surface, where radiation-induced vacancies in the carbon lattice are formed. In contrast, relativistic electrons make it through the $0.5-1$ mm thick samples, and, consequently, the vacancies are distributed relatively evenly.

Figure 2.1(a) shows the results of proton-irradiation Monte-Carlo simulations made using the Stopping and Range of Ions in Matter (SRIM) software [160]. The diamond sample was modeled as a pure ^{12}C layer with density 3.52 g/cm^3 and displacement energy 45 eV [161, 162, 163]. For the H^+ energy of 2.4 MeV, the simulations predict a dense layer of vacancies, recoiled interstitial carbon atoms, and stopped H^+ ions at a depth of $\sim 35\ \mu$m, and almost no radiation damage deeper into the sample. If vacancy-to-NV conversion is relatively even throughout the sample, then one might expect a similar depth profile of NV concentration.

Figure 2.1(b) shows the estimated NV^- concentration, taken by normalizing the integrated ZPL intensity by that of a single NV center, as a function of depth for the proton-irradiated samples after the first annealing. Figure 2.1(c) displays the

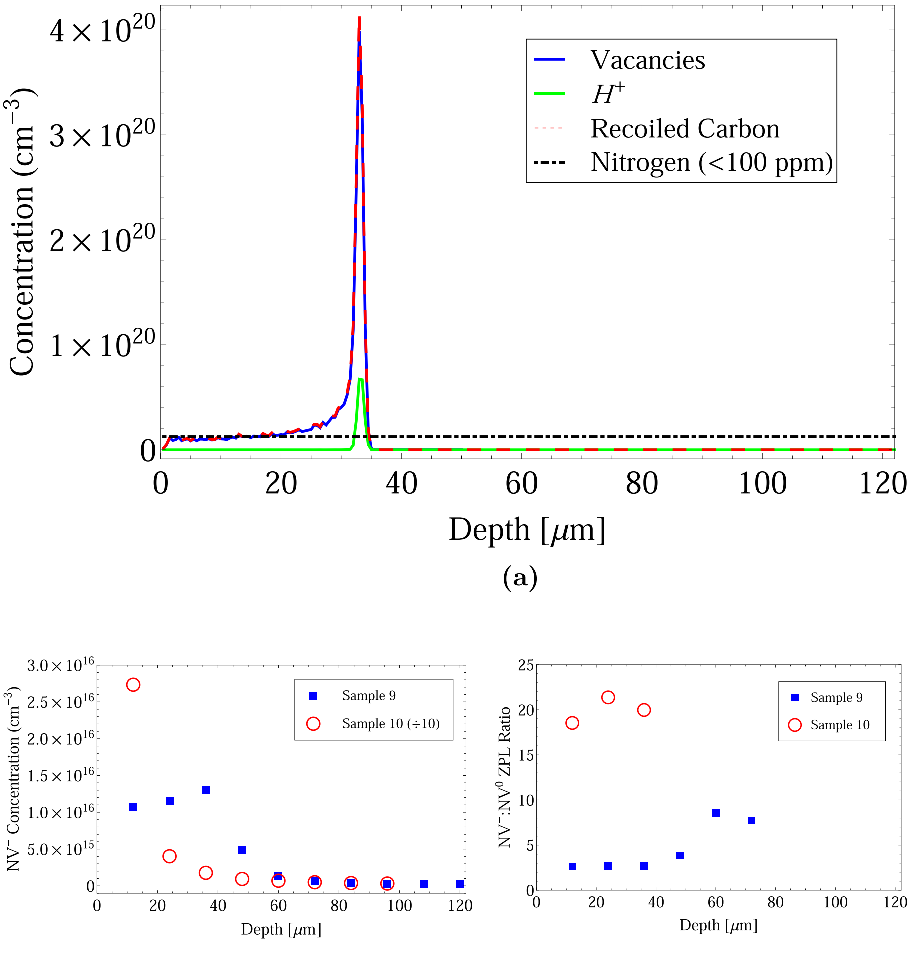

(a)

(b) **(c)**

Figure 2.1: (a) Monte-carlo simulation of radiation damage as a function of penetration depth for 2.4-MeV proton radiation, using the SRIM software. (b) Depth profile of NV$^-$ centers, taken by normalizing the integrated ZPL intensity by that of a single NV center, after the first annealing (see text). The concentrations for Sample 10 have been divided by a factor of 10 for visualization. Errors on the concentration estimates are discussed in Sec. 2.4.2.2. (c) NV$^-$:NV^0 ZPL intensity ratio as a function of depth after the first annealing. The lightpower was 100 μW. For Sample 10, beyond a depth of ~ 36 μm, the NV^0 ZPL became indistinguishable from the background.

NV^-:NV^0 ZPL intensity ratio under the same conditions as Fig. 2.1(b) and is discussed later in Sec. 2.4.1.3. In Fig. 2.1(b), Sample 9 (after annealing at 500°C) shows a thin layer of NV^- emission with a small peak at ~ 35 μm, followed by a rapid decrease in concentration with depth. The peak intensity, however, is not nearly as dramatic as in the vacancy profile predicted by SRIM. Sample 10 (after the first annealing at 800°C) shows a sharp, monotonic decrease throughout the first 35 μm that is not at all consistent with the vacancy profile predicted by SRIM. Upon further measurements (see Fig. 2.2(a) in Sec. 2.4.1.2), it was seen that the qualitative features in the depth profiles of Sample 10 varied greatly for different locations. It is worth mentioning that in this sample the NV^- concentration varied by more than an order of magnitude for different locations all at a depth of ~ 12 μm from the surface. There was one location that had a concentration nearly three orders of magnitude lower than the mean. As shown in the next section, these spatial inhomogeneities in NV^- concentration are related to the presence of multiple growth sectors, with widely varying nitrogen concentrations, in these HPHT-synthesized diamonds.

2.4.1.2 Photoluminescence depth profiles

The spectroscopic measurements were followed by spatially resolved PL measurements where the position of the focus was varied by translating the microscope objective with a closed-loop, triple-axis piezoelectric stage and the fluorescence, in the 647-804 nm range, was collected. Figure 2.2(a) shows examples of raw data both for a typical scan (left side) and one around a sector boundary (right). After averaging over the lateral dimension, x, the resulting depth profile was deconvolved using a similarly-processed profile from a sample containing a very thin layer ($\lesssim 200$ nm) of NV centers as the response function, in conjunction with an optimized Wiener filter [164]. Figure 2.2(b) shows the results for three different samples: both of the proton-irradiated samples as well as Sample 1, a high nitrogen-content electron-irradiated sample, for comparison. These profiles were taken after the final annealing at 1050°C and were post-selected to ensure that they were from a single growth-sector. As expected for relativistic-electron irradiation, Sample 1 has a relatively even depth profile throughout the sample. The gradual decrease in intensity with depth is consistent with absorption of the 532 nm laser light, as seen in Sec. 2.4.2.4. Samples 9 and 10, on the other hand, exhibit emission only from a thin layer of NV^- centers near the surface. The edge of this layer is at approximately the same depth as the edge in the vacancy profile predicted by SRIM, ~ 35 μm from the surface, but the sharp peak at the end of the layer is absent. Figure 2.2(c) shows the depth profile in a single-sector region for Sample 9 after both the first and final annealing; the results are discussed below.

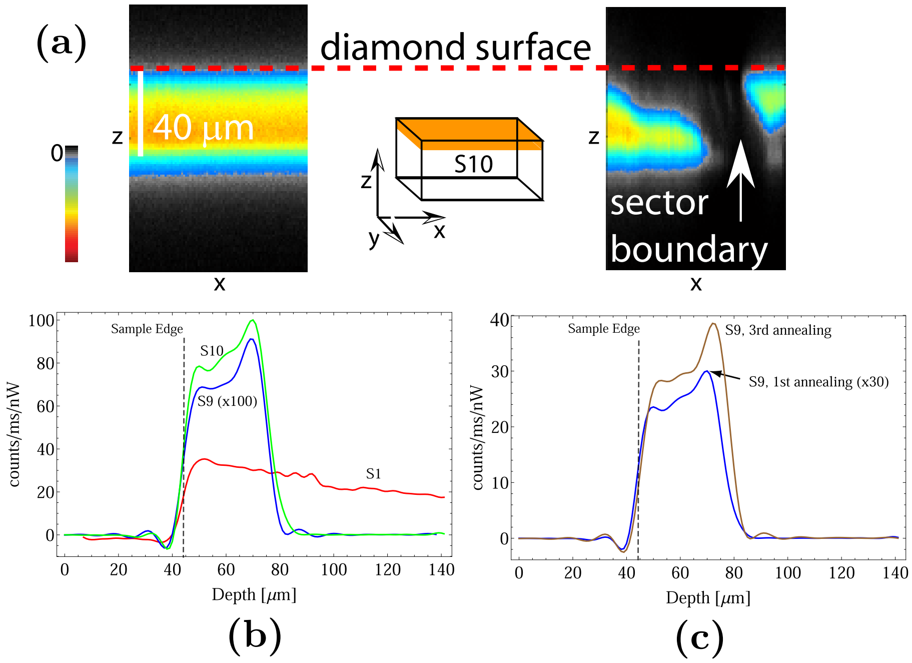

Figure 2.2: (a) Depth profiles of the phonon-sideband PL intensity for Sample 10 at a typical location (left) and at a sector boundary (right). (b) Deconvolved intensity as a function of depth for Samples 1, 9, and 10 (S1, S2, etc.) after the first annealing at 700, 500, and 800 °C, respectively. The PL intensity is normalized by the incident laser power (5, 153, and 1.9 nW for Samples 1, 9, and 10, respectively). The signal for Sample 9 is multiplied by a factor of 100 for visualization. (c) PL deconvolution for Sample 9 after the first and third annealing. The PL intensity after the first annealing has been multiplied by a factor of 30. The damped oscillations are artifacts of the signal processing caused by rapid changes in concentration.

2.4.1.3 Discussion of fluorescence depth profiles

There could be several potential explanations for the deviation of the observed NV$^-$ fluorescence depth profiles from the vacancy distribution predicted by SRIM:

1. The ZPL intensity and the integrated PSB fluorescence are poor indicators of the actual NV$^-$ concentration.
2. The vacancies diffuse tens of μm during annealing.
3. The concentration of nitrogen is insufficient to convert most of the vacancies to NV$^-$ centers at the stopping peak.
4. Other products of the irradiation, either the interstitial carbon, stopped H$^+$ ions, or the vacancies themselves, inhibit NV$^-$ formation by forming stable defects with the vacancies.

We now briefly discuss each of these possibilities and show that the first three explanations are not supported by our observations.

1. In the He$^+$ ion implantation work of Ref. [158], a similar deviation from the SRIM vacancy profiles was seen in the NV$^-$ ZPL intensities for various radiation doses. The primary cause posited in that work was radiation absorption by vacancies and graphitization defects. In order to set a limit on the absorption by such defects in our samples, we monitored the intensity of the diamond's first-order Raman peak at 573 nm during the spectroscopic measurements whenever it was distinguishable from the background. In every instance, the 573 nm peak intensity did not change by more than a factor of two over the first $\sim$ 100 μm of the sample, and at least some of this attenuation was due to absorption by the NV$^-$ centers themselves (see Sec. 2.4.2.4). To our knowledge, there is no defect present in large concentrations in these samples that absorbs strongly in the NV$^-$ fluorescence region but not at 573 nm. The neutral vacancy center, GR1, for example, absorbs roughly equally in these two spectral regions [165, 166]. Therefore a factor of approximately two is the maximum possible attenuation of the NV$^-$ fluorescence due to absorption by other defects. The 35-μm peak height predicted by the SRIM vacancy depth profile is several orders of magnitude larger than the peak heights of the NV$^-$ depth profiles in Figs. 2.1(b) and 2.2(b), so radiation absorption cannot explain this deviation.

2. The results shown in Fig. 2.2(c) give evidence that vacancy diffusion cannot explain the deviation from the SRIM vacancy depth profile. The magnitude of NV$^-$ fluorescence in the depth profile for Sample 9 exhibits an increase of approximately a factor of 35 between measurements taken after the first and third annealing, signifying that vacancies are diffusing to form NV$^-$ centers during the second and/or third annealing. However, based on the shape of these depth profiles, and taking into account the artifacts introduced by the deconvolution, a limit of $\delta r \lesssim 1.5$ μm can be placed on the spatial range of diffusion of vacancies in this sample during annealing

at 875°C and 1050°C for a time of $t = 2$ hours each. This is not enough diffusion to account for the large difference in peak height predicted by the SRIM vacancy depth profile. Assuming the diffusion coefficient at 875°C is smaller than that at 1050° and that the vacancies are not annihilated by other processes during annealing, this corresponds to an upper bound on the diffusion coefficient at 1050°C of $D_V \approx (\delta r)^2/(4t) \lesssim 4 \times 10^{-13}$ cm^2/s.

3. To address the possibility that insufficient nitrogen levels limit the overall NV$^-$ concentration at the stopping peak, a rough measurement of the levels of substitutional nitrogen available for NV formation was made by monitoring the ZPL of the neutral NV^0 center at 575 nm. Substitutional nitrogen is a donor in diamond, believed to be responsible for the negative charge on the NV$^-$ center, and consequently a shortage of nitrogen leads to a greater proportion of neutral NV^0 centers [167, 158, 168]. Figure 2.1(c) shows the NV$^-$:NV^0 ZPL intensity ratio for Samples 9 and 10 for the same depths as in Fig. 2.1(b). The high ratio for Sample 10 is inconsistent with donor depletion. The ratio for Sample 9 is lower compared to that of similar samples irradiated at lower doses (NV$^-$: NV^0 $\approx 1 - 40$ (see Fig. 2.4(b)), but the absence of a sharp dip near 35 μm suggests that electron depletion cannot account for the deviation from the SRIM vacancy depth profile.

4. The possibility that other radiation damage inhibits NV formation cannot be verified in this study, but it is not inconsistent with our observations. As seen in Figure 2.1(a), the recoiled carbon atoms are the most abundant defect present in the diamond, with more than 30 times the nitrogen concentration. The deposited H$^+$ also comprise over five times the nitrogen concentration. At these levels, it is more likely that during annealing the diffusing vacancies will recombine, or form other color centers, with these interstitial atoms before they encounter a nitrogen atom. ESR measurements of the interstitial carbon color center, R2, suggest that some recombination occurs during irradiation unless the diamond is cooled well below room temperature [169, 159] (not the case here), and that during annealing the remaining R2 centers become mobile at a threshold temperature in the $400 - 700$°C range [169, 166, 159]. Samples 9 and 10 are actually two halves of the same diamond, but their first annealing was done at different temperatures: 500°C and 800°C, respectively. The temperature of these samples was maintained below 80°C during irradiation, yet their depth profiles after these different annealing temperatures show similar deviation from SRIM vacancy profiles. This suggests that, if interstitial recombination is the mechanism responsible for this deviation, the onset of self-interstitial mobility occurs at or below an annealing temperature of 500°C. This limit still falls within the $400 - 700$°C range of values for the onset of self-interstitial mobility found in the literature.

In addition to recombination with interstitial carbon atoms, vacancies are also known to combine with hydrogen atoms to form VH$^-$ [170] and NVH$^-$ [171] defects. As we were not setup to observe ESR where these paramagnetic centers are best detected, they were not studied here, but they may limit NV formation and dephase NV$^-$ spins in magnetometry applications.

In summary, the proton-irradiation and annealing produced NV centers in a confined volume of depth ~ 35 μm. The depth profiles of the NV$^-$ center concentrations showed a significant deviation from the expected damage profiles. We considered possible causes of such a deviation and surmised that excess radiation damage likely inhibited NV formation. The resulting [NV$^-$] distributions may actually be better for some micro-magnetometer configurations, but more work is required to understand the details of the radiation damage.

2.4.2 Electron-irradiated samples

In contrast to proton irradiation, irradiation with electrons leaves a relatively even distribution of damage throughout the sample, enabling the preparation of millimeter-sized samples for ultra-sensitive magnetometry. Here we present and discuss the optical and magnetic-resonance characterization of electron-irradiated samples (Samples 1-8) prepared under varied conditions.

2.4.2.1 Fluorescence spectra and calibrations

Figure 2.3(a) shows the room-temperature 532-nm laser-induced fluorescence spectrum for Sample 2, a $2 \times 2 \times 1$ mm^3 Sumitomo HPHT sample irradiated with electrons at a dose of 9.8×10^{18} cm^{-2} (see Table 2.1), for each stage of annealing, as well as the spectrum for a single NV in a non-irradiated Electronic Grade ultra-pure CVD diamond. The collection volume was located near the surface of the sample in order to minimize the effects of laser and fluorescence absorption. Before annealing, the main spectral feature is a sharp peak at 573 nm which is the first-order Raman peak of the pure diamond lattice. Additionally, the broad second-order Raman feature is visible for the single-NV center in the $600-625$ nm region. After annealing, the much brighter NV^0 and NV$^-$ zero-phonon lines, at 575 nm and 638 nm, respectively, with linewidths of approximately 1.5 nm full width at half maximum, become prominent features in the spectrum. The monotonically increasing background is due to the overlapping broad phonon sidebands. For more details on the spectral features, see, for example, Ref. [16].

In order to quantify the NV concentrations, the fluorescence collection volume was determined by taking several lateral scans of the ultra-pure CVD diamond at different depths and recording the $647-804$ nm fluorescence of single NVs, as illustrated in Fig. 2.3(b). A collection volume of ~ 5.2 μm^3 was calculated from these scans. This value, together with the integrated ZPL intensity at 638 nm from the spectrum of one of the single NV centers (Fig. 2.3(a)), were used to determine the NV concentrations throughout this work. We note that concentrations obtained in this way are expected to be a lower bound, as the laser power used for these single NV scans was just above saturation, and the effects of PL quenching due to non-radiative energy transfer to nearby impurities [172] were not quantified. Nonetheless, as will

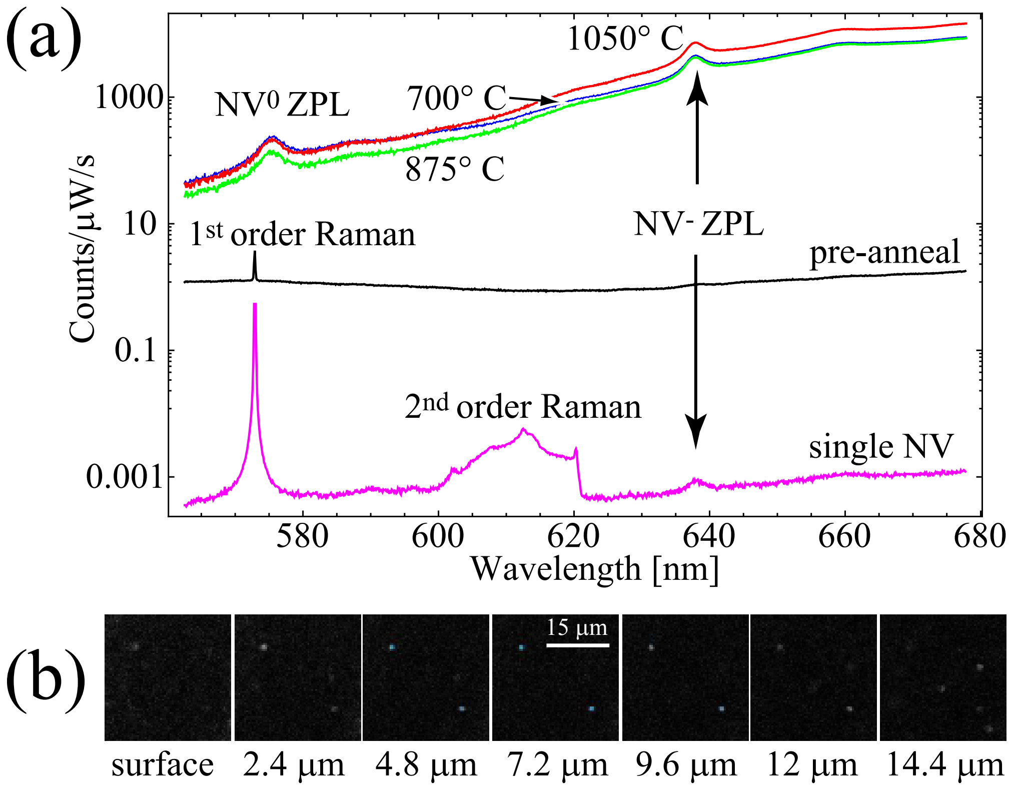

Figure 2.3: Fluorescence spectrum at each stage of annealing for Sample 2 (see Tab. 2.1), as well as the spectrum of a single NV center in the ultra-pure CVD diamond used for calibrations. The measurement volume is approximately 5.2 $\mu\mathrm{m}^3$ located ~ 12 μm from the surface. The important spectral features are labeled (as described in the text). (b) Lateral (xy) scans of the ultra-pure CVD diamond showing fluorescence in the $647-804$ nm spectral region from two of the single NV centers used to determine the fluorescence collection volume. The range for all of the scans is 30 μm $\times$ 30 μm
.

be shown in Sec. 2.4.2.4 and 2.4.2.5, this method produced concentrations values that are in close agreement with absorption-based methods [173, 131]. Furthermore, a fluorescence-based approach enables the measurement of NV concentrations in optically thin samples.

2.4.2.2 NV concentrations

Figure 2.4(a) shows the NV^- concentration for all of the electron-irradiated samples after each stage of annealing. All concentrations were determined by normalizing the integrated ZPL intensity by that of a single NV center, and the collection volume was $\sim 12\ \mu$m from the surface. For the samples with high nitrogen content, the NV^- concentration was already near, or at, its maximum value after the first annealing at 700 °C. The samples with $\lesssim 1$ ppm nitrogen did not reach a maximum until the 875 °C annealing. We note that since we do not completely distinguish between the effects of annealing time and temperature, it is possible that annealing the low nitrogen-content samples at 700°C for twice as long would produce the same effect.

In order to test reproducibility, the data were taken on two different days, using different lateral locations in the sample, and in between days the mirrors and sample mount had been adjusted. The samples were analyzed after the 700°C (but before the 875°C) annealing on both days. The discontinuity seen in Fig. 2.4(a) between days shows that the uncertainty in determination of the NV^- concentrations is about a factor of two, caused by the aforementioned conditions. We estimate that the total systematic uncertainty due to radiation absorption, uncertainty in the collection volume, etc. is less than the spread in concentration due to spatial inhomogeneity.

The NV^-:NV^0 ZPL intensity ratio is plotted as a function of annealing temperature in Fig. 2.4(b). The ZPL intensity ratio can be converted to a concentration ratio by using the difference in the Huang-Rhys factors (Sec. 2.4.3) for the two charge states (NV^-:NV^0 ZPL intensity ratio is approximately a factor of two smaller than the corresponding concentration ratio). The ratio does not appear to have a strong temperature dependence, but it varies strongly as a function of position in the sample and/or laser power, as evidenced by the large discontinuity between the two different days (corresponding to two different locations and laser powers). The incident laser powers are shown in the legend of Fig. 2.4(b) because, as will be discussed in Sec. 2.4.3, changes in power lead to varying degrees of photo-ionization, which, depending on the individual sample characteristics, affects the ratio by an order of magnitude or more.

The very high NV^-:NV^0 ratio for Samples 1 and 2 provides evidence that many of the nitrogen atoms had not been converted to NV centers, since if this were the case, there would not be enough donors for making the negative charge state (Sec. 2.4.1.3). Conversely, the data in Fig. 2.4(b) show the effects of electron depletion on the low nitrogen-content samples, leading to a significantly lower NV^-:NV^0 ratio. Since the specific collection location and laser power between days were different,

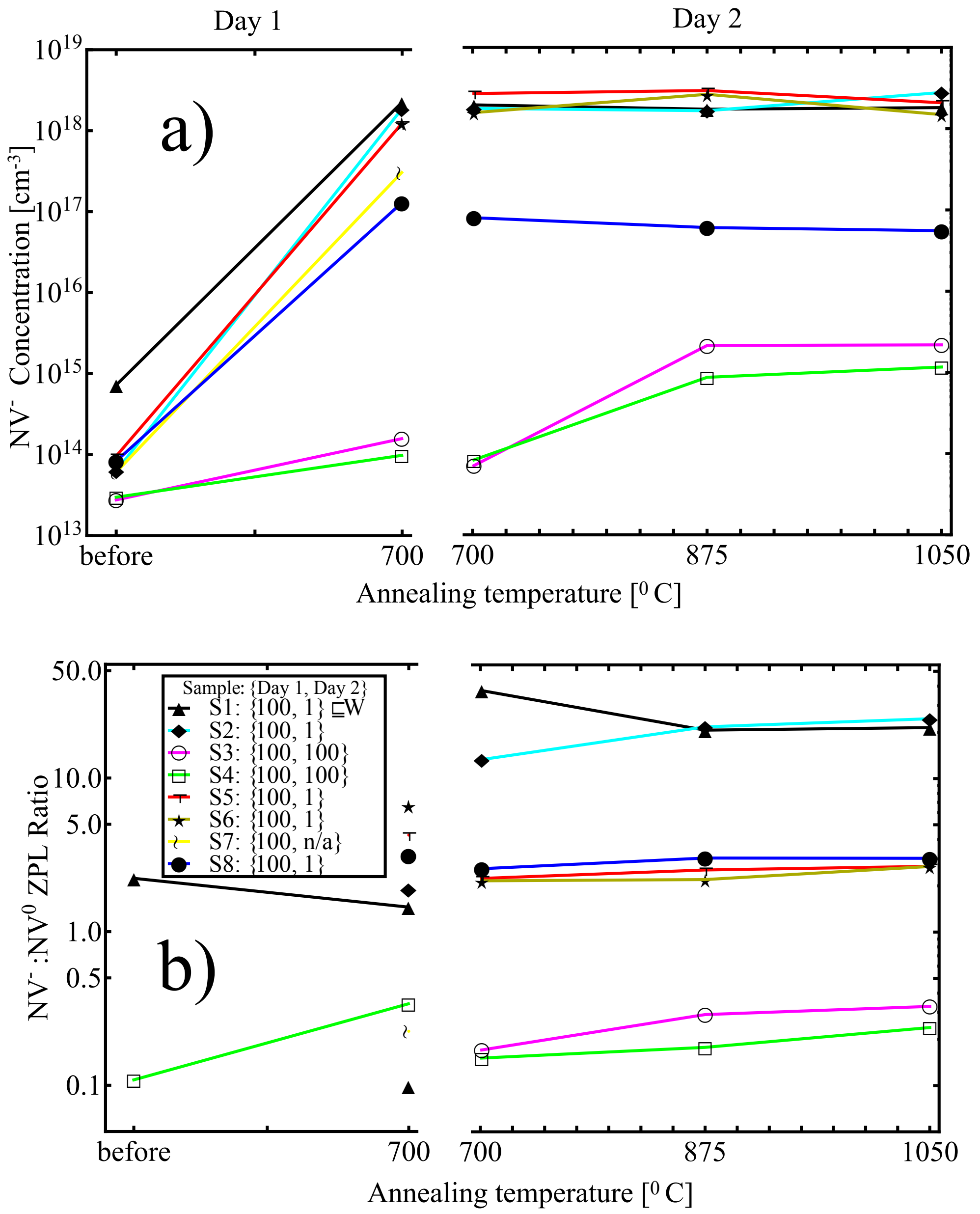

Figure 2.4: (a) NV$^-$ concentrations of electron-irradiated samples as a function of annealing temperature. (b) NV$^-$:NV^0 ZPL intensity ratio of the same samples as a function of annealing temperature. The data were taken during two different runs on separate days. On each day the collection location for each sample was the same, but in between days the location changed. The laser power for the data on each day is indicated in the legend. Filled plot symbols are used for all samples with high nitrogen content and empty symbols represent the two samples with $\lesssim 1$ ppm nitrogen. Error bars are not shown here but are discussed in the text.

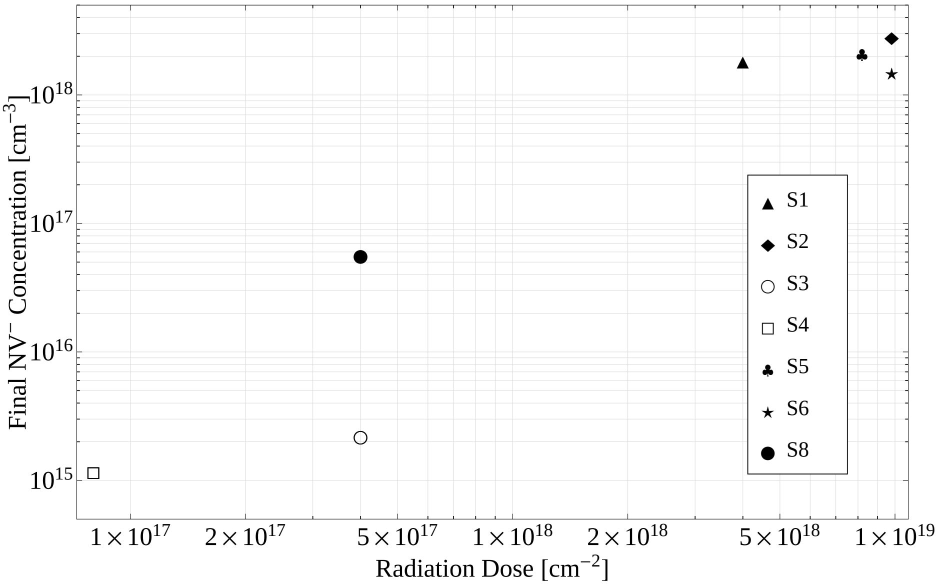

Figure 2.5: NV$^-$ concentrations near the surface as a function of dose for electron-irradiated samples after the final annealing at 1050°C. The data are the same as used in Fig. 2.4(a).

there is a large degree of uncertainty in the absolute values of the NV$^-$:NV^0 ratio for each sample. However, for a given day and a given sample, the laser power and collection location were constant, so it can be concluded from the flat temperature dependence seen in Fig. 2.4(b) for Day 2, and to a lesser extent also on Day 1, that the NV$^-$:NV^0 ratio is not strongly affected by annealing.

Figure 2.5 shows the NV$^-$ concentrations obtained after the final annealing at 1050°C as a function of radiation dose. As expected, the higher radiation dose generally leads to larger NV$^-$ concentrations. The initial nitrogen content is also an important factor, as evidenced by the factor of $\sim$ 25 difference between concentrations for Samples 3 and 8. These samples were subjected to the same radiation dose but their initial nitrogen concentration differed by approximately a factor of 100.

In conclusion, the doses and annealing temperatures listed in Tab. 2.1 were sufficient to create samples with a wide range of NV$^-$ concentrations. Annealing at 700 °C was sufficient to obtain the maximum NV$^-$ yield for samples with high nitrogen content, while an additional annealing at 875 °C was required for the low-nitrogen-content samples. The high-nitrogen samples exhibited a large NV$^-$:NV^0 ratio, while the low-nitrogen samples had a significantly lower ratio. Lastly, the concentration-measurement technique based on photoluminescence was reproducible to within approximately a factor of two even when different lateral positions in the sample were used.

2.4.2.3 Nitrogen-to-NV$^-$ conversion

#	[N] (ppm)	post-irrad. [Vacancies] (ppm)	final [NV$^-$] (ppm)	[NV$^-$]:[N]
1	$\lesssim 100$	45	10	$\gtrsim 10\%$
2	$\lesssim 100$	110	16	$\gtrsim 16\%$
3	$\lesssim 1$	5	.012	$\gtrsim 1\%$
4	$\lesssim 1$	1	.007	$\gtrsim 1\%$
5	$\lesssim 200$	90	12	$\gtrsim 6\%$
6	$\lesssim 200$	110	8	$\gtrsim 4\%$
8	$\lesssim 100$	5	.3	$\gtrsim 0.3\%$

Table 2.2: Sample Characteristics. Final NV$^-$ concentrations for the electron-irradiated samples are tabulated along with initial nitrogen content (reported by the commercial providers) and projected vacancy concentrations. These values are used to set a lower bound on the nitrogen-to-NV$^-$ conversion efficiency, as seen in the last column. The error in NV$^-$ concentration estimates, and consequently the error in conversion efficiency, is a approximately a factor of two, as discussed in the text.

A figure of merit for sensitive high-density magnetometry is the conversion efficiency of substitutional nitrogen to NV$^-$ centers, because any remaining paramagnetic nitrogen accelerates the rate of spin decoherence (see Sec. 2.4.4.4). For irradiation temperatures around those used in this work ($\lesssim 150°$C), the rate of vacancy production for 2-MeV electrons throughout millimeter-thick samples was determined experimentally to be ~ 1.25 vacancies/e$^-$/cm in Ref. [159] and ~ 1.5 vacancies/e$^-$/cm in Ref. [169] and theoretically to be ~ 2.2 vacancies/e$^-$/cm [174]. Since the electrons are relativistic, the difference in vacancy production between 2- and 3-MeV electrons is small [174], so we assume a vacancy production for the 3-MeV electrons used in this work of ~ 2 vacancies/e$^-$/cm. Using this value, along with irradiation doses from Tab. 2.1, Tab. 2.2 displays approximate initial concentrations of vacancies before annealing. The initial nitrogen concentrations reported by the manufacturers and the final NV$^-$ concentrations from Fig. 2.5 are also shown and these values are used to set a lower bound on the nitrogen-to-NV$^-$ conversion efficiency. Sample 2, having converted $\gtrsim 16\%$ of the initial nitrogen into NV$^-$ centers, shows the most promising conditions for high conversion efficiency. For this sample, the initial nitrogen concentration was $\lesssim 100$ ppm and the irradiation dose was 9.8×10^{18} cm^{-2}, corresponding to ~ 110 ppm vacancies. As discussed in Sec. 2.4.2.4, it is likely this dose was insufficient to maximize NV$^-$ formation.

2.4.2.4 Visible absorption

Optical magnetometry with spin ensembles requires that the samples be reasonably transparent over the spectral range of interest. In diamond magnetometry based

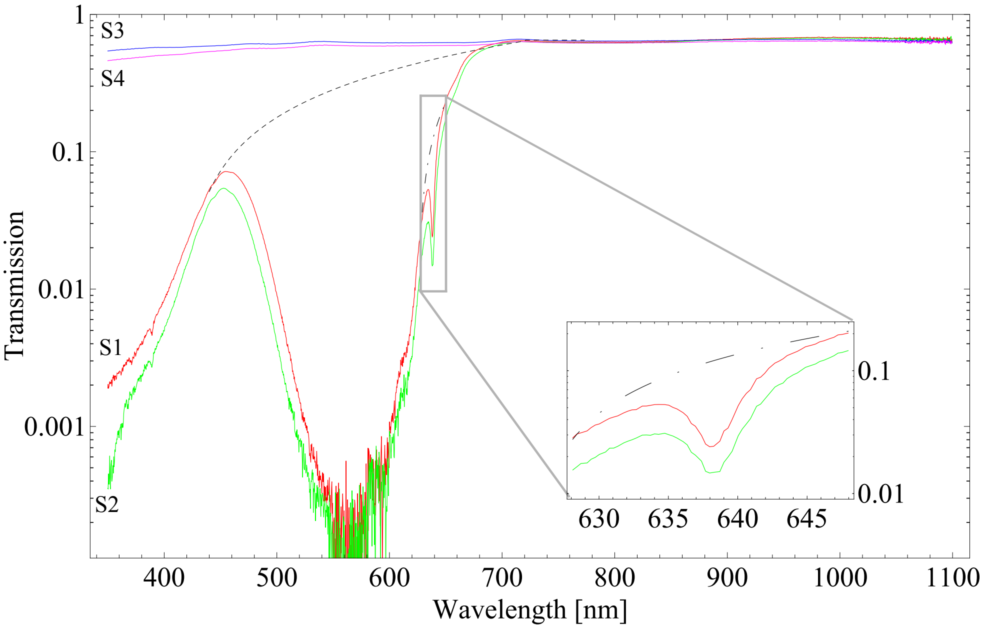

Figure 2.6: Room temperature transmission curves for four electron-irradiated samples after the final annealing at 1050°C. The beam path (i.e. the sample thickness) was 1 mm for Samples 1 and 2 (S1 and S2) and .5 mm for S3 and S4. The ZPL at ∼ 638 nm is visible for S1 and S2 and is blown up in the inset. The dotted lines represent the baselines used for Sample 1 in the effective vibrational-splitting and Huang-Rhys factor calculations (the baseline for Sample 2 was similar).

on NV⁻ centers, zero-phonon optical transitions at 638 nm and 1042 nm [19], as well as their broad phonon sidebands, provide possible channels for detection. To measure the opacity in this range, a Cary 50 spectrophotometer was used to obtain transmission spectra for four of the electron-irradiated samples (Samples $1-4$) after the final annealing at 1050°C. The visible spectra for a subset of these samples were also measured after the first annealing, and no significant differences in the spectra between these stages of annealing were observed.

Figure 2.6 shows the room-temperature transmission curves for these samples. For all four samples, the transmission in the wavelength region ∼ 700-1100 nm is approximately 66%. The loss of light can be accounted for by Fresnel reflection; the index of refraction of diamond is 2.4, which corresponds to a reflection of 17% off of each diamond surface for light at normal incidence in air.

In the wavelength region to the red of the ZPL and below ∼ 700 nm, Samples 1 and 2 exhibit absorption that increases rapidly with decreasing wavelength. Absorption at these wavelengths is due to the significant population of NV⁻ centers in the excited vibrational states at room temperature. After subtraction of the overall background and absorption due to the ZPL (baselines in Fig. 2.6), the ratio of the integrated absorption in this spectral region (638-700 nm) to the total integrated absorption is $\sim 11(2)\%$ for Sample 1 and $\sim 13(2)\%$ for Sample 2. If these values are taken to be the Boltzmann-distributed occupancy of excited vibrational states at room temperature, they would give a rough estimate for the effective ground-state vibrational-energy splitting [175] of 56(4) and 52(4) meV for the NV$-$ center, respectively. These values are in tolerable agreement with previous measurements based on emission spectra, where the effective vibrational-spacing in the $^3A_2$ ground state of the NV$^-$ center was estimated to be ~ 60 meV [73, 114].

In the region around $\sim 628 - 648$ nm, inset in Fig. 2.6, the NV$^-$ ZPL appears prominently in the spectrum for Samples 1 and 2, where at the peak of absorption approximately 98% of the light is absorbed. This corresponds to four absorption lengths for this 1-mm path length, with approximately one absorption length attributed to just the ZPL and the other three due to overlap of the PSB. To the blue of the ZPL, at $\sim 450 - 638$ nm, resides a broad feature which is a combination of the NV^0 and NV$^-$ phonon sidebands. The ZPL for NV^0 at 575 nm is obscured by this strongly absorbing region. For Samples 3 and 4, there are no visible spectral features, due to the low NV concentrations in these samples (see Tab. 2.2).

Based on the absorption data, it is possible to estimate the electron-phonon coupling parameter, also known as the Huang-Rhys factor [112], $S = -\ln(I_{ZPL}/I_{tot})$, where I_{ZPL} and I_{tot} refer to the integrated absorption intensities after normalization by the light frequency. While this relationship is only strictly correct at zero-temperature where quadratic electron-phonon coupling is suppressed, it was shown in Ref. [112] that, in NV$^-$ centers, the temperature-dependence of S is weak. In that work it was reported that S increases by less than 30% from 2 to 350 K. Analysis of the data in Fig. 2.6 gives, after subtracting the linear background (dashed lines in the figure), $S \approx 3.9$ for Sample 1 and 4.0 for Sample 2, which is within the range of values in the literature for NV$^-$ centers at or below 80 K ($4.8, 4.3, 2.8$ in Ref. [114], and 3.7 in Ref. [73]). The value used for I_{tot} is a slight over-estimate, as the phonon sideband from the NV^0 centers overlaps, but this effect is small ($\lesssim 2\%$) since the concentration of NV^0 was small compared to that of NV$^-$ for both samples (see Sec. 2.4.2.2).

Another important observation from Fig. 2.6 is the absence of an absorption feature at 741 nm, the wavelength of the ZPL of the neutral vacancy center, GR1. The neutral vacancy concentration has previously been calibrated based on the GR1 integrated ZPL in absorption [131, 176]. Based on this calibration and the lack of an identifiable ZPL, a conservative upper bound of 1 ppm can be placed on the concentration of neutral vacancy centers for Samples 1 and 2. This suggests that the NV conversion efficiency for these samples may be limited by the number of vacancies present after irradiation. Recall from Tab. 2.2 that the vacancy concentration was predicted to be slightly larger than the nitrogen concentration for Sample 2. Since all of the neutral vacancies are gone after the final annealing, it is likely that there is a competing process to the vacancy capture by the substitutional nitrogen atoms.

We also considered the possibility that many vacancies remain after annealing, but the vast majority of remaining vacancies were actually negatively charged, due to the high concentration of nitrogen donors, and therefore do not contribute to the GR1 absorption. The negatively charged vacancy center, ND1, is not visible in the absorption spectra because its ZPL is at 396 nm [16]. This wavelength coincides with the large background absorption, presumably due to photo-ionization of the substitutional nitrogen, prohibiting a direct measurement of the negatively charged vacancy concentration. However, as will be shown in Sec. 2.4.2.5, the concentration of positively charged nitrogen, the likely product of ND1 formation, can be measured from infrared absorption spectra and was found to be 15(3) and 19(4) ppm after the final annealing for Samples 1 and 2, respectively. Since much of this concentration can be attributed to nitrogen's role as a donor in NV^- formation (recall that the NV^- concentrations were approximately 10 and 16 ppm for Samples 1 and 2, respectively), a conservative upper bound of 10 ppm can be placed on the negatively charged vacancy concentration in both samples. Since this upper bound represents a small fraction of the estimated initial vacancy concentration (Tab. 2.2), it remains likely that in order to maximize the NV conversion efficiency higher radiation doses should be explored.

For Samples 1 and 2, the visible-absorption measurements can also be used as a cross-check on the NV^- concentrations determined from the PL spectra (Sec. 2.4.2.2) [173, 131]. Using the calibration published in Ref. [131], the integrated ZPLs for Samples 1 and 2 correspond to NV^- concentrations of 8 and 10 ppm, respectively, which is in tolerable agreement with the concentrations measured from the PL spectra (10 and 16 ppm, respectively). As the calibration established in that work was intended for low-temperature absorption, the somewhat lower $[NV^-]$ values can be partly attributed to the slightly lower Huang-Rhys factor at room-temperature [112].

In summary, visible-absorption measurements establish that even at high radiation doses the dominant source of absorption in the visible and near-infrared is due to NV centers, and not other radiation damage. The absence of GR1 absorption suggests that higher radiation doses should be explored for optimizing NV yield. The absorption spectra were also used to confirm the NV^- ground vibrational-state occupancy and Huang-Rhys factors from the literature and the NV^- concentrations determined from the absorption ZPL provide good agreement with those determined from the PL spectra in Sec. 2.4.2.2.

2.4.2.5 Infrared absorption

The presence of paramagnetic nitrogen has important implications for magnetometry, as discussed below in Sec. 2.4.4.4. Infrared absorption measurements were made with a Nicolet Magna IR-750 FTIR spectrometer to measure the leftover nitrogen concentration after the final annealing (Fig. 2.7). Nitrogen-rich diamonds display a broad vibrational absorption band peaking around 1130 cm^{-1} [177] that has been calibrated with respect to the substitutional nitrogen concentration using

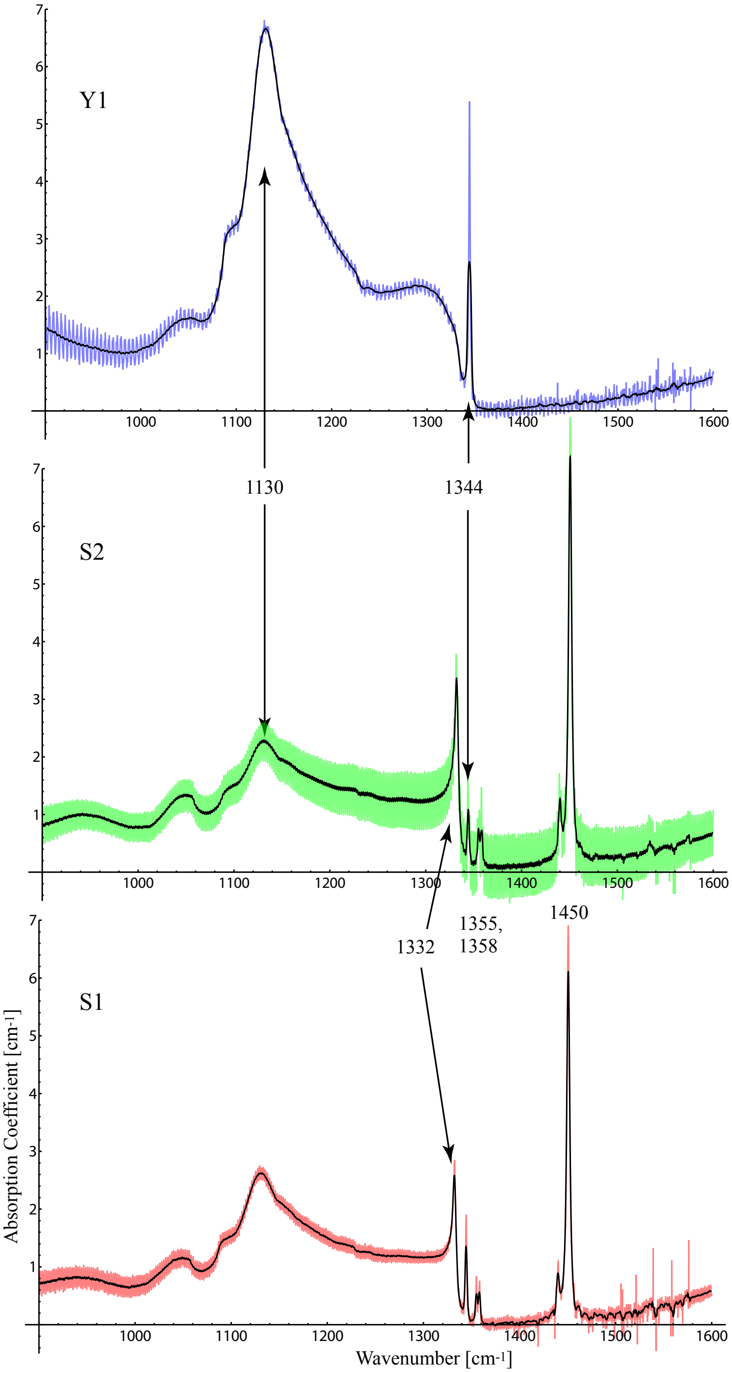

Figure 2.7: Infrared spectra for Samples 1, 2, and "Y1" after the final annealing. Each spectrum represents averaging of 64 scans and the resolution of the spectrometer was set to 0.25 cm^{-1}. The rapid oscillations are due to etaloning at normal incidence, and they have been smoothed by a moving average (black lines) in order to quantify the peak at ~ 1130 cm^{-1} (see text). Features mentioned in the text are labeled by their wavenumbers.

ESR and inert-gas fusion techniques [178, 179]. According to this calibration, an absorption coefficient of 1 cm^{-1} corresponds to a substitutional nitrogen concentration of approximately 22 ppm [179]. Figure 2.7 shows the infrared spectra for Samples 1 and 2 after the final annelaing, and a third Sumitomo HPHT diamond ("Y1") with very similar specifications that had not been irradiated or annealed. Based on the spectral feature at $\sim$ 1130 cm^{-1}, the nitrogen content for Samples 1, 2, and Y1 were 58(8), 49(7), and 146(20) ppm, respectively, where the uncertainty is based on the spread of the calibration values in the literature [178, 179]. The sharp spectral feature at 1344 cm^{-1} present in all three samples is also associated with the single substitutional nitrogen [177]. Both of these peaks are more intense for Sample Y1, presumably because Samples 1 and 2 contain NV centers and other nitrogen-related centers formed during irradiation and annealing. The most prominent feature in the FTIR spectra for Samples 1 and 2 is at 1450 cm^{-1}, which was tentatively assigned to a vibrational mode of interstitial nitrogen [180, 181]. The smaller features at 1355 and 1358 cm^{-1} may also be related to this defect [182]. The production of this interstitial defect may be due to irradiation, since these features are not present in Sample Y1.

The spectral feature at 1332 cm^{-1}, present only in Samples 1 and 2, has been linked to positively charged substitutional nitrogen, N^+ (Ref. [131]). In that work, it was argued that because of nitrogen's role as a donor in NV^- formation, the concentration of N^+ after the final annealing should be roughly equal to the concentration of NV^-. Using the calibration of the 1332 cm^{-1} peak from that work (1 cm^{-1} of absorption corresponds to 5.5 ± 1 ppm of N^+), the NV^- concentrations for Samples 1 and 2 would be 15(3) and 19(4) ppm. Since nitrogen is a donor in the formation of other centers, such as the negatively charged vacancy (Sec. 2.4.2.4), it can be expected that $[\mathrm{N}^+]$ would be somewhat higher than $[\mathrm{NV}^-]$. Thus these values for $[\mathrm{NV}^-]$ are in excellent agreement with the values (10 and 16 ppm, respectively) measured using PL spectra in this work.

In conclusion, the FTIR measurements indicate that a large concentration of paramagnetic nitrogen remains in the samples even after the highest irradiation doses and annealing temperatures studied here. The absorption of the 1332 cm^{-1} peak was found to be in excellent agreement with the NV^- concentrations determined from PL spectra.

2.4.3 Light-power dependence of NV^0 and NV^- concentrations

The neutral NV center, NV^0 presents a similar problem to ultra-sensitive magnetometry as the remaining substitutional nitrogen, since it is also paramagnetic [96] and therefore limits NV^- dephasing times. Further, since the emission spectrum of NV^0 partly overlaps with the phonon sideband of the NV^- defect, the presence of NV^0 leads to a background fluorescence signal that reduces measurement contrast. In previous work [183, 184], it was shown that the NV^- and NV^0 concentrations can change upon illumination by light in a range of wavelengths including 532 nm, the

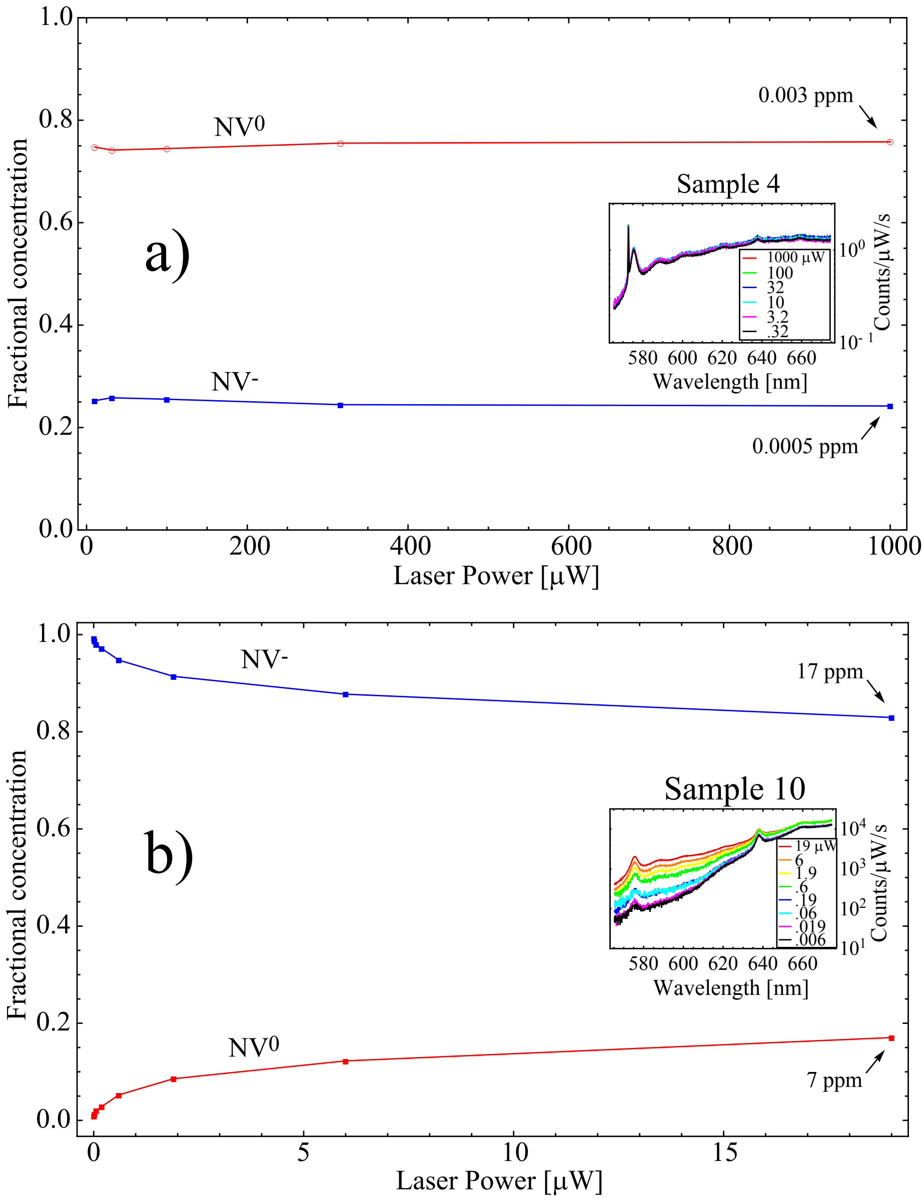

Figure 2.8: Relative NV⁻ and NV^0 concentrations for (a) Sample 10 and (b) Sample 4 after the first annealing (700°C and 800°C, respectively) as a function of incident laser power. The concentrations were obtained from fluorescence spectra (insets) taken at a depth of approximately 36 μm, for Sample 10, and 12 μm, for Sample 4. Determination of NV^0 concentration was made by weighting the relative ZPL intensity according to the difference in room-temperature Huang-Rhys factors; $S \sim 3.3$ for NV^0 [16] and $S \sim 4.0$ for the NV$^-$ center (Sec. 2.4.2.4). The laser beam was focused to a diameter of approximately 0.5 μm for all measurements.

wavelength used for excitation in this work. In particular, in Ref. [183] it was reported that the NV$^-$:NV^0 ratio dropped with increasing laser power and identified direct photo-ionization of the NV$^-$ center and ionization of nearby potential nitrogen donors as the primary causes.

Figure 2.8 shows the relative NV$^-$ and NV^0 concentrations determined from the PL spectra (Sec. 2.4.2.1) for (a) Sample 10 and (b) Sample 4 as a function of incident laser power. By relative, we mean that the NV$^-$ and NV^0 concentrations have been normalized such that, at any given laser power, their sum is 1. In order to determine the NV^0 concentration, the difference in Huang-Rhys factors for NV^0 and NV$^-$ were used for normalization, since the NV^0 ZPL for the single NV center (Fig. 2.3(a)) was not visible in the spectrum. As seen in Fig. 2.8, the laser-light intensity has a significant effect on the NV charge state for the high-nitrogen-concentration Sample 10, but does not affect the low-nitrogen-concentration Sample 4. Since at very low light power Sample 10 has a large [NV-]:[NV^0] ratio and Sample 4 has a very low ratio, the results in Fig. 2.8 can be interpreted as a small fraction of NV$^-$ being converted to NV^0 due to the laser light until the ratio reaches some minimum saturation level. Note that the range of laser powers explored for Sample 4 was higher than that of Sample 10, due to the low overall NV concentration in this sample. Similar plots were made after each annealing, but further annealing was found to have no measurable impact. While the mechanism for changing the NV charge state (i.e. one- or two-photon process) cannot be confirmed from this data set, the results indicate that sensitive magnetometry requires careful optimization of the laser light power.

2.4.4 Optically detected magnetic resonance (ODMR)

2.4.4.1 NV$^-$ electronic structure

One of the crucial features of nitrogen-vacancy ensembles for practical magnetometry is that the NV$^-$ centers can be optically pumped and interrogated using visible light over a broad range of wavelengths (see Fig. 2.6). Figure 2.9(a) shows the crystallographic cell for the trigonal NV$^-$ center in one of four possible orientations, corresponding to the N-V axis along each of the dangling bonds. Figure 2.9(b) shows the level diagram with energy levels and allowed transitions labeled according to the most current model posited in Refs. [19, 107]. Based on C$_{3v}$ symmetry [73] and results from early electron-spin-resonance (ESR) [70] and hole-burning experiments [71], it is known that the center's ground state is a $^3A_2$ spin-triplet and the state which can be directly accessed by an electric dipole transition is ^3E. The ground state is split by 2.88 GHz due to the strong spin-spin interaction arising from the electron charge distribution being highly localized near each of the three carbon atoms [70]. At low temperature the ^3E state is an orbital doublet split by transverse strain, but at room temperature the orbital components appear to average [107], and thus it is represented by a single orbital with spin-spin splitting of 1.42 GHz [106]. The $^3A_2$

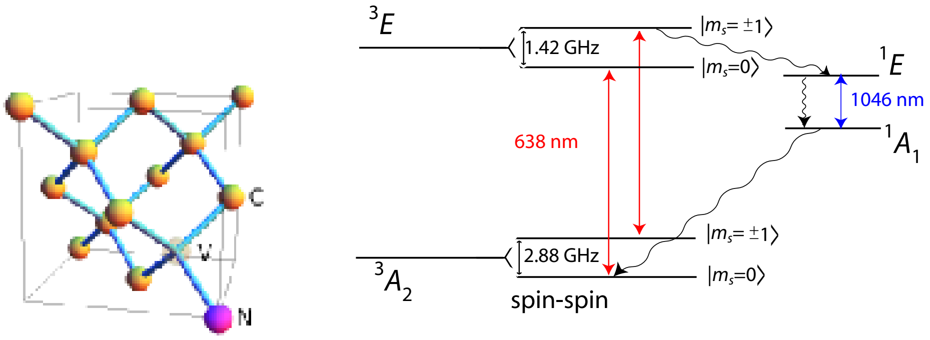

a) b)

Figure 2.9: (a) Crystallographic cell for the NV center in diamond. The center has C_{3v} symmetry and the line that contains both N and V defines the symmetry axis, of which there are four possible orientations. C–Carbon, N–Nitrogen, V–Vacancy. (b) Level diagram for NV^- center showing spin-triplet ground and excited states, as well as the singlet system responsible for intersystem crossing (see text). The transition wavelengths are for the ZPL, with radiative transitions indicated by solid arrows and non-radiative transitions by wavy arrows.

ground state has a single non-degenerate electronic orbital and thus is immune to first-order shifts due to strain.

In thermal equilibrium, the ground state sublevels are nearly equally populated, but after interaction with light resonant with the $^3A_2 \rightarrow {}^3E$ transition (excited here on the phonon sideband at 532 nm), the $|m_s = \pm 1\rangle$ sublevels become depopulated and the $|m_s = 0\rangle$ sublevel eventually takes on the excess. Theoretical considerations and spin-dependent lifetime measurements suggest that the process responsible for the ground-state polarization is the decay, due to spin-orbit interaction, from the $|m_s = \pm 1\rangle$ sublevels of the ^3E to a singlet state(s) with lower energy [185, 104, 153]. Pulsed-pump transient measurements have shown that the $|m_s = \pm 1\rangle$ can decay back to the $|m_s = 0\rangle$ through the singlet system after approximately 300 ns [104]. As this decay is mostly non-radiative, optical pumping into the $|m_s = 0\rangle$ sublevel results in an increase in fluorescence with a contrast as high as 30%, limited by the branching ratio of approximately 0.5 for the $|m_s = \pm 1\rangle$ sublevels decay to the singlet system [14]. Until very recently this singlet system, thought to be ^1A and/or ^1E from C_{3v} group theory considerations [104, 19], had not been directly detected. Weak infrared emission at 1042 nm was finally observed in Ref. [19] and the magnetic-field and strain dependence of the fluorescence spectra indicate that the emission is indeed involved in the optical pumping mechanism.

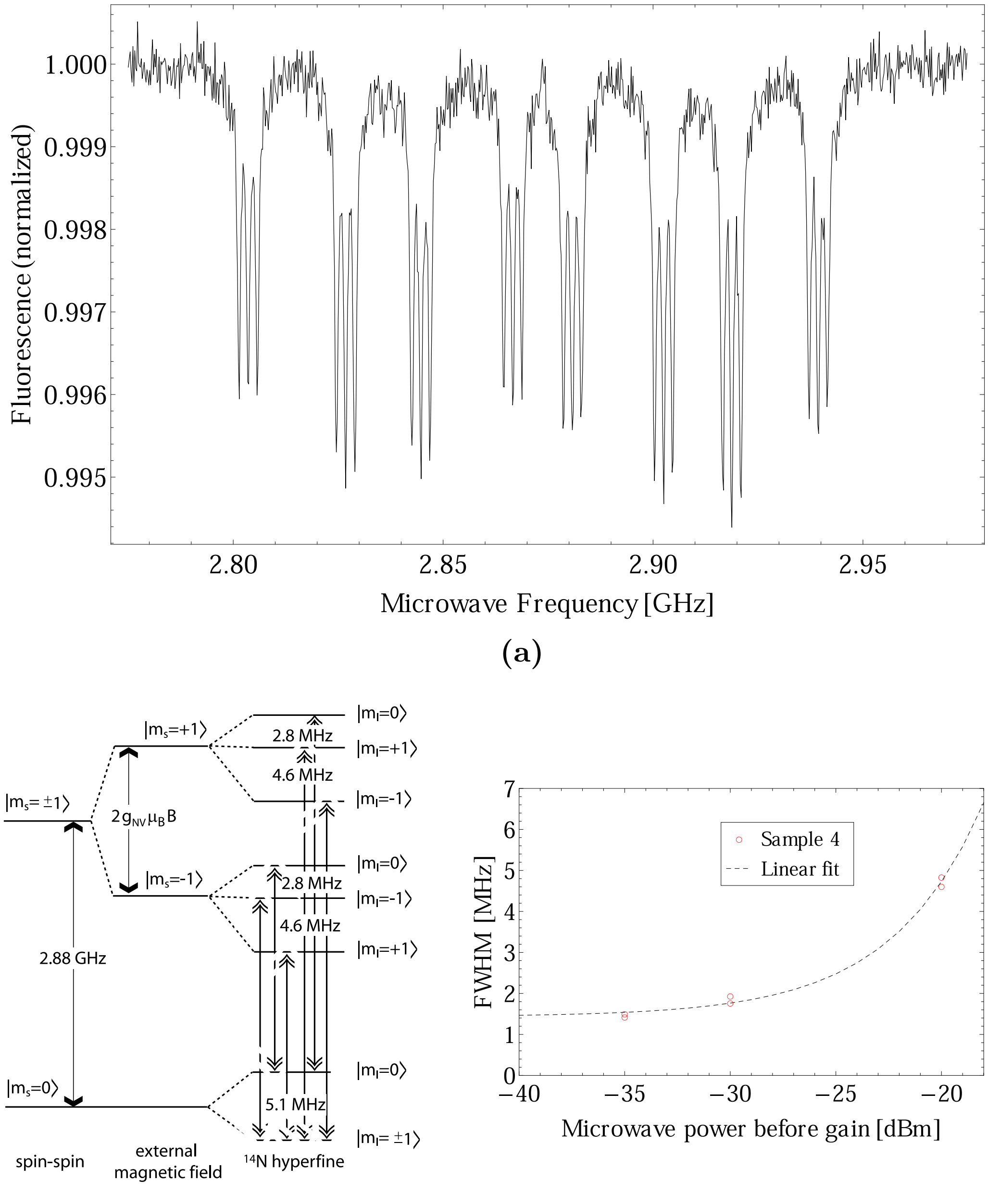

(a)

(b)

(c)

Figure 2.10: (a) ODMR spectrum for Sample 3. The 24 separate resonances correspond to two different $|\Delta m_s| = 1$ transitions, four different NV orientations, and three different ^{14}N hyperfine transitions. The orientations were split by a ∼ 50 G field. (b) Level diagram for the ground-state magnetic dipole transitions induced by the microwave field in the ODMR measurements. The selection rules for these transitions are $|\Delta m_s| = 1$ and $\Delta m_I = 0$. The values for the ^{14}N hyperfine splitting are taken from Ref. [17]. (c) Microwave-power dependence (log-scale) of the relaxation rate for Sample 4 for a laser power of 213 μW. Microwaves from a signal generator were amplified and applied with a ∼ 1-mm-diameter current loop with unmatched impedance. The microwave power was measured at the output of the signal generator prior to the ∼ 30 dB amplifier. The FWHM linewidth of each $|\Delta m_s| = 1, \Delta m_I = 0$ transition for one of the orientations was plotted as a function of microwave power. A linear fit for the lowest-power points (dashed line) was used to extrapolate the linewidth to zero microwave power. The standard error in the fit parameter serves as the uncertainty in the measurement.

2.4.4.2 Optically detected magnetic resonance technique

The transverse spin relaxation time, T_2^*, is critically important for spin-precession magnetometry, as it places bounds on both the minimum sensitivity and laser power of broadband sensors (Sec. 2.4.5). In order to measure T_2^*, the technique of ODMR was employed after the final annealing. In this technique, a microwave field is tuned to the ground-state ESR frequency of the NV⁻ center and the fluorescence resulting from illumination by light exciting the ${}^3A_2 \to {}^3E$ transition is monitored [70, 122]. Optical pumping transfers the NV⁻ centers to the $|m_s = 0\rangle$ ground state. An external magnetic field is applied, and the electronic spin sublevels $|m_s = \pm 1\rangle$ couple to the component B_z along the N-V axis, leading to Zeeman energy shifts of $\Delta E = m_s g_s \mu_B B_z$, where $g_s = 2.0028$ is the NV⁻ electronic Landé factor [70] and $\mu_B \approx 1.40$ MHz/G is the Bohr magneton. When the oscillating magnetic field has frequency equal to the splitting between the $|m_s = 0\rangle$ and $|m_s = \pm 1\rangle$ magnetic sublevels, the component transverse to the N-V axis drives the magnetic dipole transition and repopulates the $|m_s = \pm 1\rangle$ magnetic sublevels, counteracting the anisotropy produced by optical pumping. With the pump light still on, the increase in population in $|m_s = \pm 1\rangle$ leads to non-radiative decay through the singlet system, reducing the fluorescence emitted by the center. Thus the ESR signal is the change in fluorescence registered when scanning the frequency of the microwave field.

An example of an ODMR spectrum is shown in Fig. 2.10(a). An additional layer of complexity in the spectrum is the presence of the hyperfine interaction with the nuclear-spin-one ^{14}N nucleus, which splits each $|\Delta m_s| = 1$ resonance into three hyperfine peaks ($\Delta m_I = 0$) with an equal spacing of 2.3 MHz at zero-magnetic field [122]. Figure 2.10(b) shows the level diagram for the allowed ground-state transitions. The four different orientations of the NV⁻ center are degenerate in the absence of magnetic field, but this degeneracy was removed with a static magnetic field of magnitude ≈ 50 G, applied using a permanent magnet. Both fits to the data and numerical diagonalization of the 9×9 spin hamiltonian [17] confirmed that the spin-state mixing due to this applied field, particularly the component perpendicular to the N-V axes, causes the hyperfine splitting to vary by $\lesssim 0.1$ MHz.

2.4.4.3 Results of ODMR measurements

The resonance profile corresponding to each N-V orientation and $|\Delta m_s| = 1$ coherence was fit with three Lorentzian functions of equal amplitude and equal linewidth, γ, given as full-width at half maximum (FWHM). Equal spacings between the centers of adjacent Lorentzians of 2.2 MHz were used, even when the ^{14}N hyperfine splitting could not be resolved. The effective transverse spin relaxation times, $T_2^* = 1/(\pi\gamma)$, and associated uncertainties were obtained from the ODMR spectra by extrapolating γ to zero microwave power (Fig. 2.10(c)) with a linear fit. Density-matrix calculations confirmed that γ is, to lowest order, linear in the microwave power. The

Sample #	[N] (ppm)	final [NV$^-$] (ppm)	Laser Power (μW)	T_2^* (ns)
1	$\lesssim 100$	10	5	66(8)
2	$\lesssim 100$	16	188	118(48)
3	$\lesssim 1$	.012	130	$\gtrsim 291$
4	$\lesssim 1$	.007	213	222(11)
5 (spot 1)	$\lesssim 200$	1.0	24	27(4)
5 (spot 2)	$\lesssim 200$	.02	100	128(64)
5 (spot 3)	$\lesssim 200$	2.5	240	145(63)
8	$\lesssim 100$	.3	188	114(25)

Table 2.3: Effective transverse spin relaxation times, T_2^*, extrapolated to zero microwave power, for several electron-irradiated samples at the given laser powers (focused to ~ 0.5-μm diameter). For Sample 5, three locations, corresponding to spots in different growth-sectors, were investigated. The uncertainty estimates for all samples except Sample 3 come from the standard error of the linear fits, as shown in Fig. 2.10(c). For Sample 3, only one low microwave power, -30 dBm before the amplifier, was investigated (shown in Fig. 2.10(a)). The lower bound on T_2^* for this sample corresponds to one standard deviation below the statistical average of the resonance widths.

resulting T_2^* times are tabulated in Tab. 2.3 for each sample at the given laser power. The laser-power dependence was not studied here though the light power was varied from sample to sample in order to maximize the signal on the photon counter. This dependence will be investigated in future work.

2.4.4.4 Contributions to T_2^*

For the HPHT-synthesized Sample 5, ODMR spectra at three different locations, corresponding to sectors with very different initial nitrogen concentrations, were observed, and the NV$^-$ concentrations at these locations were estimated based on the integrated ZPL, as described in Secs. 2.4.2.1 and 2.4.2.2. Since the irradiation was uniform throughout the sample, the wide variation of T_2^*, from 27 ns to 145 ns is probably not due to vacancy-related defects other than NV centers, unless the formation of such centers is strongly correlated with the local concentration of nitrogen.

For dilute spins, the contribution of NV$^-$–NV$^-$ dipolar interactions to the magnetic-resonance broadening can be approximated by assuming that each NV$^-$ center couples to only the nearest-neighboring NV$^-$ center. For an ensemble, this dipolar coupling leads to a spin-relaxation contribution on the order of $T_{NV} \approx 1/[(g_s\mu_B)^2 n_{NV}]$, where n_{NV} is the NV$^-$ concentration [13]. For Sample 2, this corresponds to $T_{NV} \approx 1$ μs, meaning that NV$^-$–NV$^-$ coupling is significant but not necessarily the primary source of relaxation. For Sample 5, spot 3 has a much higher NV$^-$ concentration but similar

T_2^* to spot 2, providing evidence that NV⁻–NV⁻ relaxation is not the dominant source of relaxation in this sample.

For nitrogen-to-NV⁻ conversion efficiency of less than 50%, the contribution of substitutional-nitrogen dipolar interactions to NV⁻ decoherence is expected to be even larger, as the paramagnetic nitrogen has similar coupling strength. Similarly to the estimate for NV⁻–NV⁻ interactions, the characteristic timescale for this decoherence is $T_N \approx 1/((g_s\mu_B)^2 n_N)$, where we ignore the small difference in g-factors between NV⁻ and nitrogen [70]. Recall from Sec. 2.4.2.5 that Samples 1 and 2 had final nitrogen concentrations on the order of 50 ppm, giving a value of $T_N \approx 300$ ns. Samples 1, 2, and 5-8 all had similar initial concentration of nitrogen ($\lesssim 100$ ppm). Since the irradiation and annealing process converted no more than 16 ppm of nitrogen into NV⁻ centers, it is likely that relaxation due to remaining paramagnetic nitrogen is the dominant cause of relaxation in all of these samples.

Another well-known cause for relaxation is inhomogenous broadening due to dipolar hyperfine coupling of nearby ^{13}C nuclear spins (natural 1.1% abundance in all samples). Based on experiments on single NV centers, this spin-relaxation contribution is in the range $T_{C_{exp}} \approx 0.3 - 1.5$ μs [87, 128, 42]. Those experimental values are not too far from the T_2^* seen for Samples 3 and 4, where the nitrogen content was low enough that ^{13}C is likely a major source of inhomogenous broadening due to dipolar coupling.

In conclusion, dipolar broadening due to paramagnetic nitrogen is predicted to be the dominant dephasing mechanism in the high-nitrogen-concentration samples, followed closely by dephasing due to other NV centers and ^{13}C nuclear spins. For the low-nitrogen-concentration ([N]$\lesssim 1$ ppm) samples, dephasing due to the ^{13}C nuclear spins was likely the dominant form of relaxation.

2.4.5 Prospects for ultra-sensitive magnetometry

The performance of a magnetometer based on electronic spins is, in principle, limited by the spin-projection noise. The minimum detectable magnetic field, δB, is [7]:

$$\delta B \simeq \frac{1}{g_s\mu_B}\frac{1}{R\sqrt{\eta}}\frac{1}{\sqrt{NtT_2^*}}, \tag{2.1}$$

where R is the measurement contrast, η is the detection efficiency, N is the number of spin centers, and t is the integration time. It is interesting to estimate the magnetic sensitivity of a sensor based under ideal conditions. We choose Sample 2, as it has the highest product of density and T_2^*, and we speculate that improved experimental techniques will allow the signal from nearly all NV centers to be collected with contrast $R \sim 0.3$ and efficiency $\eta \sim 0.1$. Using these values the quantum shot-noise limited sensitivity would be ~ 150 fT/$\sqrt{\text{Hz}}$ for a 100 μm-scale magnetometer based on this sample. This approaches the sensitivity of superconducting quantum interference devices (SQUIDs) with similar spatial resolution [8]. Moreover, the isotropy of the system makes it easily size scalable, and the advantage of a such a compact device working in a broad range of temperatures–from room temperature down to liquid helium temperatures–makes NV-ensembles an attractive candidate for many types of magnetic-sensing applications. Of course, much work needs to be done to experimentally realize the shot-noise limit, including thorough analysis and mitigation of sources of decoherence and improved experimental techniques. In particular, we note that the optimal optical pumping rate for this model magnetometer is on the order of $N_{NV}/T_2^* = 2.8 \times 10^{12}/(118 \text{ ns})$. This corresponds to approximately 8 W for 532 nm laser light. Thus, lengthening the effective relaxation time is essential in order to improve sensitivity while maintaining practical light powers.

2.5 Conclusion

Proposals for high-density ensemble magnetometers predict sensitivities rivaling the most sensitive atomic and superconducting magnetometers [13]. Development of such magnetometers requires reliable production of diamond samples with control over the NV$^-$ concentration as well as other defects which may contribute to spin relaxation. In this work, ten diamond samples were prepared under very different conditions and their optical and spin-relaxation properties were characterized. The compiled results show that electron-irradiated samples annealed at 700°C for two hours can have NV$^-$ concentrations on the order of 10 ppm, a reasonable benchmark for 100 μm-scale magnetometry at the 100 $\text{fT}/\sqrt{\text{Hz}}$ sensitivity level. For samples with large initial nitrogen concentrations approaching 100 ppm, the highest irradiation dose used in this work, $\sim 10^{19}$ e$^-$/cm^2, was still insufficient for maximum nitrogen-to-NV$^-$ conversion. Nitrogen concentrations on the order of 50 ppm remain in the samples, so in order to maximize the conversion efficiency, higher doses will be explored in future work. Conveniently, the irradiated samples remained mostly transparent in the spectral region of interest–absorption in the visible and near-infrared spectrum was due almost entirely to NV centers. Effective relaxation times above 100 ns have been observed for some of the high-NV$^-$ concentration samples, likely limited by remaining paramagnetic nitrogen. A 100 μm-sized magnetic sensor based on this sample operating under ideal conditions should achieve a sensitivity of $\sim 150\ \text{fT}/\sqrt{\text{Hz}}$. In order to improve on this limit, future work is necessary to mitigate the dominant causes of relaxation.

2.6 Acknowledgements

The authors would like to thank B. Patton and S. Rochester for help with modeling and data visualization, T. Sauvage for proton irradiation, and P. Hemmer for extensive comments and suggestions. We also thank V. Bouchiat, C. Hovde, D. Twitchen, and R. Walsworth for providing helpful comments, R. Segalman and J. Sun for providing the Cary 50 spectrometer, and M. Donaldson and W. Vining for help with FTIR measurements. This work was supported by ONR-MURI and the Polish Ministry of Science (grant NN 505 0920 33).

Chapter 3

Temperature dependence of the nitrogen-vacancy magnetic resonance

This chapter (excluding Sec. 3.9) was previously published in Ref. [118] and is republished here, with minor changes, with permission.

3.1 Abstract

The temperature dependence of the magnetic resonance spectra of nitrogen-vacancy (NV^-) ensembles in the range of 280-330 K was studied. Four samples prepared under different conditions were analyzed with NV^- concentrations ranging from 10 ppb to 15 ppm. For all samples, the axial zero-field splitting (ZFS) parameter, D, was found to vary significantly with temperature, T, as $dD/dT = -75.0(6)$ kHz/K. The transverse ZFS parameter, E, was non-zero (between 1 and 8 MHz) in all samples, and exhibited a temperature dependence of $dE/(EdT) = -1.5(5) \times 10^{-4}$ K^{-1}. The results might be accounted for by considering local thermal expansion. The temperature dependence of the ZFS parameters presents a significant challenge for diamond magnetometers and may ultimately limit their bandwidth and sensitivity.

3.2 Introduction

Magnetometers based on nitrogen-vacancy (NV) ensembles in diamond [13, 12, 48] promise high-sensitivity, rivaling those of superconducting quantum interference devices (SQUIDs) [8] and alkali vapor magnetometers [7], in a scaleable solid state system that can be operated over a wide range of temperatures. This remarkable combination of spatial resolution [14, 152] and magnetic sensitivity [42] make diamond magnetometers promising candidates for remote-detection and low-field nuclear magnetic resonance spectroscopy [186, 23, 187, 25], nano-scale biological imaging [15, 14, 39, 38], and studies of novel magnetic and superconducting materials

[188, 48]. Until now, the temperature dependence of the magnetic resonance spectra has not been systematically studied and has only briefly been mentioned in the literature [77, 48]. In this chapter, we report a striking temperature dependence of the magnetic-resonance spectra of NV$^-$ ensembles in diamond over the temperature range of 280-330 K. These findings have important implications for the design of diamond magnetometers and may ultimately limit their sensitivity.

3.3 Experiment procedure

The resonance spectra were recorded using the continuous-wave Fluorescence Detected Magnetic Resonance (FDMR) method [122, 77]. Light from a 514-nm Argon-ion laser was focused with a 2.5 cm focal length lens onto the diamond samples, exciting the NV$^-$ centers' $^3A_2 \rightarrow {}^3E$ optical transition via a phonon sideband [104]. The same lens was used to collect fluorescence from the diamond which was then passed through a dichroic mirror and a 650-800 nm bandpass filter and detected with a photodiode. Noise due to laser power fluctuations was reduced by normalizing the fluorescence signal to a reference photodiode which monitored the incident laser power. The output of a microwave signal generator was amplified, passed through a straight $\sim$ 200-μm diameter copper wire of length $\sim$ 5 mm placed within 500 μm of the focused light beam, and terminated with 50-Ω impedance. For temperature control, the diamond was thermally connected to a copper heatsink and placed inside an insulated aluminum housing. The temperatures of the heat sink and housing were controlled with separate thermoelectric (TE) elements. Unless otherwise stated, the results reported in this Letter were obtained with a magnetic field of $\lesssim$ 1 G, laser-light power of $\sim$ 150 mW, and microwave power (after the wire) of $\sim$ 10 dBm.

For temperature scans, the temperature of the copper plate in direct thermal contact with the diamond was monitored with an AD590 sensor. The FDMR spectra were recorded with the temperature stabilized so that temperature excursions were less than 0.05 K over 5 min. In order to avoid stray magnetic fields when recording the spectrum, the currents supplied to both TE elements were chopped at a frequency of 2 Hz using photoMOS circuits, and the spectra were recorded only when the TE currents were off. The process was repeated until the temperature had been scanned through the 280-330 K range several times in both directions.

3.4 Zero-field Hamiltonian and fitting procedure

The NV-ensemble magnetic-resonance spectroscopy has been described, for example, in Refs. [70, 122, 20, 121, 12]) and is only briefly summarized here. Optical pumping via a spin-selective decay path collects NV centers (total spin $S = 1$) in the $|m_s = 0\rangle$ ground-state magnetic sublevel [104]. In the absence of external fields, the $|m_s = 0\rangle$ and $|m_s = \pm 1\rangle$ levels are split by an energy equal to the axial zero-field splitting (ZFS) parameter, $D \approx 2.87$ GHz. For perfect C_{3v} symmetry, the transverse ZFS parameter is $E = 0$ and the $|m_s = \pm 1\rangle$ levels remain degenerate. When the frequency of a microwave field that is transverse to the symmetry axis is tuned to the energy splitting between the $|m_s = 0\rangle$ and $|m_s = \pm 1\rangle$ levels, NV centers are transferred to the $|m_s = \pm 1\rangle$ sublevels, resulting in diminished fluorescence with a contrast as high as 30% [14]. In the presence of an applied magnetic field, B, the $|m_s = \pm 1\rangle$ levels split, revealing resonances separated by $2g_{NV}\mu_B B$, where $g_{NV} = 2.003$ is the NV$^-$ Landé factor [70, 55] and μ_B is the Bohr magneton. For ensembles, there are four different NV orientations and, provided that $g_{NV}\mu_B|B| \ll D$, only the projection of the magnetic field on the N-V axis affects the transition frequencies [121].

The zero-field Hamiltonian for the ground state, including hyperfine coupling to the ^{14}N nucleus (spin $I = 1$), can be written as:

$$\mathscr{H}_0 \approx DS_z^2 + E(S_x^2 - S_y^2) + A_{\|}S_zI_z + A_{\perp}(S_xI_x + S_yI_y), \tag{3.1}$$

where $A_{\|} = -2.1$ MHz and $A_{\perp} = -2.7$ MHz are, respectively, the axial and transverse hyperfine constants [55]. Analysis of this Hamiltonian reveals six allowed microwave transitions for each N-V orientation. The relative intensities can be calculated by treating the interaction with the microwave field, $\vec{B_1}$ as a perturbation, $\mathscr{H}_1 = g_{NV}\mu_B\vec{B_1} \cdot \vec{S}$, with matrix elements that depend on the alignment of the microwave radiation with respect to the symmetry and strain axes of each N-V center. However, since the exact geometry and the number of NV$^-$ centers of each orientation were not known *a priori*, Gaussian functions with variable amplitudes and equal widths, centered about these transition frequencies, were fit to the spectra. Including residual magnetic fields, measured by a commercial fluxgate magnetometer to be less than 1 G, into the model did not significantly influence the fits.

3.5 Results

Four single-crystal samples of mm-scale dimensions were studied, which were labeled S2, S3, S5, and S8 and characterized in Ref. [12]. Figure 3.1 shows the FDMR spectrum at 293 K for S3, a sample synthesized by chemical vapor deposition (CVD) with [NV$^-$]$^-$ $\approx$ 10 ppb [12]. As there was no applied magnetic field, the splitting between resonance peaks is due to non-zero E, induced by local strain [14, 189, 121]. This feature is present in varying magnitudes for all four samples. Even though all four NV orientations are present, the spectra are reasonably well-described by just six broad transitions, suggesting that the strain splittings are spatially inhomogenous [77, 190]. As no correlation with NV$^-$ concentration was observed (see Tab. 3.1), further work is necessary to determine the exact strain mechanism.

During each temperature scan, the spectrum was fit to an empirical function similar to the one described above, and the ZFS parameters were extracted. Figure 3.2(a) displays the spectra at two different temperatures for another sample, S8, a

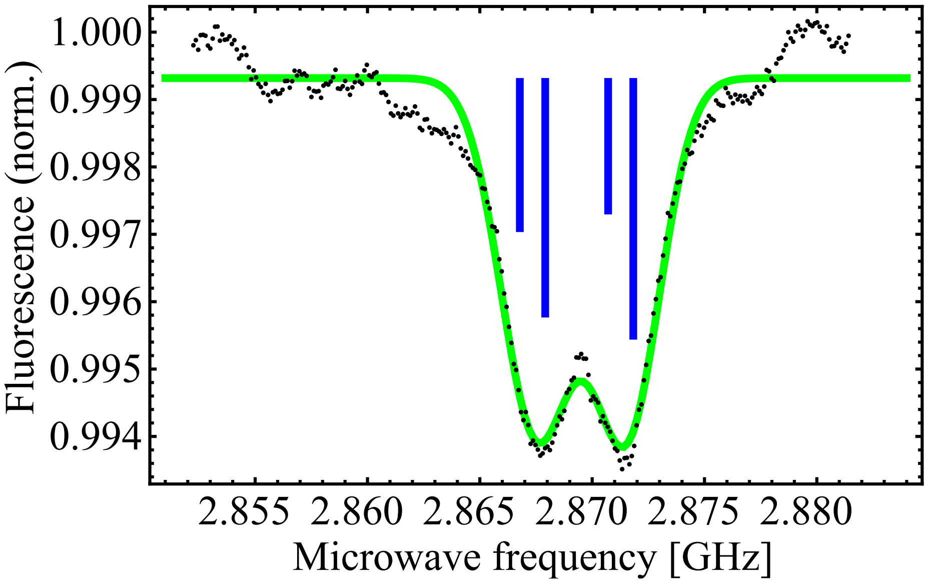

Figure 3.1: Zero-field FDMR spectrum at 293 K for S3 and the corresponding fit based on Eq. 3.1 (solid green line). The six blue lines represent the fitted amplitudes at each transition frequency, and the fitted linewidth was 3.3 MHz (full width at half maximum). The microwave power was reduced to ~ -10 dBm to resolve the hyperfine structure, resulting in the relatively small contrast of $\sim 0.6\%$. The best-fit parameters for this scan are $E = 1.4(5)$ MHz and $D = 2869.3(2)$ MHz.

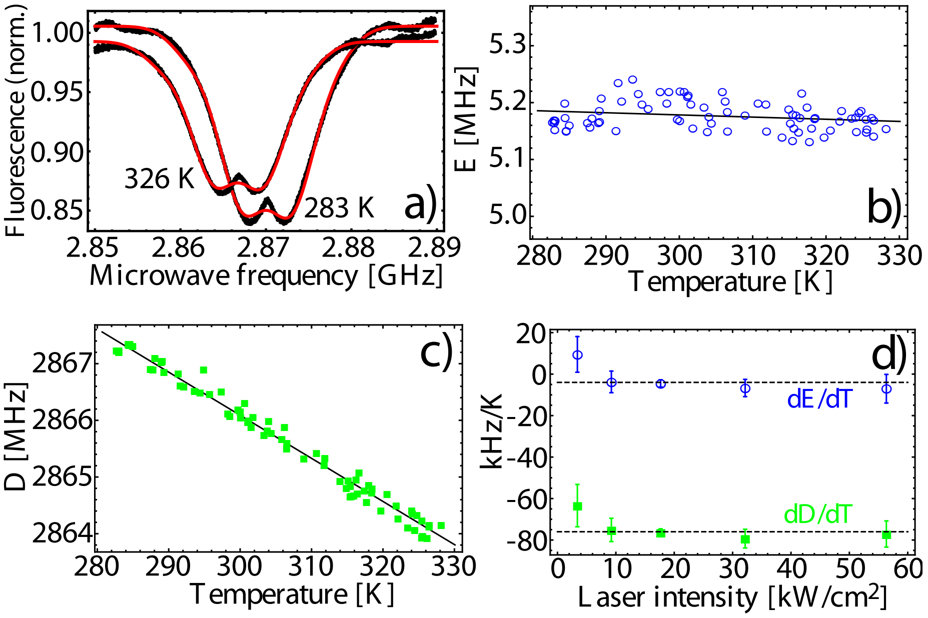

Figure 3.2: (a) Zero-field FDMR spectra at 283 K and 326 K for S8 with fits (solid red lines). (b) Value of E for S8 as a function of temperature with linear fit (solid black line). (c) D for S8 vs. temperature with linear fit. (d) dD/dT and dE/dT as a function of laser intensity for S5. The dotted lines are the laser-intensity-independent values used in Tab. 3.1.

high-pressure, high-temperature (HPHT) synthesized diamond with [NV$^-$] $\approx$ 0.3 ppm, as well as the empirical fits based on Eq. 3.1. Figures 3.2(b) and (c) show the ZFS parameters as a function of temperature for this sample. Linear least-squares fits yield $dE/dT = -0.4(2)$ kHz/K and $dD/dT = -76(1)$ kHz/K. Figure 3.2(d) displays the laser-intensity dependence for S5, an HPHT diamond with [NV$^-$] $\approx$ 12 ppm. Linear fits (not shown) determined that any dependence of dD/dT or dE/dT on laser intensity is not statistically significant. Additional tests for dependence on microwave power, external magnetic field, and sample positioning also did not show statistically significant effects.

A similar procedure was performed for the three other samples: S2, an HPHT diamond with [NV$^-$] $\approx$ 16 ppm, as well as S3 and S5 (already mentioned). Table 3.1 displays the temperature dependence of the ZFS parameters for each of these samples. The temperature dependence of D is similar for each sample, indicating that the mechanism responsible for this temperature variation is intrinsic to the NV centers themselves. Taking a weighted average over all samples gives $dD/dT = -75.0(6)$ kHz/K and, using the fitted room-temperature values for each sample ($D \approx 2869(1)$ MHz), this corresponds to a fractional temperature dependence of $dD/(DdT) = -2.61(2) \times 10^{-5}$ K^{-1}. The weighted average over samples of the fractional variation of E with temperature (final column of Tab. 3.1) is also statistically significant, $dE/(EdT) = -1.5(5) \times 10^{-4}$ K^{-1}, but further work is necessary to understand the nature of E.

#	[NV$^-$](ppm)	$\frac{dD}{dT}$(kHz/K)	E(MHz)	$\frac{1}{E}\frac{dE}{dT}(10^{-4}\text{K}^{-1})$
S2	16	$-71(1)$	2.7(6)	$-5(2)$
S3	0.01	$-74(4)$	1.4(5)	$-40(40)$
S5	12	$-78(1)$	8(1)	$-5(1)$
S8	0.3	$-76(1)$	2.6(4)	$-0.4(5)$

Table 3.1: ZFS parameters and uncertainties for four different samples. The values of E represent the expected value of E(293 K) extrapolated from the linear fits, and the error bars represent the standard error from the fit but not systematic effects due to imperfect assumptions in the model (see text). The laser intensity was $\sim$ 25-50 kW/cm^2 throughout the collection volume. Note that for the S2 spectra a magnetic field of $B_\perp \approx 13$ G was applied. This field enabled the isolation of a single NV orientation, and the simplified spectrum was used to verify the robustness of the model.

3.6 Calculation of D and its relative temperature dependence

The origin of D is expected to be predominately due to dipolar spin-spin coupling between the two unpaired electrons forming the center [70, 97, 122]. This suggests a a likely mechanism for the temperature variation is local lattice expansion. Assuming that the angular electronic wavefunctions are temperature-independent and that D is entirely due to dipolar coupling, the effect of lattice expansion on D is:

$$\frac{1}{D}\frac{dD}{dT} \approx \frac{1}{D}\frac{d\langle(r_{12}^2 - 3z_{12}^2)/r_{12}^5\rangle}{dR}\frac{dR}{dT}, \tag{3.2}$$

where r_{12} is the displacement between the two spins, z_{12} is the component of r_{12} along the N-V symmetry axis, and R is the distance between two basal carbon nuclei. The effect of thermal expansion on $\langle(r_{12}^2 - 3z_{12}^2)/r_{12}^5\rangle$ can be estimated by treating spins, localized near the basal carbon atoms [122, 10], with p-orbitals [122, 55] oriented along axes 110° apart [99], and calculating the integral for neighboring values of R. Using the room-temperature values for bulk diamond of $R = 0.252$ nm and $dR/dT = 2.52 \times 10^{-5}$ nm/K [18], we calculate $D = 2.66$ GHz, which is within 10% of the experimental value, and $dD/(DdT) = -5.8 \times 10^{-6}$ K^{-1}, which is about a factor of 4.5 smaller than the experimental value from this work. The latter discrepancy suggests that the macroscopic thermal expansion is not a good description of dR/dT in the immediate vicinity of the defect. *Ab initio* calculations [97, 99, 100, 10, 191] which include the determination of local thermal expansion effects would give a more accurate prediction of dD/dT.

3.7 Significance for magnetometry applications

The sharp temperature dependence of D presents a technical challenge for room-temperature diamond magnetometry. Even if the ambient temperature can be controlled at the 1-mK level, this would lead to fluctuations in the resonance frequency of 80 Hz corresponding to a magnetic-field variation of 3 nT. Monitoring both of the $\Delta m_s = \pm 1$ resonances could provide a feedback mechanism for controlling this effect for slow drifts, since the energy difference between these resonances does not depend on D.

Higher-frequency temperature fluctuations due to, for example, laser-intensity noise, present an additional complication for magnetometry in the high-density limit. Consider the case of a Ramsey-type magnetometer making use of repeated light pulses [13, 15, 14, 42] which transfer an energy to the diamond on the order of $E_p \approx \Delta\epsilon[\mathrm{NV}^-]V$, where $\Delta\epsilon \approx 0.6$ eV is the difference in energy between absorbed and radiated photons, V is the effective volume being heated, and we have conservatively neglected non-radiative transfer from the NV$^-$ singlet decay path [19] and other impurities [172]. If the pulses are separated in time by a precession window, τ, then in steady state the diamond temperature is modulated at a rate $\frac{dT}{dt} \approx \frac{E_p}{Vc\tau}$, where $c = 1.8$ J/cm^3/K is the volumetric specific heat of diamond [192]. Integration over the precession window yields a magnetometer offset of $B_{off} \approx \frac{\pi\Delta\epsilon[\mathrm{NV}^-]}{g_{NV}\mu_B c}\frac{dD}{dT} \approx -80$ nT at room temperature for $[\mathrm{NV}^-] = 1$ ppm. This offset makes the magnetometer sensitive to laser-pulse fluctuations. Uncorrelated, normally-distributed fluctuations in E_p by a fraction χ produce magnetic field noise-per-unit-bandwidth at the level of $\chi|B_{off}|/\sqrt{\tau} \approx 1$ pT/$\sqrt{\mathrm{Hz}}$, using $\chi = 0.01$ and $\tau = 1$ μs. We note that this magnetometer noise is directly correlated with laser-intensity noise and therefore monitoring the incident laser intensity could significantly reduce this effect.

3.8 Conclusion

In this work, we have measured the temperature dependence of the ZFS parameters of four diamond samples covering a wide range of NV$^-$ concentrations. We have found a significant variation of the axial ZFS, D, with temperature and surmise that it is due to local thermal expansion. We also present evidence of a non-zero transverse ZFS, E, and measure a small fractional temperature dependence just above the experimental uncertainty. The results have a major impact on the performance of NV-ensemble magnetometers and may ultimately limit their sensitivity and bandwidth. We expect that proper feedback mechanisms, such as monitoring laser intensity fluctuations and observing both $\Delta m_s = 1$ coherences simultaneously, will help to partially mitigate these effects.

The authors are grateful to A. Gali, C. Santori, P. Hemmer, F. Jelezko, E. Corsini, and O. Sushkov for valuable discussions and R. Folman for support. This work was supported by NSF grant PHY-0855552 and ONR-MURI.

3.9 Addendum

Recently [118] it was shown that D is strongly temperature dependent for the temperature range 280-330 K. It was shown that the experimental value of $D \approx$ 2.87 GHz could be theoretically accounted for by pure dipolar coupling between the unpaired electrons. However estimates for $dD/(Dd)T$ based on the thermal expansion coefficient of bulk diamond predicted a value that was $\sim$ 4.5 times smaller than the experimental value.

In order to gain further insight into the temperature dependence, we measured off-resonant zero-field ODMR spectra in visible fluorescence for a much wider temperature range, 5-400 K. The position of the dips were determined by quadratic fits and

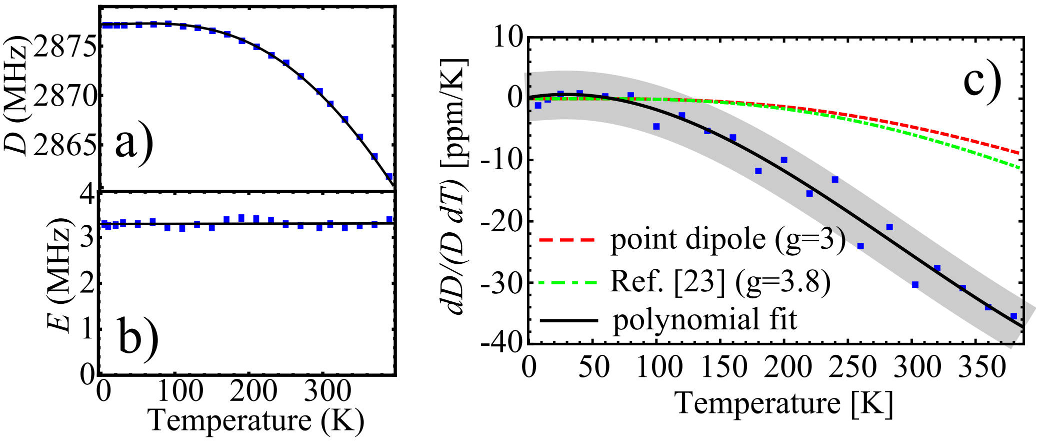

Figure 3.3: (a) Fitted value for D as a function of temperature. The microwave field amplitude was $\sim$ 3 mG and excitation was with $\sim$ 1 mW of 532 nm light for all data in (a)-(c). Error bars from the fits in (a)-(b) are smaller than the plotted points. (b) Fitted value of E as a function of temperature. (c) Fitted values of $dD/(DdT)$ as a function of temperature and theoretical temperature dependence based on macroscopic thermal expansion [18], as described in the text.

used to extract the ZFS parameters. Figures 3.3(b) and (c) show the temperature-dependence of the fitted values of D and E, respectively. We note that the room-temperature values for the ZFS parameters are shifted by $\sim$ 2 MHz from those for S2 in Ref. [118], and we attribute this discrepancy to an error in the fitting procedure in that work. However, upon re-analysis of the raw spectra in Ref. [118], the temperature dependence of both parameters, remained the same to within the quoted uncertainty.

No temperature dependence for E is evident from the data in Fig. 3.3(b), for example a fit to a line sets a limit of $dE/(EdT) < 30$ ppm/K. Figure 3.3(c) plots $dD/(DdT)$ as a function of temperature. These data were calculated by taking the derivative of nearest-lying points in Fig. 3.3(a). As seen in Fig. 3.3(c), the value measured for $dD/(DdT)$ is $-21(4)$ ppm/K at 283 K and $-28(3)$ ppm/K at 320 K. These values are in excellent agreement with Ref. [118], where $dD/(DdT) = -26.1(2)$ ppm/K in the temperature range 280-330 K was reported.

The solid and dashed lines in Fig. 3.3(c) come from assuming a form $dD/(DdT) = -g\alpha(T)/D$, where $\alpha(T)$ is the thermal expansion coefficient for bulk diamond [$\alpha(295\text{ K}) \approx$ 1 ppm/K, Ref. [18]] and g is a coefficient which describes the strength of the dipolar interaction. For a pure point-dipole interaction, $D \propto r^{-3}$, where r is the separation between unpaired electrons. Thus we expect $g = 3$ if r follows the same thermal expansion as bulk diamond. Assuming the unpaired electrons are confined to p-orbitals along the dangling bonds (see Ref. [118]), and that the positions of the dangling bonds follow the same thermal expansion as bulk diamond, we expect $g \approx 3.8$. A fit to a fifth order polynomial, consistent with the polynomial order used to fit the thermal expansion coefficient in Ref. [18], is shown in Fig. 3.3(c).

Chapter 4

Optical properties of the nitrogen-vacancy singlet levels in diamond

This chapter was previously published in Ref. [11] and is republished here, with minor changes, with permission.

4.1 Abstract

We report measurements of the optical properties of the 1042 nm transition of negatively-charged Nitrogen-Vacancy (NV) centers in type 1b diamond. The results indicate that the upper level of this transition couples to the $m_s = \pm 1$ sublevels of the ^3E excited state and is short-lived, with a lifetime of $\lesssim 1$ ns. The lower level is shown to have a temperature-dependent lifetime of 462(10) ns at 4.4 K and 219(3) ns at 295 K. The light-polarization dependence of 1042 nm absorption confirms that the transition is between orbitals of A_1 and E character. The results shed new light on the NV level structure and optical pumping mechanism.

4.2 Introduction

The negatively-charged Nitrogen-Vacancy (NV) center in diamond has received considerable attention in recent years for its unique optical and spin properties. The center has a paramagnetic ground state with long coherence times ($\gtrsim 1$ ms [42]), and spin levels can be initialized and detected by optical excitation in a broad range of wavelengths (450-650 nm) [112, 129, 122, 77] and manipulated on sub-nanosecond timescales [90] by microwave (MW) excitation, all at room temperature. These traits, coupled with the excellent thermal, electrical, and mechanical properties of

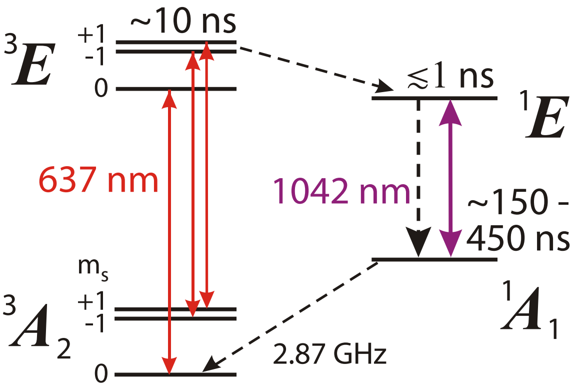

Figure 4.1: Level diagram for NV center showing spin-triplet ground and excited states, as well as the singlet system involved in intersystem crossing. Radiative transitions are indicated by solid arrows and non-radiative transitions by dashed arrows. The tentative label of the upper(lower) singlet as $^1E(^1A_1)$ is based on the observed spin-selective decay paths (see text).

the diamond host, make NV centers promising candidates for quantum computing [85, 86, 87, 88, 89, 92] and ultra-sensitive metrology [13, 14, 15, 12, 47, 54].

The NV center is now among the most widely studied defects in a solid [185], but there still exist open questions regarding its electronic level structure, and the mechanism by which optical excitation produces high spin polarization ($\gtrsim 80\%$ even at room temperature) [115, 55, 89] is not fully understood. The ordering and relative energies of all four singlet levels predicted by group theory [97] have not been experimentally verified, and current theories disagree [104, 101, 102]. Since some of these levels are responsible for the optical pumping mechanism of the NV center, a full characterization of their properties is necessary before applications can reach their full potential.

Recently an infrared (IR) zero-phonon line (ZPL) at $\sim$ 1042 nm was observed after optical excitation at 532 nm [19, 193]. The transition was characterized as a singlet-singlet transition involved in the optical pumping mechanism, but attempts to excite it on the phonon sideband were unsuccessful. In this chapter, we study the 1042 nm transition using laser light tuned to the ZPL. We determine the lifetimes of both singlet levels involved in the transition and infer their symmetry character from observed light-polarization selection rules. The results confirm the role of the transition in optical pumping of the center and give new information on the relative ordering and energies of the singlet levels.

Figure 4.1 depicts the energy level diagram of the NV center. Only experimentally verified levels are shown, though two additional singlet levels have been theoretically predicted [97, 104]. Transitions from the $^3A_2$ ground state to the ^3E state can be excited optically with ZPL at 637 nm. At least one singlet level lies close in energy

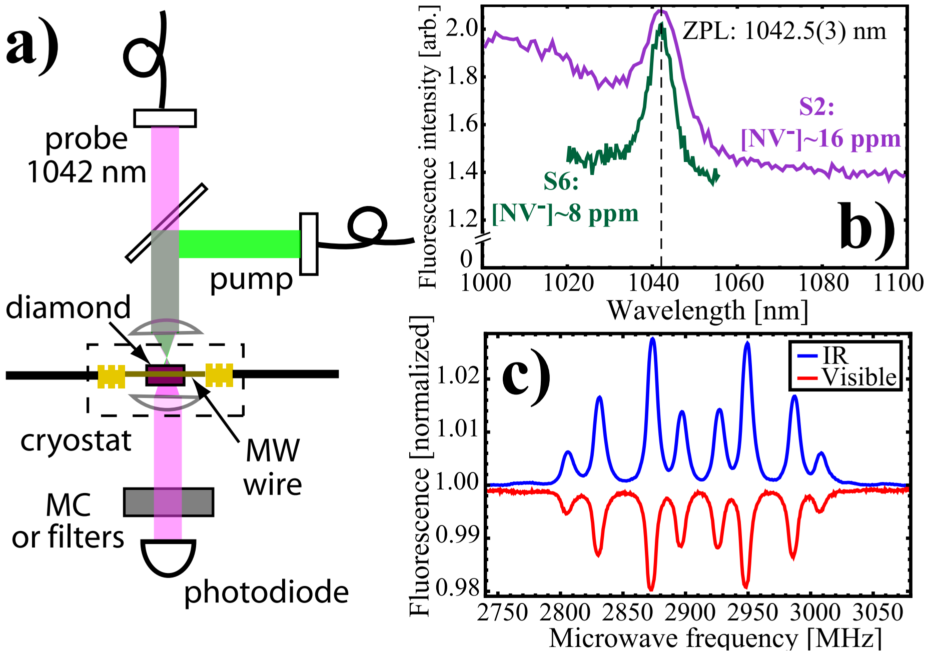

Figure 4.2: (a) Apparatus used for magnetic resonance and optical studies. MC–monochromator. (b) Fluorescence spectrum of the IR transition (excitation at 532 nm) at room temperature for two diamonds with different NV⁻ concentrations [12] showing a ZPL at 1042.5(3) nm. The sloped background is due to the tail of the phonon sideband of the much-stronger $^3E \rightarrow {}^3A_2$ transition [19]. (c) Magnetic-resonance spectra of sample S2 for visible (650-800 nm bandpass filter) and IR (1000 nm longpass filter) emission at room temperature under an applied field of $\sim$ 4 mT. Excitation was with $\sim$ 1 W of 532 nm light, polarized in the plane of the sample surface. The variation in peak heights can be explained by the pump-light and microwave polarization selection rules [20].

to ^3E, and spin-orbit coupling induces triplet-singlet intersystem crossing (ISC). NV centers in the $m_s = \pm 1$ magnetic sublevels have significantly higher probability to undergo ISC [122, 77], and, from symmetry considerations, this suggests that the closest lying singlet is ^1E [104, 194, 102]. NV centers which undergo ISC then decay to another, longer-lived singlet level [19] (ZPL at 1042 nm), after which they cross over predominately to the $m_s = 0$ sublevel of the $^3A_2$ ground state [104, 102]. Symmetry considerations predict that this metastable singlet (MS) is $^1A_1$ [104], but recent theoretical calculations [101, 9] contradict this assignment.

4.3 Experimental apparatus

Figure 4.2(a) illustrates the experimental apparatus used for optical characterization of the 1042 nm transition. Two laser beams, a pump (514, 532, or 637 nm) and IR probe ($\sim$ 10 mW at 1042.4 nm), were overlapped and focused with a 1/2"-focal-length lens onto the surface of a diamond housed in a liquid-helium cryostat (Janis ST-500). The temperature was measured by a diode located at the base of the cryostat's sample holder. The diamonds used in this work [12], grown under high-pressure-high-temperature conditions (HPHT), were irradiated with 3-MeV electrons and annealed at 750 C for two hours, after which they contain $\sim$ 8-16 ppm of NV$^-$ and $\sim$ 50 ppm of unconverted nitrogen. For absorption measurements, the transmission of the probe beam was spectrally filtered and detected with a Si photodiode. The same detection scheme was employed for fluorescence measurements, except the probe beam was blocked and different spectral filters were used, as appropriate. Figure 4.2(b) shows the room-temperature fluorescence spectra for two different high-NV-density HPHT samples, S2 and S6, recorded using a monochromator. For the samples and temperature range ($\sim$ 4.4-300 K) explored here, we measure the ZPL to be at 1042.5(3) nm. The IR emission is predominately concentrated in the ZPL [19], but the integrated intensity is less than visible emission (650-800 nm) by a factor of around 1000, presumably due to competition with a non-radiative decay process [19, 102].

4.4 Optical properties, spin-dynamics and temperature-dependent lifetimes

Here we describe measurements made on S2. Figure 4.2(c) shows room-temperature magnetic-resonance spectra detected in visible and IR emission with a 532 nm pump beam. These spectra can be understood as follows. Optical pumping collects NV centers in the $m_s = 0$ ground-state sublevel. When the frequency of an applied MW field coincides with one of the eight ground-state magnetic-resonance transition frequencies (see, for example, Refs. [20, 12, 121, 47, 54, 118]), population is transferred to an $m_s = \pm 1$ sublevel. Under continuous optical excitation, this results in more NV centers undergoing ISC to the singlet levels, resulting in a decrease in visible fluorescence and an increase in IR fluorescence. Due to a combination of background fluorescence from the phonon sideband of the $^3E \rightarrow {}^3A_2$ transition, imperfect spin polarization, and non-zero branching ratio from $m_s = 0$, the contrast of the IR fluorescence magnetic-resonance spectra is only a few percent.

To verify the model in Fig. 4.1, wherein the upper singlet is populated indirectly by decay from the $m_s = \pm 1$ sublevels of ^3E, we observed, via fluorescence, magnetic resonance spectra while pumping resonantly (637 nm) and non-resonantly (514 nm) at 70 K. The pump intensities were kept relatively low ($\lesssim$ 1 kW/cm^2) in order to minimize bleaching [195, 142]. Under both pumping conditions, we found that the intensity ratio of visible emission (650-800 nm) to infrared emission (1000+ nm) was the same ($3(1) \times 10^3$), confirming that the upper singlet is populated via the ^3E. Further, the shape and contrast of the IR fluorescence spectra were similar under both pumping conditions, indicating that decay is primarily from the $m_s = \pm 1$ sublevels.

In order to determine lifetimes of the upper singlet and ^3E excited state, fluorescence lifetime measurements were carried out for both the IR and visible emission using the phase-shift technique [196] (Fig. 4.3(a)). When the intensity of the pump beam is modulated sinusoidally with frequency f, the time-dependent fluorescence oscillates with a relative phase shift, ϕ. For decay described by a single time-constant, τ, which was used to model the visible emission [197], this phase shift is $\phi = \arctan(2\pi f \tau)$. For the cascade decay expected for IR fluorescence (Fig. 4.1), we assume that the upper singlet level (lifetime, τ_0) is populated only by the $m_s = \pm 1$ sublevels in ^3E (lifetime, $\tau_1 \approx 7.8$ ns [153]), and find $\phi = \arctan(\frac{2\pi f(\tau_1+\tau_0)}{1-(2\pi f)^2 \tau_1 \tau_0})$.

Figure 4.3(b) shows results of the lifetime measurements at zero magnetic field for visible and IR emission, respectively. The pump (514 nm) modulation-frequency was varied and both the pump and fluorescence intensities were simultaneously recorded on separate detectors. The relative phase was determined by fitting both signals and correcting for time delays due to the detection scheme. For visible emission, the ensemble-averaged decay time is found to be 10.0(3) ns. For IR emission, the fitted lifetime of the upper singlet is $\tau_0 = 0.9(5)$ ns, which is consistent with the decay being dominated by a non-radiative channel [19]. No temperature dependence was observed for either visible or IR fluorescence lifetimes in the range explored here (4.4-70 K).

The lifetime of the MS level was measured by recording the transmission of 1042.4 nm light after abruptly turning the pump beam off (fall time $\lesssim 20$ ns), and fitting to a single exponential. Laser-intensity-dependent effects were determined to be smaller than the statistical uncertainty by varying both pump and probe laser powers. Figure 4.3(c) shows the lifetime as a function of temperature, along with fits to the model described below. A substantial temperature dependence is observed; the MS lifetime is determined to be 462(10) ns at 4.4 K and decreases to 219(3) ns at 295 K and 142(6) ns at 450 K. The timescale of this decay is in agreement with the observed timescale for ISC to the ground state [185, 104], confirming that the lower-energy level of the 1042 nm transition is indeed the metastable state which governs spin dynamics under optical excitation.

As the spontaneous emission rate is independent of temperature, a likely mechanism for temperature-dependent decay is emission stimulated by lattice phonons. Assuming a simple model where decay is dominated by a single channel, the temperature-dependent rate for the N-phonon decay is then given by [198]:

$$\frac{1}{\tau[T]} = \frac{1}{\tau[0]} \prod_{i=1}^{N} (1 + n_i[T]), \tag{4.1}$$

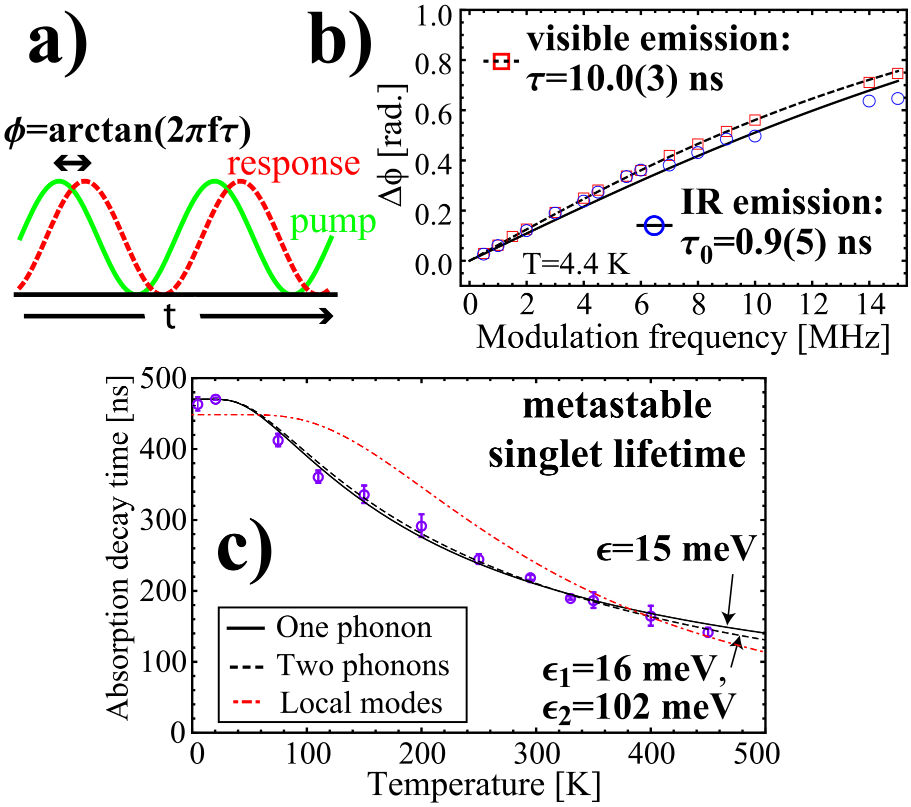

Figure 4.3: (a) The phase shift technique. (b) Phase shift of visible (650-800 nm) and IR (1035-1045 nm) fluorescence as a function of modulation frequency and fits (see text). (c) Lifetime of the MS as a function of temperature as well as fits to Eq. (4.1). The values of ϵ and $\epsilon_{1,2}$ are the fitted phonon energies for $N = 1$ and $N = 2$ decays, respectively. Error bars represent the standard deviation of multiple measurements.

where $n_i[T] = (e^{\epsilon_i/(k_\mathrm{B}T)} - 1)^{-1}$ is the Bose occupancy for the phonon mode with energy ϵ_i, and k_B is the Boltzmann constant. Figure 4.3(c) shows fits of Eq. (4.1) for $N = 1$ and 2. The fit parameters indicate that the total energy gap between the MS and final state, $\sum_i \epsilon_i$, is 15(1) meV for $N = 1$ and 118(30) meV for $N = 2$. We also fit the data to the dominant local phonon modes [19], modifying Eq. (4.1) as $1/\tau[T] = 1/\tau[0]\prod_{i=1}^{2}(1 + n_i[T])^{N[\epsilon_i]}$, where $\epsilon_i = \{43, 137\}$ meV are the phonon energies, and $N[\epsilon_i]$ are the respective degeneracies. While the fit is not as good, it suggests a similarly small energy gap of 129 meV (N[43 meV] = 3 and N[137 meV] = 0). Such a small energy gap is not predicted by current models, where the MS is expected to lie ~ 700 meV above the ${}^3A_2$ ground state [19, 101, 102], so further work is necessary to resolve this.

In order to determine the orbital character of the two singlets, we studied the light-polarization selection rules for excitation. A magnetic field was applied which split the resonances belonging to each orientation, allowing us to observe the optical response of each NV orientation (Fig. 4.4(a)). We modified the apparatus illustrated in Fig. 4.2(a), inserting separate linear polarizers for both resonant pump (637.7 nm) and probe (1042.4 nm) beams. Figure 4.4(b) shows the light-polarization-dependence of the magnetic-resonance contrast under two geometric configurations; where the NV axis, $\mathbf{z}$, was normal to or lying in the plane of polarization, defined by the normal vector, $\hat{\mathbf{k}}$. For $\mathbf{z} \parallel \hat{\mathbf{k}}$, the contrast of visible fluorescence, R_{vis}, is independent of pump polarization angle, and for $\mathbf{z} \perp \hat{\mathbf{k}}$, R_{vis} approaches zero for polarization along $\mathbf{z}$. This behavior is consistent with the expected polarization selection rules for a $E \leftrightarrow A_2$ transition [199, 20, 200], where excitation with $\mathbf{x}$ and $\mathbf{y}$ polarized light is equally allowed and $\mathbf{z}$ polarization is forbidden. With pump polarization now held constant at an angle which excited all orientations, we observed the contrast of IR absorption, R_{ir}, with varying probe polarization. The results demonstrate that R_{ir} has a similar polarization dependence to R_{vis}, indicating that both transitions obey the same polarization selection rules. This observation confirms that the 1042 nm transition involves E and A_1 orbitals, as the other possible combinations of singlet levels have different polarization selection rules [21] (Fig. 4.4(c)).

4.5 Conclusion

We have measured optical properties of the 1042 nm transition of the NV center and determined that the transition plays an important role in the optical pumping mechanism. This knowledge can be used to improve NV-based applications; for example, 1042 nm absorption was recently used in a magnetometer which demonstrated about an order of magnitude improvement in sensitivity compared to fluorescence-based techniques [44]. Further work is necessary to determine the relative energies of all four singlet levels and to understand the role of non-radiative decay.

The authors are grateful to A. Gali, N. Manson, L. Rogers, M. Doherty, P. Hem-

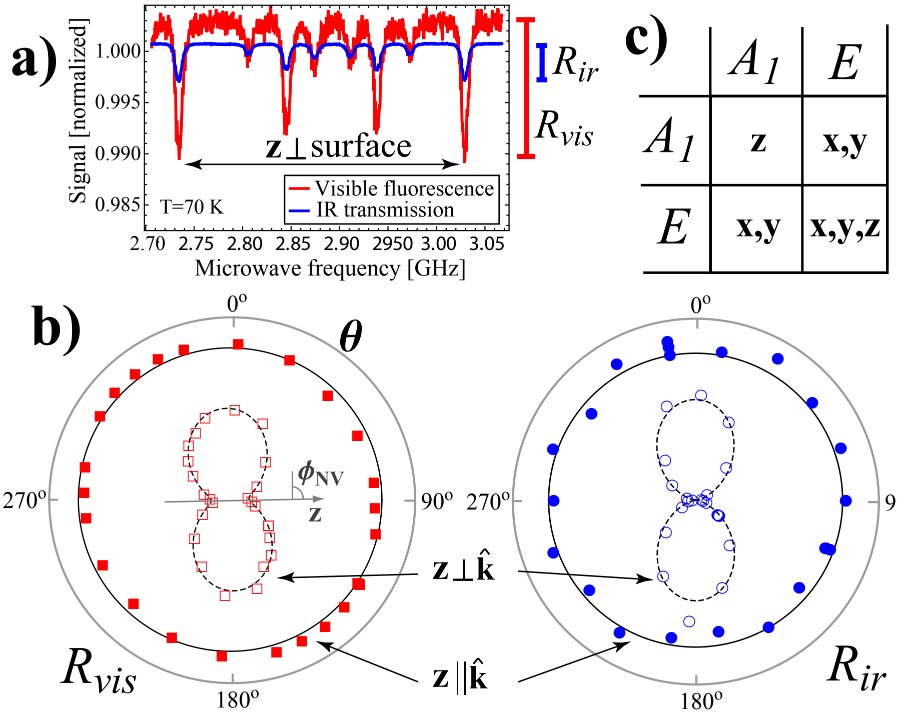

	A_1	E
A_1	**z**	**x,y**
E	**x,y**	**x,y,z**

Figure 4.4: (a) Example magnetic-resonance spectrum for visible fluorescence and transmission of IR probe at 70 K. As the sample was [111]-oriented, one of the NV axes was normal to the sample surface. (b) Polar plot of the contrast of visible fluorescence (left) and IR absorption (right) as a function of light-polarization angle for both geometries (see text). Solid lines are fits to a constant and dashed lines are fits to $\sin^2(\theta - \phi_{NV}) + c$, where θ is the polarizer angle, ϕ_{NV} is the angle of $\mathbf{z}$ relative to the polarizer axis, and c is an offset which takes into account imperfections in light polarization, beam alignment, and selection rules. For the $\mathbf{z} \perp \hat{\mathbf{k}}$ geometry, the sample and polarizer were positioned such that we expected $\phi_{NV} = 90(3)°$, and both of the fitted values of ϕ_{NV} agree with this value to within the uncertainty. (c) Light-polarization axes for allowed transitions between the singlet levels [21]. The selection rules are identical for both absorption and emission.

mer, E. Corsini, B. Patton, M. Ledbetter, and L. Zipp for valuable discussions. This work was supported by NSF grant PHY-0855552.

Chapter 5

Broadband magnetometry by infrared-absorption detection of diamond NV centers

This chapter was previously published in Ref. [44] and is republished here, with minor changes, with permission.

5.1 Abstract

We demonstrate magnetometry by detection of the spin state of high-density nitrogen-vacancy (NV) ensembles in diamond using optical absorption at 1042 nm. With this technique, measurement contrast and collection efficiency can approach unity, leading to an increase in magnetic sensitivity compared to the more common method of collecting red fluorescence. Working at 75 K with a sensor with effective volume $50 \times 50 \times 300\ \mu\text{m}^3$, we project photon shot-noise limited sensitivity of 5 pT in one second of acquisition and bandwidth from DC to a few MHz. Operation in a gradiometer configuration yields a noise floor of 7 nT_{rms} at $\sim$ 110 Hz in one second of acquisition.

5.2 Introduction

Recently, a technique for measuring magnetic fields at the micro- and nanometer scale has emerged based on nitrogen-vacancy (NV) electron spin resonances in diamond [14, 15]. This technique offers an exceptional combination of sensitivity and spatial resolution in a wide temperature range, from 0 K to above room temperature. Sensors employing ensembles of NV centers promise the highest sensitivity [13, 12] and have recently been demonstrated [48, 54, 47]. These first-generation magnetometers have measured sub-micron-scale fields, but their sensitivity was limited by background fluorescence and poor photon collection efficiency.

In this Chapter, we demonstrate a technique to read out the NV spin state using infrared (IR) absorption at 1042 nm [19, 11]. With this technique, measurement contrast and collection efficiency can approach unity, leading to an overall increase in magnetic sensitivity. We perform measurements at 45-75 K on a sensor with active volume $\sim 50\times50\times300\ \mu\text{m}^3$, revealing magnetic resonances with amplitude and width corresponding to a shot-noise-limited sensitivity of 5 pT in one second of acquisition and a measurement bandwidth from DC up to a few MHz. We demonstrate operation in a gradiometer configuration, with a sensitivity of 7 nT_{rms} in one second of acquisition at $\sim$ 110 Hz bandwidth, and outline a design for a room-temperature device employing a low-finesse optical cavity with sensitivity approaching the spin-projection noise limit.

5.3 Fundamental limits on sensitivity

Spin-based magnetometers are fundamentally limited by the quantum noise associated with spin projection. The minimum detectable magnetic field for a sample of spins with density n in a volume V is given by [7, 13]:

$$\delta B_q \simeq \frac{1}{\gamma}\frac{1}{\sqrt{nVt_mT_2^*}}, \tag{5.1}$$

where $\gamma = 1.761\times10^{11}\ \text{s}^{-1}\text{T}^{-1}$ is the NV gyromagnetic ratio [70] and T_2^* is the electron spin dephasing time, and $t_m \gtrsim T_2^*$ is the measurement time. The sample [12] used in this work (labeled S2), contains an NV density of $n = 7\times10^{17}\ \text{cm}^{-3}$ for each of the four crystallographic orientations and typically exhibits $T_2^* = 0.15\ \mu$s. With optimal detection the magnetic sensitivity approaches the limit set by Eq. (5.1), and we find the noise floor in this sample of $\sim 20\ \text{pT}/\mu\text{m}^{3/2}$ for $t_m = 1$ s, or $\sim$ 10 fT for the active volume used here.

However, reaching this level of sensitivity requires an improvement over the commonly used technique of detecting spin selective fluorescence [72, 185]. For sufficiently low measurement contrast, R (relative difference in detected signal depending on spin-projection), the sensitivity using the fluorescence technique can be estimated [13, 12] by modifying Eq. (5.1) as $\delta B_{fl} \approx \delta B_q/(R\sqrt{\eta})$, where η is the detection efficiency. Recent experiments [54, 47] yielded typical values of $R \sim 0.03$ and $\eta \sim 0.001$, making the best possible sensitivity, in the absence of excess technical noise or other broadening mechanisms, about three orders of magnitude worse than the spin-projection-noise limit. The contrast is limited by non-ideal branching ratios to the dark singlet states [104, 19] and high background fluorescence from defects which do not contribute to the magnetometer signal [20], while η is limited by the field of view of the detection optics and sub-unity quantum efficiency of the detected transition [142, 52].

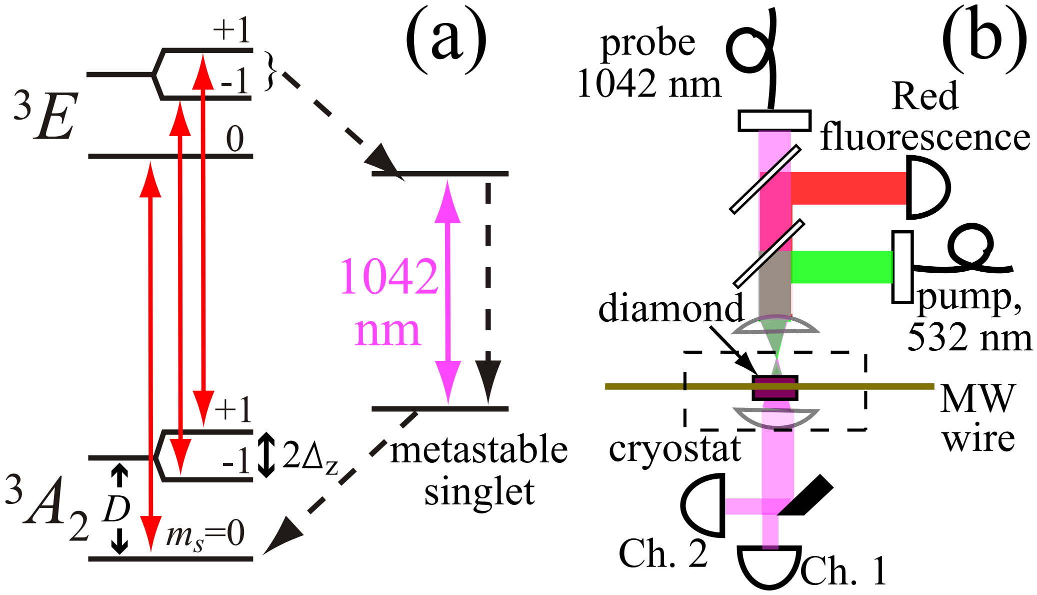

Figure 5.1: (a) Level structure of the NV center and allowed optical transitions. Radiative (non-radiative) transitions are represented by solid (dashed) lines. (b) IR absorption gradiometer apparatus. The green pump and IR probe beams were focused to a diameter of ~ 30 μm near the surface of the diamond, and two halves of the transmitted IR beam were detected with separate photodiodes. MW–microwave.

5.4 Infrared absorption technique

By using IR absorption detection, we circumvent most of these problems and achieve considerably higher sensitivity. Figure 5.1(a) displays the level structure of the NV center with allowed radiative and non-radiative transitions. The center has a paramagnetic ($S = 1$) ground state, with a zero-field splitting of $D \approx 2.87$ GHz at room-temperature [118]. At low magnetic field ($<< 0.1$ T), the magnetic sublevels shift by $\Delta_z \approx \gamma m_s B_z/(2\pi)$, where B_z is the projection of the magnetic field along the NV axis. Optical pumping via a spin-selective decay path [104, 19, 11] involving a 1042 nm transition, populates NV centers in the $m_s = 0$ ground-state sublevel. The same decay path is also responsible for the drop in fluorescence upon application of resonant microwaves, which is the principle of operation of recent magnetometry demonstrations [14, 15, 42, 48, 47, 54].

The apparatus is illustrated in Fig. 5.1(b). Pump (532 nm) and probe (1042 nm) beams were overlapped and focused to a waist of ~ 30 μm diameter, approximately 0.5 mm before the diamond surface. The diverging beam had a diameter of ~ 50 μm as it passed through the diamond, and was sufficiently far from the focal point (more than one Rayleigh range) that it exhibited far-field diffraction. Fluorescence was collected via the same lens, spectrally filtered to pass 650-800 nm light, and detected

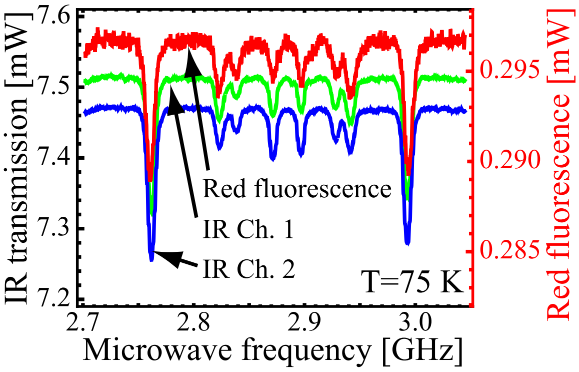

Figure 5.2: Optically-detected magnetic resonance at 75 K using the fluorescence method and both halves of the transmitted IR probe. The pump power was 0.8 W and the microwave Rabi frequency was ∼ 1.5 MHz.

by a photodiode. The transmitted probe beam was split in two halves by a sharp-edge mirror and detected with separate photodiodes. The diamond was housed in a liquid-helium cryostat (Janis ST-500) and microwaves were delivered via a wire placed ∼ 2 mm from the illuminated region. No magnetic shielding was used.

The principle behind our technique is the following: under continuous optical pumping, we detect the population of NV centers in the metastable singlet (MS) by monitoring the transmission of the 1042 nm probe beam and use this to read out the spin polarization of the ensemble. In the absence of resonant microwaves, NV centers are pumped into the $m_s = 0$ ground-state sublevel and there is reduced population in the MS corresponding to maximum probe transmission. Under application of microwaves with frequency $D \pm \gamma B_{z_i}/(2\pi)$, where B_{z_i} is the magnetic field projection along the i'th NV orientation, population is transferred to the $m_s = \pm 1$ sublevel, resulting in greater population in the MS and lower probe transmission.

Magnetic-resonance spectra, detected by both fluorescence and IR-transmission, are shown in Fig. 5.2. A bias magnetic field of ∼ 4 mT, produced by a permanent magnet, was directed such that each of the four NV orientations had different B_{z_i}, resulting in eight resolved resonances. The contrast of both fluorescence and IR-transmission resonances depends on the change in the MS population, which saturates when the pump rate is $\Omega_p \gtrsim 1/\tau_{MS}$, where $\tau_{MS} \approx 0.3$ μs is the MS lifetime [11]. This condition was satisfied without significant power broadening for the pump power used here, 0.8 W.

For the IR-transmission resonances, the contrast also depends on the probe's optical depth. At room temperature, we find $R \sim 0.003$, limited by the weak oscillator strength of the transition [19, 11] and homogenous broadening of the IR absorption line [19, 11]. The maximum contrast ($R \sim 0.03$) occurs in the 45-75 K temperature range, where the homogenous and inhomogenous contributions to the linewidth are approximately equal [108]. This contrast is, coincidentally, nearly the same as the maximum contrast obtained using fluorescence detection, but the signal is much larger due to the higher collected light intensity.

5.5 Operation as a magnetic gradiometer

Operation of the device as a magnetometer was accomplished by phase-sensitive detection. An oscillating magnetic field (frequency 40 kHz, amplitude ~ 0.1 mT) was applied and the resulting photodiode signals were demodulated at the first harmonic using lock-in electronics. In order to maximize the contrast, we used the $\Delta m_s = -1$ resonance corresponding to NV orientation normal to the light polarization vectors [20, 11]. Lock-in signals as a function of microwave frequency are shown in Fig. 5.3(a) for both IR channels. The small difference in magnetic response of the two channels, due to inhomogeneity in the pump and microwave fields, was compensated for by adjusting the light levels hitting the photodiodes.

Tuning the microwaves to the center of the resonance, where the lock-in signal crosses zero, gave the highest magnetic response. Figure 5.3(b) shows the time-series response of both magnetometer channels when an additional AC magnetic field (frequency 109 Hz, amplitude 1 $\mu\mathrm{T}_{\mathrm{rms}}$) was applied. The magnetometer was also operated at 26 and 426 Hz with a similar magnetic response. The measurement bandwidth in this work was limited by the lock-in time constant, but in principle this technique can be used to detect fields with angular frequency approaching the maximum spin polarization rate, $\sim 1/\tau_{MS}$, without degradation in sensitivity.

The Fourier transform of the time-series response for the 109 Hz applied field, Fig. 5.3(c), reveals a noise floor for each channel of ~ 15 $\mathrm{nT}_{\mathrm{rms}}$ in 1 s of acquisition for $\sim$ 110 Hz frequencies. For comparison, we also plot the noise spectrum for fluorescence-based magnetometer at room temperature, showing a noise floor of ~ 60 $\mathrm{nT}_{\mathrm{rms}}$ in 1 s of acquisition.

Taking the difference of the two IR channels' magnetometer signals gives a noise floor of ~ 7 $\mathrm{nT}_{\mathrm{rms}}$ in 1 s of acquisition for ~ 110 Hz frequencies. Since these signals correspond to light that has interacted with spatially separate parts of the diamond, the difference-signal measures the magnetic field gradient across the beam (effective baseline ~ 25 μm). The benefit of this gradiometric approach is that technical noise common to both channels, such as laser intensity and ambient field fluctuations, is canceled. The cancelation here was imperfect, as the dominant contributions to the noise floor were uncompensated intensity fluctuations of both pump and probe lasers, as determined by blocking the pump laser and/or turning off the modulation field.

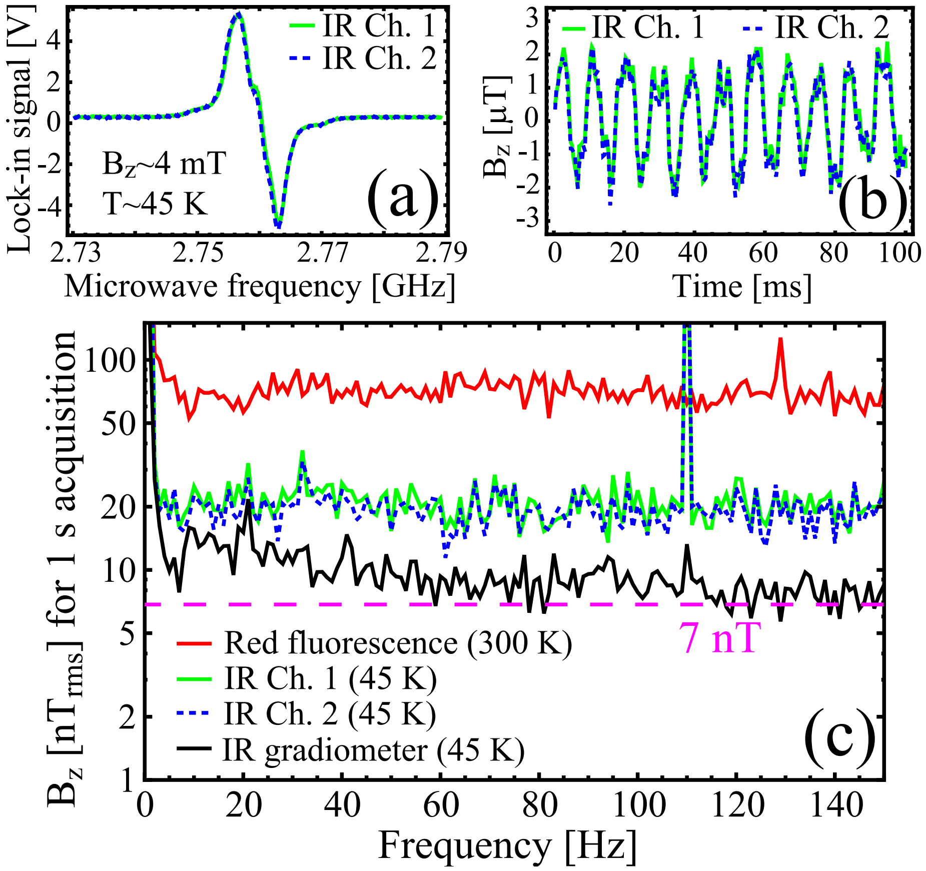

Figure 5.3: (a) Lock-in signal for both IR magnetometer channels. (b) Time series magnetometer signal, after subtraction of the static bias field, for a 1 μT_{rms} applied field at 109 Hz. The microwave frequency was tuned to the center of the resonance (zero-crossing in (a)). (c) Frequency-domain response of the magnetometer output in (b) revealing an IR absorption gradiometer noise floor of 7 nT_{rms} in 1 s of acquisition.

5.6 Eliminating photon shot-noise

In the absence of technical noise, our technique is limited by photon shot-noise, given by:

$$\delta B_p \simeq \frac{1}{\gamma}\frac{\Gamma_{mr}}{R}\sqrt{\frac{E_p}{P t_m}}, \tag{5.2}$$

where Γ_{mr} is the magnetic-resonance linewidth, E_p is the photon energy, and P is the detected optical power. Analyzing the highest-contrast resonances in Fig. 5.2, we project a photon shot-noise limited sensitivity of $\sim$ 40 pT for fluorescence collection and $\sim$ 5 pT for the sum of both IR absorption channels at $t_m = 1$ s. The latter corresponds to approximately an order of magnitude better sensitivity-per-root-volume than the photon shot-noise limit of recent fluorescence-based demonstrations [47, 54].

Here we were limited by the available laser diode power, but if the 1042 nm transition is closed, we may be able to increase the probe power without adverse effects, making the photon shot-noise negligibly low, and leaving only the quantum-shot-noise-limited sensitivity. In this case, the number of NV centers that enters Eq. (5.1) would be the change in the MS population on and off resonance.

5.7 Conclusion

The present technique can be extended to room-temperature operation by employing a cavity to increase the optical depth at 1042 nm. We estimate that a cavity with finesse of $\sim$ 200 will optimize the magnetometer response. Using two parallel micro-cavities should permit gradiometry with sensitivity approaching the quantum shot-noise limit of $\sim$ 10 fT in one second of acquisition. Such a device would be ideal for low-field NMR detection [26] in, for example, microfluidic devices [25].

The authors thank B. Patton, E. Corsini, and the group of A. Pines for helpful comments. This work was supported by NSF.

Chapter 6

Conclusion

In this dissertation, the basic history and physics behind optical magnetometry with nitrogen vacancy centers in diamond was discussed. The focus was on high-spin-density ensembles for ultra-sensitive, high-bandwidth, variable-temperature magnetometry at the micrometer scale. First we identified important parameters in the fabrication process and showed how to produce optimized material for ensemble magnetometry. Next we studied the temperature dependence of the ground-state magnetic resonance and discussed its impact on the performance of ultra-sensitive devices. Then we discussed optical properties of a singlet-singlet transition and showed that this transition can be used for high sensitivity spin-state readout. Finally we presented a magnetometer prototype which incorporated ideas learned from these basic studies and improved on the state-of-the-art in several key areas.

Bibliography

[1] W. C. Griffith, S. Knappe, and J. Kitching, Opt. Express **18**, 27167 (2010).

[2] H. B. Dang, A. C. Maloof, and M. V. Romalis, Applied Physics Letters **97**, 151110 (2010).

[3] M. Vengalattore, J. M. Higbie, S. R. Leslie, J. Guzman, L. E. Sadler, and D. M. Stamper-Kurn, Physical Review Letters **98**, (2007).

[4] J. R. Kirtley, M. B. Ketchen, K. G. Stawiasz, J. Z. Sun, W. J. Gallagher, S. H. Blanton, and S. J. Wind, Applied Physics Letters **66**, 1138 (1995).

[5] A. Finkler, Y. Segev, Y. Myasoedov, M. L. Rappaport, L. Ne'eman, D. Vasyukov, E. Zeldov, M. E. Huber, J. Martin, and A. Yacoby, Nano Letters **10**, 1046 (2010).

[6] H. J. Mamin, T. H. Oosterkamp, M. Poggio, C. L. Degen, C. T. Rettner, and D. Rugar, Nano Letters **9**, 3020 (2009).

[7] D. Budker and M. Romalis, Nature Physics **3**, 227 (2007).

[8] J. Clarke and A. I. Braginski, *The SQUID Handbook* (Wiley-VCH, Weinheim, 2004), Vol. 1.

[9] M. W. Doherty, N. B. Manson, P. Delaney, and L. C. L. Hollenberg, New Journal of Physics **13**, 025019 (2011).

[10] A. Gali, M. Fyta, and E. Kaxiras, Physical Review B **77**, (2008).

[11] V. M. Acosta, A. Jarmola, E. Bauch, and D. Budker, Physical Review B **82**, 201202 (2010).

[12] V. M. Acosta, E. Bauch, M. P. Ledbetter, C. Santori, K. M. C. Fu, P. E. Barclay, R. G. Beausoleil, H. Linget, J. F. Roch, F. Treussart, S. Chemerisov, W. Gawlik, and D. Budker, Physical Review B **80**, 115202 (2009).

[13] J. M. Taylor, P. Cappellaro, L. Childress, L. Jiang, D. Budker, P. R. Hemmer, A. Yacoby, R. Walsworth, and M. D. Lukin, Nat Phys **4**, 810 (2008).

[14] G. Balasubramanian, I. Y. Chan, R. Kolesov, M. Al-Hmoud, J. Tisler, C. Shin, C. Kim, A. Wojcik, P. R. Hemmer, A. Krueger, T. Hanke, A. Leitenstorfer, R. Bratschitsch, F. Jelezko, and J. Wrachtrup, Nature **455**, 648 (2008).

[15] J. R. Maze, P. L. Stanwix, J. S. Hodges, S. Hong, J. M. Taylor, P. Cappellaro, L. Jiang, M. V. G. Dutt, E. Togan, A. S. Zibrov, A. Yacoby, R. L. Walsworth, and M. D. Lukin, Nature **455**, 644 (2008).

[16] A. M. Zaitsev, *Optical Poperties of Diamond: A Data Handbook* (Springer-Verlag, Berlin Heidelberg, 2001).

[17] J. R. Rabeau, P. Reichart, G. Tamanyan, D. N. Jamieson, S. Prawer, F. Jelezko, T. Gaebel, I. Popa, M. Domhan, and J. Wrachtrup, Applied Physics Letters **88**, 023113 (2006).

[18] T. Sato, K. Ohashi, T. Sudoh, K. Haruna, and H. Maeta, Physical Review B **65**, 092102 (2002).

[19] L. G. Rogers, S. Armstrong, M. J. Sellars, and N. B. Manson, New Journal of Physics **10**, 103024 (2008).

[20] T. P. M. Alegre, C. Santori, G. Medeiros-Ribeiro, and R. G. Beausoleil, Physical Review B **76**, 165205 (2007).

[21] M. S. Dresselhaus, G. Dresselhaus, and A. Jorio, *Group theory: Applications to the physics of condensed matter* (Springer, Heidelberg, 2008).

[22] V. V. Yashchuk, J. Granwehr, D. F. Kimball, S. M. Rochester, A. H. Trabesinger, J. T. Urban, D. Budker, and A. Pines, Physical Review Letters **93**, 160801 (2004).

[23] S. J. Xu, V. V. Yashchuk, M. H. Donaldson, S. M. Rochester, D. Budker, and A. Pines, Proceedings of the National Academy of Sciences of the United States of America **103**, 12668 (2006).

[24] H. Xia, A. B. A. Baranga, D. Hoffman, and M. V. Romalis, Applied Physics Letters **89**, (2006).

[25] M. P. Ledbetter, I. M. Savukov, D. Budker, V. Shah, S. Knappe, J. Kitching, D. J. Michalak, S. Xu, and A. Pines, Proceedings of the National Academy of Sciences of the United States of America **105**, 2286 (2008).

[26] M. P. Ledbetter, C. W. Crawford, A. Pines, D. E. Wemmer, S. Knappe, J. Kitching, and D. Budker, Journal of Magnetic Resonance **199**, 25 (2009).

[27] S. A. Murthy, D. Krause, Z. L. Li, and L. R. Hunter, Physical Review Letters **63**, 965 (1989).

[28] C. J. Berglund, L. R. Hunter, D. Krause, E. O. Prigge, M. S. Ronfeldt, and S. K. Lamoreaux, Physical Review Letters **75**, 1879 (1995).

[29] J. M. Brown, S. J. Smullin, T. W. Kornack, and M. V. Romalis, Physical Review Letters **105**, 151604 (2010).

[30] A. N. Youdin, D. Krause, K. Jagannathan, L. R. Hunter, and S. K. Lamoreaux, Physical Review Letters **77**, 2170 (1996).

[31] V. Acosta, M. P. Ledbetter, S. M. Rochester, D. Budker, D. F. J. Kimball, D. C. Hovde, W. Gawlik, S. Pustelny, J. Zachorowski, and V. V. Yashchuk, Physical Review A **73**, 053404 (2006).

[32] V. M. Acosta, M. Auzinsh, W. Gawlik, P. Grisins, J. M. Higbie, D. F. J. Kimball, L. Krzemien, M. P. Ledbetter, S. Pustelny, S. M. Rochester, V. V. Yashchuk, and D. Budker, Optics Express **16**, 11423 (2008).

[33] M. P. Ledbetter, V. M. Acosta, S. M. Rochester, D. Budker, S. Pustelny, and V. V. Yashchuk, Physical Review A (Atomic, Molecular, and Optical Physics) **75**, 023405 (2007).

[34] M. P. Ledbetter, I. M. Savukov, V. M. Acosta, D. Budker, and M. V. Romalis, Physical Review A **77**, 033408 (2008).

[35] K. Jensen, V. M. Acosta, J. M. Higbie, M. P. Ledbetter, S. M. Rochester, and D. Budker, Physical Review A (Atomic, Molecular, and Optical Physics) **79**, 023406 (2009).

[36] V. M. Acosta and et al., New Journal of Physics **12**, 083054 (2010).

[37] M. Jamet, W. Wernsdorfer, C. Thirion, D. Mailly, V. Dupuis, P. Melinon, and A. Perez, Physical Review Letters **86**, 4676 (2001).

[38] J. P. Cleuziou, W. Wernsdorfer, V. Bouchiat, T. Ondarcuhu, and M. Monthioux, Nat Nano **1**, 53 (2006).

[39] D. Rugar, R. Budakian, H. J. Mamin, and B. W. Chui, Nature **430**, 329 (2004).

[40] H. J. Mamin, M. Poggio, C. L. Degen, and D. Rugar, Nat Nano **2**, 301 (2007).

[41] C. L. Degen, Applied Physics Letters **92**, 243111 (2008).

[42] G. Balasubramanian, P. Neumann, D. Twitchen, M. Markham, R. Kolesov, N. Mizuochi, J. Isoya, J. Achard, J. Beck, J. Tissler, V. Jacques, P. R. Hemmer, F. Jelezko, and J. Wrachtrup, Nat Mater **8**, 383 (2009).

[43] B. M. Chernobrod and G. P. Berman, Journal of Applied Physics **97**, 014903 (2005).

[44] V. M. Acosta, E. Bauch, A. Jarmola, L. J. Zipp, M. P. Ledbetter, and D. Budker, Applied Physics Letters **97**, 174104 (2010).

[45] L. T. Hall, J. H. Cole, C. D. Hill, and L. C. L. Hollenberg, Physical Review Letters **103**, 220802 (2009).

[46] L. T. Hall, C. D. Hill, J. H. Cole, B. Stadler, F. Caruso, P. Mulvaney, J. Wrachtrup, and L. C. L. Hollenberg, Proceedings of the National Academy of Sciences **107**, 18777 (2010).

[47] B. J. Maertz, A. P. Wijnheijmer, G. D. Fuchs, M. E. Nowakowski, and D. D. Awschalom, Applied Physics Letters **96**, 092504 (2010).

[48] L. S. Bouchard, E. Bauch, V. M. Acosta, and D. Budker, New Journal of Physics **13**, 025017 (2011).

[49] P. C. Maurer, J. R. Maze, P. L. Stanwix, L. Jiang, A. V. Gorshkov, A. A. Zibrov, B. Harke, J. S. Hodges, A. S. Zibrov, A. Yacoby, D. Twitchen, S. W. Hell, R. L. Walsworth, and M. D. Lukin, Nature Physics **6**, 912 (2010).

[50] B. R. Smith, D. W. Inglis, B. Sandnes, J. R. Rabeau, A. V. Zvyagin, D. Gruber, C. J. Noble, R. Vogel, E. Osawa, and T. Plakhotnik, Small **5**, 1649 (2009).

[51] C. Bradac, T. Gaebel, N. Naidoo, J. R. Rabeau, and A. S. Barnard, Nano Letters **9**, 3555 (2009).

[52] T. M. Babinec, B. J. M. Hausmann, M. Khan, Y. Zhang, J. R. Maze, P. R. Hemmer, and M. Loncar, Nat Nano **5**, 195 (2010).

[53] R. S. Schoenfeld and W. Harneit, Physical Review Letters **106**, 030802 (2011).

[54] S. Steinert, F. Dolde, P. Neumann, A. Aird, B. Naydenov, G. Balasubramanian, F. Jelezko, and J. Wrachtrup, Review of Scientific Instruments **81**, 043705 (2010).

[55] S. Felton, A. M. Edmonds, M. E. Newton, P. M. Martineau, D. Fisher, D. J. Twitchen, and J. M. Baker, Physical Review B (Condensed Matter and Materials Physics) **79**, 075203 (2009).

[56] P. L. Stanwix, L. M. Pham, J. R. Maze, D. Le Sage, T. K. Yeung, P. Cappellaro, P. R. Hemmer, A. Yacoby, M. D. Lukin, and R. L. Walsworth, Physical Review B **82**, 201201 (2010).

[57] E. E. Mikhailov, I. Novikova, M. D. Havey, and F. A. Narducci, Opt. Lett. **34**, 3529 (2009).

[58] V. Shah, S. Knappe, P. D. D. Schwindt, and J. Kitching, Nat Photon **1**, 649 (2007).

[59] C. L. Degen, M. Poggio, H. J. Mamin, C. T. Rettner, and D. Rugar, Proceedings of the National Academy of Sciences **106**, 1313 (2009).

[60] E. Fermi and F. Rasetti, Zeitschrift fur Physik A Hadrons and Nuclei **33**, 246 (1925).

[61] F. Bitter, Physical Review **76**, 833 (1949).

[62] J. Brossel and F. Bitter, Physical Review **86**, 308 (1952).

[63] S. Geschwind, R. J. Collins, and A. L. Schawlow, Physical Review Letters **3**, 545 (1959).

[64] I. Wieder, Physical Review Letters **3**, 468 (1959).

[65] Y. K. Zavoisky, J. Phys. USSR **9**, 245 (1945).

[66] J. H. E. Griffiths, J. Owen, and I. M. Ward, Nature **173**, 439 (1954).

[67] J. H. Griffiths, J. Owen, and I. M. Ward, in *Defects in Crystalline Solids* (The Physical Society, London, ADDRESS, 1955), pp. 81–87.

[68] W. V. Smith, P. P. Sorokin, I. L. Gelles, and G. J. Lasher, Physical Review **115**, 1546 (1959).

[69] W. Happer, Reviews of Modern Physics **44**, 169 (1972).

[70] J. Loubser and J. A. van Wyk, Reports on Progress in Physics **41**, 1201 (1978).

[71] N. R. S. Reddy, N. B. Manson, and E. R. Krausz, Journal of Luminescence **38**, 46 (1987).

[72] E. van Oort, N. B. Manson, and M. Glasbeek, Journal of Physics C-Solid State Physics **21**, 4385 (1988).

[73] G. Davies and M. F. Hamer, Proceedings of the Royal Society of London Series a-Mathematical Physical and Engineering Sciences **348**, 285 (1976).

[74] W. Neuhauser, M. Hohenstatt, P. E. Toschek, and H. Dehmelt, Physical Review A **22**, 1137 (1980).

[75] J. Kohler, J. A. J. M. Disselhorst, M. C. J. M. Donckers, E. J. J. Groenen, J. Schmidt, and W. E. Moerner, Nature **363**, 242 (1993).

[76] J. Wrachtrup, C. von Borczyskowski, J. Bernard, M. Orritt, and R. Brown, Nature **363**, 244 (1993).

[77] A. Gruber, A. Drabenstedt, C. Tietz, L. Fleury, J. Wrachtrup, and C. von Borczyskowski, Science **276**, 2012 (1997).

[78] S.-J. Yu, M.-W. Kang, H.-C. Chang, K.-M. Chen, and Y.-C. Yu, Journal of the American Chemical Society **127**, 17604 (2005).

[79] A. M. Schrand, H. Huang, C. Carlson, J. J. Schlager, E. ÃĚÅŠsawa, S. M. Hussain, and L. Dai, The Journal of Physical Chemistry B **111**, 2 (2007).

[80] Y.-R. Chang, H.-Y. Lee, K. Chen, C.-C. Chang, D.-S. Tsai, C.-C. Fu, T.-S. Lim, Y.-K. Tzeng, C.-Y. Fang, C.-C. Han, H.-C. Chang, and W. Fann, Nat Nano **3**, 284 (2008).

[81] F. Neugart, A. Zappe, F. Jelezko, C. Tietz, J. P. Boudou, A. Krueger, and J. Wrachtrup, Nano Letters **7**, 3588 (2007).

[82] O. Faklaris, D. Garrot, V. Joshi, F. Druon, J.-P. Boudou, T. Sauvage, P. Georges, P. A. Curmi, and F. Treussart, Small **4**, 2236 (2008).

[83] J. Tisler, G. Balasubramanian, B. Naydenov, R. Kolesov, B. Grotz, R. Reuter, J.-P. Boudou, P. A. Curmi, M. Sennour, A. Thorel, M. Borsch, K. Aulenbacher, R. Erdmann, P. R. Hemmer, F. Jelezko, and J. Wrachtrup, ACS Nano **3**, 1959 (2009).

[84] C. Bradac, T. Gaebel, N. Naidoo, M. J. Sellars, J. Twamley, L. J. Brown, A. S. Barnard, T. Plakhotnik, A. V. Zvyagin, and J. R. Rabeau, Nat Nano **5**, 345 (2010).

[85] F. Jelezko, T. Gaebel, I. Popa, A. Gruber, and J. Wrachtrup, Physical Review Letters **92**, 076401 (2004).

[86] L. Childress, M. V. G. Dutt, J. M. Taylor, A. S. Zibrov, F. Jelezko, J. Wrachtrup, P. R. Hemmer, and M. D. Lukin, Science **314**, 281 (2006).

[87] M. V. G. Dutt, L. Childress, L. Jiang, E. Togan, J. Maze, F. Jelezko, A. S. Zibrov, P. R. Hemmer, and M. D. Lukin, Science **316**, 1312 (2007).

[88] P. Neumann, N. Mizuochi, F. Rempp, P. Hemmer, H. Watanabe, S. Yamasaki, V. Jacques, T. Gaebel, F. Jelezko, and J. Wrachtrup, Science **320**, 1326 (2008).

[89] P. Neumann, R. Kolesov, B. Naydenov, J. Beck, F. Rempp, M. Steiner, V. Jacques, G. Balasubramanian, M. L. Markham, D. J. Twitchen, S. Pezzagna, J. Meijer, J. Twamley, F. Jelezko, and J. Wrachtrup, Nat Phys **6**, 249 (2010).

[90] G. D. Fuchs, V. V. Dobrovitski, D. M. Toyli, F. J. Heremans, and D. D. Awschalom, Science **326**, 1520 (2009).

[91] B. B. Buckley, G. D. Fuchs, L. C. Bassett, and D. D. Awschalom, Science 1196436 (2010).

[92] E. Togan, Y. Chu, A. S. Trifonov, L. Jiang, J. Maze, L. Childress, M. V. G. Dutt, A. S. Sorensen, P. R. Hemmer, A. S. Zibrov, and M. D. Lukin, Nature **466**, 730 (2010).

[93] P. Neumann, J. Beck, M. Steiner, F. Rempp, H. Fedder, P. R. Hemmer, J. Wrachtrup, and F. Jelezko, Science **329**, 542 (2010).

[94] G. de Lange, Z. H. Wang, D. Riste, V. V. Dobrovitski, and R. Hanson, Science **330**, 60 (2010).

[95] P. Hemmer and J. Wrachtrup, Science **324**, 473 (2009).

[96] S. Felton, A. M. Edmonds, M. E. Newton, P. M. Martineau, D. Fisher, and D. J. Twitchen, Physical Review B **77**, (2008).

[97] A. Lenef and S. C. Rand, Physical Review B **53**, 13441 (1996).

[98] J. Maze, A. Gali, E. Togan, Y. Chu, A. S. Trifonov, E. Kaxiras, and M. D. Lukin, New Journal of Physics **13**, 025025 (2011).

[99] J. P. Goss, R. Jones, S. J. Breuer, P. R. Briddon, and S. Oberg, Physical Review Letters **77**, 3041 (1996).

[100] M. Luszczek, R. Laskowski, and P. Horodecki, Physica B-Condensed Matter **348**, 292 (2004).

[101] P. Delaney, J. C. Greer, and J. A. Larsson, Nano Letters **10**, 610 (2010).

[102] Y. Ma, M. Rohlfing, and A. Gali, Physical Review B **81**, 041204 (2010).

[103] E. van Oort, B. Vanderkamp, R. Sitters, and M. Glasbeek, Journal of Luminescence **48-9**, 803 (1991).

[104] N. B. Manson, J. P. Harrison, and M. J. Sellars, Physical Review B **74**, 104303 (2006).

[105] C. Santori, D. Fattal, S. M. Spillane, M. Fiorentino, R. G. Beausoleil, A. D. Greentree, P. Olivero, M. Draganski, J. R. Rabeau, P. Reichart, B. C. Gibson, S. Rubanov, D. N. Jamieson, and S. Prawer, Optics Express **14**, 7986 (2006).

[106] A. Batalov, V. Jacques, F. Kaiser, P. Siyushev, P. Neumann, L. J. Rogers, R. L. McMurtrie, N. B. Manson, F. Jelezko, and J. Wrachtrup, Physical Review Letters **102**, 195506 (2009).

[107] L. J. Rogers, R. L. McMurtrie, S. Armstrong, M. J. Sellars, and N. B. Manson, New Journal of Physics **11**, 063007 (2009).

[108] K.-M. C. Fu, C. Santori, P. E. Barclay, L. J. Rogers, N. B. Manson, and R. G. Beausoleil, Physical Review Letters **103**, 256404 (2009).

[109] P. R. Hemmer, A. V. Turukhin, M. S. Shahriar, and J. A. Musser, Opt. Lett. **26**, 361 (2001).

[110] C. Santori, P. Tamarat, P. Neumann, J. Wrachtrup, D. Fattal, R. G. Beausoleil, J. Rabeau, P. Olivero, A. D. Greentree, S. Prawer, F. Jelezko, and P. Hemmer, Physical Review Letters **97**, (2006).

[111] A. Gali, T. Simon, and J. E. Lowther, New Journal of Physics **13**, 025016 (2011).

[112] G. Davies, Journal of Physics C-Solid State Physics **7**, 3797 (1974).

[113] P. Tamarat, N. B. Manson, J. P. Harrison, R. L. McMurtrie, A. Nizovtsev, C. Santori, R. G. Beausoleil, P. Neumann, T. Gaebel, F. Jelezko, P. Hemmer, and J. Wrachtrup, New Journal of Physics **10**, (2008).

[114] S. Y. Kilin, A. P. Nizovtsev, T. M. Maevskaya, A. Drabenstedt, and J. Wrachtrup, Journal of Luminescence **86**, 201 (2000).

[115] J. Harrison, M. J. Sellars, and N. B. Manson, Diamond and Related Materials **15**, 586 (2006).

[116] G. D. Fuchs, V. V. Dobrovitski, D. M. Toyli, F. J. Heremans, C. D. Weis, T. Schenkel, and D. D. Awschalom, Nat Phys **6**, 668 (2010).

[117] L. Robledo, H. Bernien, T. van der Sar, and R. Hanson, New Journal of Physics **13**, 025013 (2011).

[118] V. M. Acosta, E. Bauch, M. P. Ledbetter, A. Waxman, L. S. Bouchard, and D. Budker, Physical Review Letters **104**, 070801 (2010).

[119] B. Smeltzer, J. McIntyre, and L. Childress, Physical Review A **80**, 050302 (2009).

[120] M. Steiner, P. Neumann, J. Beck, F. Jelezko, and J. Wrachtrup, Physical Review B **81**, 035205 (2010).

[121] N. D. Lai, D. Zheng, F. Jelezko, F. Treussart, and J.-F. Roch, Applied Physics Letters **95**, 133101 (2009).

[122] X. F. He, N. B. Manson, and P. T. H. Fisk, Physical Review B **47**, 8816 (1993).

[123] E. van Oort and M. Glasbeek, Chemical Physics Letters **168**, 529 (1990).

[124] F. Dolde, H. Fedder, M. W. Doherty, T. Nobauer, F. Rempp, G. Balasubramanian, T. Wolf, F. Reinhard, L. C. L. Hollenberg, F. Jelezko, and J. Wrachtrup, Nature Physics (2011).

[125] S. J. Smullin, I. M. Savukov, G. Vasilakis, R. K. Ghosh, and M. V. Romalis, Physical Review A **80**, 033420 (2009).

[126] J. R. Maze, J. M. Taylor, and M. D. Lukin, Physical Review B **78**, 094303 (2008).

[127] S. Takahashi, R. Hanson, J. van Tol, M. S. Sherwin, and D. D. Awschalom, Physical Review Letters **101**, 047601 (2008).

[128] N. Mizuochi, P. Neumann, F. Rempp, J. Beck, V. Jacques, P. Siyushev, K. Nakamura, D. J. Twitchen, H. Watanabe, S. Yamasaki, F. Jelezko, and J. Wrachtrup, Physical Review B **80**, 041201 (2009).

[129] D. A. Redman, S. Brown, R. H. Sands, and S. C. Rand, Physical Review Letters **67**, 3420 (1991).

[130] J. P. King, P. J. Coles, and J. A. Reimer, Physical Review B **81**, 073201 (2010).

[131] S. C. Lawson, D. Fisher, D. C. Hunt, and M. E. Newton, Journal of Physics-Condensed Matter **10**, 6171 (1998).

[132] I. Aharonovich, C. Santori, B. A. Fairchild, J. Orwa, K. Ganesan, K.-M. C. Fu, R. G. Beausoleil, A. D. Greentree, and S. Prawer, Journal of Applied Physics **106**, 124904 (2009).

[133] B. Naydenov, V. Richter, J. Beck, M. Steiner, P. Neumann, G. Balasubramanian, J. Achard, F. Jelezko, J. Wrachtrup, and R. Kalish, Applied Physics Letters **96**, 163108 (2010).

[134] E. L. Hahn, Physical Review **80**, 580 (1950).

[135] E. Van Oort and M. Glasbeek, Chemical Physics **143**, 131 (1990).

[136] G. De Lange, D. Riste, V. V. Dobrovitski, and R. Hanson, Physical Review Letters **106**, 080802 (2011).

[137] A. Laraoui, J. S. Hodges, and C. A. Meriles, Applied Physics Letters **97**, 143104 (2010).

[138] P. Cappellaro and M. D. Lukin, Physical Review A **80**, 032311 (2009).

[139] C. A. Ryan, J. S. Hodges, and D. G. Cory, Physical Review Letters **105**, 200402 (2010).

[140] B. Naydenov, F. Dolde, L. T. Hall, C. Shin, H. Fedder, L. C. L. Hollenberg, F. Jelezko, J. Wrachtrup, ouml, and rg, Physical Review B **83**, 081201 (2011).

[141] H. J. Mamin, R. Budakian, B. W. Chui, and D. Rugar, Physical Review B **72**, 024413 (2005).

[142] K. Y. Han, S. K. Kim, C. Eggeling, and S. W. Hell, Nano Letters **10**, 3199 (2010).

[143] C. Santori, P. E. Barclay, . K.-M. C. Fu, R. G. Beausoleil, S. Spillane, and M. Fisch, Nanotechnology **21**, 274008 (2010).

[144] A. Faraon, P. E. Barclay, C. Santori, . K.-M. C. Fu, and R. G. Beausoleil, Nature Photonics (2011).

[145] J. P. Hadden, J. P. Harrison, A. C. Stanley-Clarke, L. Marseglia, Y. L. D. Ho, B. R. Patton, J. L. O'Brien, and J. G. Rarity, Applied Physics Letters **97**, 241901 (2010).

[146] P. Siyushev, F. Kaiser, V. Jacques, I. Gerhardt, S. Bischof, H. Fedder, J. Dodson, M. Markham, D. Twitchen, F. Jelezko, and J. Wrachtrup, Applied Physics Letters **97**, 241902 (2010).

[147] L. Marseglia, J. P. Hadden, A. C. Stanley-Clarke, J. P. Harrison, B. Patton, Y.-L. D. Ho, B. Naydenov, F. Jelezko, J. Meijer, P. R. Dolan, J. M. Smith, J. G. Rarity, and J. L. O'brien, Nano-fabricated solid immersion lenses registered to single emitters in diamond, 2010, arXiv:1012.1135v2 [quant-ph].

[148] S. Schietinger, M. Barth, T. Aichele, and O. Benson, Nano Letters **9**, 1694 (2009).

[149] R. Kolesov, B. Grotz, G. Balasubramanian, R. J. Stohr, A. A. L. Nicolet, P. R. Hemmer, F. Jelezko, and J. Wrachtrup, Nature Physics **5**, 470 (2009).

[150] A. Huck, S. Kumar, A. Shakoor, and U. L. Andersen, Physical Review Letters **106**, 096801 (2011).

[151] E. Rittweger, D. Wildanger, and S. W. Hell, European Physics Letters **86**, 14001 (2009).

[152] K. Y. Han, K. I. Willig, E. Rittweger, F. Jelezko, C. Eggeling, and S. W. Hell, Nano Letters **9**, 3323 (2009).

[153] A. Batalov, C. Zierl, T. Gaebel, P. Neumann, I. Y. Chan, G. Balasubramanian, P. R. Hemmer, F. Jelezko, and J. Wrachtrup, Physical Review Letters **100**, 077401 (2008).

[154] G. Waldherr, J. Beck, M. Steiner, P. Neumann, A. Gali, F. Jelezko, and J. Wrachtrup, Physical Review Letters (2011).

[155] H. Kanda and T. Sekine, in *Properties, Growth, and Applications of Diamond*, edited by M. H. Nazare (INSPEC, London, 2000), pp. 247–255.

[156] P. Bachmann, in *Properties and Growth of Diamond*, edited by G. Davies (INSPEC, London, 1994), pp. 354–363.

[157] D. W. Palmer, in *Properties and Growth of Diamond*, edited by G. Davies (INSPEC, London, 1994), pp. 143–158.

[158] F. C. Waldermann, P. Olivero, J. Nunn, K. Surmacz, Z. Y. Wang, D. Jaksch, R. A. Taylor, I. A. Walmsley, M. Draganski, P. Reichart, A. D. Greentree, D. N. Jamieson, and S. Prawer, Diamond and Related Materials **16**, 1887 (2007).

[159] M. E. Newton, B. A. Campbell, D. J. Twitchen, J. M. Baker, and T. R. Anthony, Diamond and Related Materials **11**, 618 (2002).

[160] J. F. Ziegler, J. P. Biersack, and U. Littmark, *The Stopping Range of Ions in Matter* (SRIM, Co., Chester, MD, USA, 2008).

[161] J. C. Bourgoin and B. Massarani, Physical Review B **14**, 3690 (1976).

[162] J. Koike, D. M. Parkin, and T. E. Mitchell, Applied Physics Letters **60**, 1450 (1992).

[163] D. Saada, J. Adler, and R. Kalish, International Journal of Modern Physics C **9**, 61 (1998).

[164] W. H. Press, S. A. Teukolsky, W. T. Vetterling, and B. P. Flannery, *Numerical recipes in C (2nd ed.): the art of scientific computing* (Cambridge University Press, New York, 1992).

[165] A. T. Collins, Journal of Physics C-Solid State Physics **14**, 289 (1981).

[166] L. Allers, A. T. Collins, and J. Hiscock, Diamond and Related Materials **7**, 228 (1998).

[167] Y. Mita, Physical Review B **53**, 11360 (1996).

[168] C. Santori, P. E. Barclay, K. M. C. Fu, and R. G. Beausoleil, Physical Review B **79**, 125313 (2009).

[169] D. C. Hunt, D. J. Twitchen, M. E. Newton, J. M. Baker, T. R. Anthony, W. F. Banholzer, and S. S. Vagarali, Physical Review B **61**, 3863 (2000).

[170] C. Glover, M. E. Newton, P. M. Martineau, S. Quinn, and D. J. Twitchen, Physical Review Letters **92**, 135502 (2004).

[171] C. Glover, M. E. Newton, P. Martineau, D. J. Twitchen, and J. M. Baker, Physical Review Letters **90**, 185507 (2003).

[172] G. Davies and M. Crossfield, Journal of Physics C-Solid State Physics **6**, L104 (1973).

[173] G. Davies, S. C. Lawson, A. T. Collins, A. Mainwood, and S. J. Sharp, Physical Review B **46**, 13157 (1992).

[174] B. Campbell and A. Mainwood, Physica Status Solidi a-Applications and Materials Science **181**, 99 (2000).

[175] We say here “effective” energy splitting because in reality these vibrational levels are so strongly coupled to the continuum of delocalized phonons that there are no clear resonances.

[176] D. J. Twitchen, D. C. Hunt, V. Smart, M. E. Newton, and J. M. Baker, Diamond and Related Materials **8**, 1572 (1999).

[177] A. T. Collins and G. S. Woods, Philosophical Magazine B **46**, 77 (1982).

[178] R. M. Chrenko, H. M. Strong, and R. E. Tuft, Philosophical Magazine **23**, 313 (1971).

[179] G. S. Woods, J. A. Vanwyk, and A. T. Collins, Philosophical Magazine B-Physics of Condensed Matter Statistical Mechanics Electronic Optical and Magnetic Properties **62**, 589 (1990).

[180] G. S. Woods and A. T. Collins, Journal of Physics C-Solid State Physics **15**, L949 (1982).

[181] I. Kiflawi, A. Mainwood, H. Kanda, and D. Fisher, Physical Review B **54**, 16719 (1996).

[182] A. T. Collins, M. Stanley, and G. S. Woods, Journal of Physics D-Applied Physics **20**, 969 (1987).

[183] N. B. Manson and J. P. Harrison, Diamond and Related Materials **14**, 1705 (2005).

[184] T. Gaebel, M. Domhan, C. Wittmann, I. Popa, F. Jelezko, J. Rabeau, A. Greentree, S. Prawer, E. Trajkov, P. R. Hemmer, and J. Wrachtrup, Applied Physics B-Lasers and Optics **82**, 243 (2006).

[185] F. Jelezko and J. Wrachtrup, Physica Status Solidi a-Applications and Materials Science **203**, 3207 (2006).

[186] S. K. Lee, M. Mossle, W. Myers, N. Kelso, A. H. Trabesinger, A. Pines, and J. Clarke, Magnetic Resonance in Medicine **53**, 9 (2005).

[187] I. M. Savukov, S. J. Seltzer, and M. V. Romalis, Journal of Magnetic Resonance **185**, 214 (2007).

[188] J. R. Kirtley, A. C. Mota, M. Sigrist, and T. M. Rice, Journal of Physics-Condensed Matter **10**, L97 (1998).

[189] G. D. Fuchs, V. V. Dobrovitski, R. Hanson, A. Batra, C. D. Weis, T. Schenkel, and D. D. Awschalom, Physical Review Letters **101**, 117601 (2008).

[190] A. P. Nizovtsev, S. Y. Kilin, C. Tietz, F. Jelezko, and J. Wrachtrup, Physica B: Condensed Matter **308-310**, 608 (2001).

[191] A. Gali, E. Janzen, P. Deak, G. Kresse, and E. Kaxiras, Physical Review Letters **103**, 186404 (2009).

[192] A. C. Victor, The Journal of Chemical Physics **36**, 1903 (1962).

[193] For both of the samples studied in this work, we find the transition to occur at 1042.5(3) nm. In Ref. [26], the authors reported the ZPL to be at 1046 nm, but, according to private communication with the authors, this was a misprint.

[194] N. B. Manson and R. L. McMurtrie, Journal of Luminescence **127**, 98 (2007).

[195] A. Drabenstedt, L. Fleury, C. Tietz, F. Jelezko, S. Kilin, A. Nizovtzev, and J. Wrachtrup, Physical Review B **60**, 11503 (1999).

[196] J. Lakowicz, *Principles of Fluorescence Spectroscopy*, 3rd ed. (Springer, New York, 2006).

[197] Because measurements were made in high-defect-density samples, where each NV center experiences a different local environment, we neglect the difference in lifetimes between $m_s = \pm 1$ and $m_s = 0$ sublevels.

[198] W. D. Partlow and H. W. Moos, Physical Review **157**, 251 (1967).

[199] R. J. Epstein, F. M. Mendoza, Y. K. Kato, and D. D. Awschalom, Nat Phys **1**, 94 (2005).

[200] F. M. Hossain, M. W. Doherty, H. F. Wilson, and L. C. L. Hollenberg, Physical Review Letters **101**, 226403 (2008).